

UCLA

UCLA Electronic Theses and Dissertations

Title

Ubiquitous non- and minimally-invasive biosensing technologies for personalized and precision medicine

Permalink

<https://escholarship.org/uc/item/93b946t6>

Author

Lin, Shuyu

Publication Date

2022

Peer reviewed|Thesis/dissertation

UNIVERSITY OF CALIFORNIA

Los Angeles

Ubiquitous non- and minimally-invasive biosensing technologies for personalized and precision
medicine

A thesis submitted in partial satisfaction
of the requirements for the degree Doctor of Philosophy
in Electrical and Computer Engineering

by

Shuyu Lin

2022

© Copyright by

Shuyu Lin

2022

ABSTRACT OF THE DISSERTATION

Ubiquitous non- and minimally-invasive biosensing technologies for personalized and precision
medicine

by

Shuyu Lin

Doctor of Philosophy in Electrical and Computer Engineering

University of California, Los Angeles, 2022

Professor Sam Emaminejad, Chair

Recent advances in miniaturized electronics, microfluidics, and electrochemical sensing platforms have paved the path for the realization of wearable and mobile biosensing systems that can be deployed to longitudinally access the circulating molecular information. Leveraging their non-/minimally-invasive nature and a high sampling rate, these systems provides people with a unprecedented accessibility to their health-related information, opening up new possibilities such as personalized medicine, precision nutrition, and performance enhancement. Towards realizing the envisioned biomonitoring ecosystem, various technical challenges remain unresolved, centering on the sampling and sensing of circulating molecular information. For example, sweat

is widely targeted for non-invasive biomonitoring. However, current sweat sampling approaches are mainly stimulation-based (e.g., heat, exercise, iontophoresis), which is associated with user intervention and/or discomfort. Moreover, human subject studies are lacking to establish the physiological significance of the sweat biomarker levels. From the sensing side, electrochemical sensors are widely leveraged to quantify the analyte concentration levels due to their capability to provide sample-to-answer readouts. To accurately analyze untreated biofluids, novel sensor design and multi-dimension optimization are required to simultaneously achieve the required figure of merits, including sensitivity, selectivity, biofouling resistance, and generalizability.

In my Ph.D. training, I devised sensor- and system-level solutions to address these challenges. As an immediate group of targets, my research mainly focusses on monitoring circulating drug levels as it can be leveraged to personalize dosing, evaluate adherence, and prevent abuse. In summary of my research work, the thesis is structured as follows: chapter 1 introduces the background of non-/minimally-invasive biomonitoring, including the existing bio-interfaces and electrochemical sensing mechanisms; chapter 2 describes the use of a thin hydrogel patch to simultaneously sample and analyze analyte concentrations in natural perspiration; chapter 3 further expands the innovation from chapter 2 and demonstrates a multi-modal human machine interface; chapter 4 describes an organohydrogel-based one-touch sensing interface for lithium therapy monitoring; chapter 5 focuses on resolving the challenges associated with voltammetry-based sensor—a simple recognition element-free sensing approach to target electroactive analyte—and demonstrates a wearable drug sensing smartwatch; chapter 6 presents my efforts to achieve a generalizable solution, where I demonstrated a microneedle-based aptamer sensor to target interstitial fluid analytes.

The dissertation of Shuyu Lin is approved.

Dino Di Carlo

Aydogan Ozcan

Carlos Milla

Sam Emaminejad, Committee Chair

University of California, Los Angeles

2022

Table of Contents

List of Figures	xi
Acknowledgements	xv
Vita.....	xvii
Chapter 1 Introduction.....	1
1.1 Non-/minimally-invasive biomonitoring.....	1
1.2 Electrochemical sensors	2
1.2.1. Electroenzymatic sensors	4
1.2.2. Ion-selective sensing interfaces.....	7
1.2.3. Bioaffinity-based sensors	8
1.2.4. Synthetic receptor-based chemical sensors	9
1.2.5. Recognition element-free sensors	10
1.3 Access sweat and microfluidic interfaces.....	10
1.4 Reference	13
Chapter 2. Thin hydrogel-coated sensors for natural perspiration sampling and in-situ electrochemical analysis	17
2.1 Introduction.....	17
2.2. Experimental Section	21
2.2.1. Materials and Reagents	21
2.2.2. TH Fabrication	22
2.2.3. TH-sensor Construction	22
2.2.4. Characterization of TH-based natural perspiration sampling	24

2.2.5. Lactate Quantification with Lab Instrument.....	24
2.2.6. Caffeine quantification with liquid chromatography – tandem mass spectrometry	25
2.2.7. Microfluidic artificial fingertip fabrication and characterization.....	26
2.2.8. Simulation of analyte flux.....	27
2.2.9. Ex-situ TH-sensor characterization	27
2.2.10. Institutional Review Board (IRB) Approval for Human Subject Testing:.....	28
2.3. Naturally perspired analyte sampling	28
2.4. Formulation of an epidermal TH-sensing signal interpretation framework	31
2.5. Development of a microfluidic artificial fingertip for characterization and empirical validation of the TH-sensors and signal interpretation framework.....	33
2.6. Development and ex-situ characterization of TH-sensors for epidermal biosensing	34
2.7 Conclusions.....	37
2.8. Reference	38
Chapter 3. A touch-based multi-modal and cryptographic bio-human-machine interface	42
3.1. Introduction.....	42
3.2. Experimental Section	45
3.2.1. TH-sensor fabrication and in-situ characterizations	45
3.2.2. PPG signal acquisition and processing	46
3.2.3. Fingerprint acquisition and user identification	47
3.2.4. CBS Construction	48
3.2.5. CB-HMI construction	49
3.2.6. Construction of CB-HMI-enabled systems	50

3.2.7. Human subject testing using the CB-HMI-enabled systems.....	50
3.2.8. Institutional Review Board Approval for Human Subject Testing	51
3.3. In-situ characterization of the thin hydrogel-coated electrochemical.....	51
3.4. Develop and integration of the multimodal data acquisition and processing modules	53
3.5. Development and application of a CB-HMI-enabled in-vehicle safety system	56
3.6. Development and application of a CB-HMI-enabled medication dispensing robotic system	57
3.7. Discussion.....	59
3.8. Reference	61
Chapter 4. Touch-based non-invasive lithium monitoring using an organohydrogel-based sensing interface	65
4.1. Introduction.....	65
4.2. Experimental Section	67
4.2.1. Materials and Reagents.	67
4.2.2. Fabrication and characterization of TOH	67
4.2.3. Fabrication and characterization of lithium ISE.....	68
4.2.4. Ex-situ TOH-ISE characterizations	69
4.2.5. In-situ TOH-ISE characterization	70
4.2.6. Institutional Review Board Approval for Human Subject Testing	70
4.3. Development and characterization of individual components	70
4.4. TOH-ISE characterization	72
4.5. In-situ TOH-ISE characterization	74
4.6. Reference	75

Chapter 5. Voltammetric sensing interfaces for non-invasive wearable electroactive pharmaceutical monitoring	78
5.1. Introduction.....	78
5.2. Experimental Section	81
5.2.1. Materials and Reagents.	81
5.2.2. Electrode preparation and electrochemical measurements.	82
5.2.3. Sweat and saliva collection and ex-situ measurement.	83
5.2.4. APAP quantification with LC-MS/MS.....	84
5.2.5. Construction of microfluidic interface.	84
5.2.6. Wireless electronic module and smartwatch design.	85
5.2.7. On-body tracking of APAP metabolic profile.	86
5.2.8. Analytical framework for peak height information extraction.....	86
5.2.9. Pharmacokinetic analysis.	87
5.2.10. Institutional Review Board (IRB) approval for human subject testing.....	87
5.3. Determination of suitable sensing electrode for electroactive drug analysis.	87
5.4. Interference study to determine operational window for electroactive drug analysis	91
5.5. Wireless voltammetric sensing system for wearable electroactive drug analysis	93
5.6. Surface engineering to render undistorted and fouling-resistant voltammetric sensing.....	95
5.7. Voltammetric sensing solution for non-invasive pharmacokinetic monitoring	101
5.8. Conclusion and discussion	103
5.9. Reference	106

Chapter 6. Wearable microneedle-based electrochemical aptamer biosensing for precision dosing of drugs with narrow therapeutic windows.....	112
6.1. Introduction.....	112
6.2. Experimental Section	115
6.2.1. Materials and Reagents	115
6.2.2. μ NEAB-patch fabrication	116
6.2.3. Characterization of microneedle electrode surface morphologies and chemical compositions	117
6.2.4. DNA aptamer sequences.	117
6.2.5. EAB fabrication	118
6.2.6. Ex-vivo μ NEAB characterization.	118
6.2.7. Skin penetration efficiency test	119
6.2.8. In-vitro biocompatibility test.....	120
6.2.9. In-vivo μ NEAB-patch characterization on a rat model	120
6.2.10. Data analysis for in-vivo experiments	121
6.2.11. Pharmacokinetic analysis	122
6.2.12. Tobramycin quantification with LC-MS/MS	122
6.3. Development of μ NEABs	124
6.4. Ex-vivo μ NEAB-patch characterization.....	126
6.5. In-vivo μ NEAB-patch characterization in a rat model	128
6.6. Discussion.....	130
6.7. Reference	132

Figures 136

List of Figures

Figure 1.1. Schematic diagram of electroenzymatic sensor	136
Figure 1.2. Schematic diagram of an electrochemical aptamer-based sensor.	136
Figure 1.3. Schematic diagram of (a) fabrication and (b) application of molecularly imprinted polymers.....	136
Figure 1.4. Schematic for iontophoresis-based sweat induction.....	137
Figure 1.5. Schematic of PDMS-based microfluidic device fabrication.	137
Figure 1.6. Schematic of tape-based microfluidic device fabrication.	137
Figure 2.1. TH-based sampling and sensing interface: design rule and applications.	138
Figure 2.2. Characterization of naturally perspired analyte sampling with TH.....	139
Figure 2.4. Development and validation of a TH-sensing signal interpretation framework.	141
Figure 2.5. Structure of the microfluidic artificial fingertip.	142
Figure 2.6. Ex-vivo characterization of TH-sensors using an artificial fingertip setup.....	143
Figure 2.7. Ex-situ TH-sensor characterization under various flow rates.	143
Figure 3.1. Enabling bio-perception and interpretation via CB-HMI.....	145
Figure 3.2. Development of the multimodal data acquisition and processing modules and validation via human subject studies	146
Figure 3.3. Temporal profiles of biochemical indices (second subject).	147
Figure 3.4. Direct and indirect measurement of the natural perspiration rate profile.....	148
Figure 3.5. CBS encryption and decryption procedure.....	149

Figure 3.6. Biometric-encryption/decryption of a hypothetical input	150
Figure 3.7. Photo of the data acquisition PCB module.....	151
Figure 3.8. System-level block diagram of a CB-HMI-enabled system.....	151
Figure 3.9. A CB-HMI-enabled in-vehicle safety system.	152
Figure 3.10 A CB-HMI-enabled medication dispensing robotic system.....	154
Figure 3.11. The raw and processed bio-inputs in the medication dispensing study.....	155
Figure 4.1. Touch-based lithium monitoring: design rationale and application.....	157
Figure 4.2. Characterization of individual components of the sensing interface.....	158
Figure 4.3. Comparison of two ISM cocktails.....	159
Figure 4.4. Li ⁺ ISE characterization in DI water matrix	159
Figure 4.5. Ex-situ TOH-ISE characterization..	160
Figure 4.6. Variation of sensor readout in an emulated touch-based entry	160
Figure 4.7. Interference of pressing force.....	160
Figure 4.8. In-situ TOH-ISE validation	160
Figure 5.1. A fully-integrated wearable voltammetric drug monitoring solution: design rationale and application.....	163
Figure 5.2. Voltammetric sensing electrode characterization.....	164
Figure 5.3. Comparison of the response of SPCE, GCE, and BDDE towards (a) 2 μ M DP, (b) 10 μ M APAP, and (c) 10 μ M CAFF.	165
Figure 5.4. Systematic voltammetric interference study.....	166

Figure 5.5. Differential pulse voltammograms of electroactive interferents.	167
Figure 5.6. Interference study of non-electroactive species.	168
Figure 5.7. Voltammetric sensing system.....	169
Figure 5.8. Raw DP-spiked sweat measurements.	170
Figure 5.9. Engineering a voltammetric sensing interface for APAP detection within a created undistorted potential window with a high biofouling resistance.	171
Figure 5.10. Interference of other electroactive species.	172
Figure 5.11. Nafion/H-BDDE-enabled ex-situ APAP quantification in non-invasively retrieved biofluid samples	172
Figure 5.12. Sensor-measured APAP concentration in (a) saliva and (b) sweat samples of the second subject.	173
Figure 5.13. Nafion/H-BDDE-enabled wearable solution for on-body pharmacokinetic monitoring.	175
Figure 5.14. Sequential optical images of the in-situ sweat sampling/routing by the designed microfluidic interface.....	175
Figure 6.1. μ NEAB-patch for wearable TDM.....	176
Figure 6.2. Development and characterization of μ NEABs.	177
Figure 6.3. Illustration of the surface area enhancement effect using an AuNP coating.....	179
Figure 6.4. μ NEABs targeting doxorubicin and thrombin	179
Figure 6.5. Ex-vivo μ NEAB-patch characterization.	180
Figure 6.6. μ NEAB drift in a protein-spiked buffer solution.	181

Figure 6.7. In-vivo μ NEAB-patch characterization in a rat model.....	182
Figure 6.8. Optical image of the rat skin right after μ NEAB-patch removal.	182
Figure 6.9. In-vivo biomonitoring using μ NEAB-patches	183
Figure 6.10. Raw PK monitoring results of rat B	183

Acknowledgements

Pursuing a Ph.D. is not an easy decision and performing Ph.D. study in a different department/discipline is even harder. I can still remember my thought processes more than five years ago when I was applying for graduate school. At that time, I was really fascinated about translating knowledge and technologies into practical use and making a difference in the society. That was my main motivation of pursuing my Ph.D. in a different department and in such a multidisciplinary research group. After five years of endeavors, though there are many ups-and-downs as well as changes of mindsets, I am still proud of my decision, and I can tell that I have learnt much more than what I imagined. At the same time, I am also clear that I cannot make these achievements without all the supportive and knowledgeable people around me.

First, I would like to thank my parents and family for always being on my side and motivating me to be a better person. In the COVID pandemic, international traveling becomes a luxury. Despite that, our communication is still effective, and our connection is still tight. Whenever encountering challenging situations and experiencing low mood, they are always there to listen and to provide constructive suggestions. Particularly, as a scientist herself, my mother often provides high-level feedbacks regarding my research progress throughout my Ph.D., which motivates me to set a higher standard for myself. Moreover, I am so grateful that they took good care of the family throughout the years, especially my grandparents, which keeps my mind at ease here in U.S. It is unfortunate that the pandemic prevents us from reunion, and I wish that I can go back soon and share my happiness and achievement these years.

Next, I would like to thank my advisor, Professor Sam Emaminejad for his mentorship in the past five years. Professor Emaminejad is a very innovative and proactive researcher in the field. He always encourages me to think out of the box and view things from different angles. After

working closely with him for years, I realized that research and innovation is not only about the science itself, but also about how you think, formulate, and communicate. What I learnt from him is much more than what I imagined before joining the group. His mentorship significantly improves my problem solving and communication skills and changes my way to look at the world.

Furthermore, I would like to thank all my collaborators, committee members, and colleagues: Dr. Carlos Milla, Prof. Dino Di Carlo, Prof. Aydogan Ozcan, Prof. Zhen Gu, Prof. Hilary Collier, Dr. Bo Wang, Dr. Yichao Zhao, Dr. Haisong Lin, Xuanbing Cheng, Hanna Hojaiji, Wenzhuo Yu, Jialun Zhu, Jiawei Tan, Kiarash A. Sabet, Zhaoqing Wang, Christopher Yeung, Ryan Shih, and so many. I learned a lot from each of them and enjoyed working with them during my Ph.D. journey. I am looking forward to working with them again in the future to push the field moving forward.

Finally, I would like to thank my girlfriend, Ailin He for her companion. Her bravery and life wisdom really means a lot to me. I am grateful that she can come to U.S. again after working in China for years to pursue a challenging yet rewarding new life. Lastly, I would also like to thank my long-term friends for their supports and advice along my Ph.D. journey: Zewei Chen (Purdue), Yue Shen (UCLA), Yuanxing Zhang (Mines), and so many.

Vita

2013 – 2017

B.S., Materials Science and Engineering

Tsinghua University

Beijing, China

2017 – 2019

M.S., Electrical and Computer Engineering

Advisor: Professor Sam Emaminejad

University of California, Los Angeles

Los Angeles, CA

Selected publications:

1. **S. Lin**, J. Zhu, W. Yu, B. Wang, K.A. Sabet, Y. Zhao, X. Cheng, H. Hojaiji, H. Lin, J. Tan, C. Milla, R. W. Davis, and S. Emaminejad, "A touch-based multi-modal and cryptographic bio-human-machine interface", *Proceedings of the National Academy of Sciences*, 119 (15), e22019371192022, 2022.
2. **S. Lin**, W. Yu, B. Wang, Y. Zhao, K. En, J. Zhu, X. Cheng, C. Zhou, H. Lin, Z. Wang, H. Hojaiji, C. Yeung, C. Milla, R. W. Davis, and S. Emaminejad, "Noninvasive wearable electroactive pharmaceutical monitoring for personalized therapeutics", *Proceedings of the National Academy of Sciences*, 117 (32), 19017-19025, 2020.
2. **S. Lin**, B. Wang, W. Yu, K. Castillo, C. Hoffman, X. Cheng, Y. Zhao, Y. Gao, Z. Wang, H. Lin, H. Hojaiji, J. Tan, and S. Emaminejad. "Design Framework and Sensing System for Non-invasive Wearable Electroactive Drug Monitoring," *ACS Sensors*, 5(1), 265-273, 2020.
3. **S. Lin**, B. Wang, Y. Zhao, R. Shih, X. Cheng, W. Yu, H. Hojaiji, H. Lin, C. Hoffman, D. Ly, J. Tan, Y. Chen, D. Di Carlo, C. Milla, and S. Emaminejad. "Natural Perspiration Sampling

and In-Situ Electrochemical Analysis with Hydrogel Micropatches for User-Identifiable and Wireless Chemo/bio-sensing," *ACS Sensors*, 5(1), 265-273, 2020.

4. **S. Lin**, X. Cheng, B. Wang, W. Yu, D. Ly, and S Emaminejad, "A Fouling-Resistant Voltammetric Sensing System for Wearable Electroactive Biomarker Monitoring", *Journal of Microelectromechanical Systems*, 29(5), 1059-1063, 2020.

Patents:

1. "METHODS FOR MITIGATING BIOFOULING EFFECTS OF BIOFLUID INTERFERENTS TO DETECT IN VIVO BIOCHEMICAL AND WEARABLE DEVICE THEREFOR," S. Emaminejad, **S. Lin**, date: 07/06/2021, Application No: 17/368,694

2. "DEVICE AND METHOD OF DETECTING AND CALIBRATING A VOLTAMMETRIC RESPONSE TO IN VIVO BIOCHEMICALS," S. Emaminejad, **S. Lin**, B. Wang, date: 04/29/2021, International Publication No: WO 2021/0815-2 A1

3. "ELECTROSTIMULATION-FREE AND BIOMETRICALLY ENCRYPTABLE NONINVASIVE BIOCHEMICAL SENSING DEVICE AND METHOD," S. Emaminejad, **S. Lin**, B. Wang, date: 04/29/2021, International Publication No: WO 2021/081118 A1

Awards:

1. UCLA Dissertation Year Fellowship, 2021
2. UCLA ECE Preliminary Examination Fellowship, 2019
3. Best Poster Presentation, UCLA ECE Annual Research Review, 2018
4. Excellent Bachelor of Tsinghua University, China, 2017

Chapter 1 Introduction

1.1 Non-/minimally-invasive biomonitoring

Recent advances in wearable and mobile sensors have provided unprecedented opportunities for (semi)continuous monitoring of personal health. The proliferation of these sensors and the accumulation of the collected physiologically-relevant information can be adapted to applications ranging from personal fitness and nutrition monitoring to clinical diagnostics [1]. To date, most wearable medical devices focus on detection and tracking of physical signals (e.g., physical activity, vital signs, etc.) using physical sensors. Some notable examples include heart rate, electrodermal activity, electrocardiography, and muscle oxygen saturation [2-4]. However, physical signals are not the only source of physiologically relevant data. Chemical signals accessible through various biofluids (e.g., endogenous biomarker molecules and xenobiotics) can also provide valuable insights into personal health and disease status, which can enable various applications including general health monitoring (e.g., fitness and nutrient monitoring), drug tracking (e.g., drug compliance, pharmacokinetics, and pharmacodynamics), and disease diagnosis. Compared to traditional lab-based chemical tests, wearable chemical sensing modalities are more accessible and can enable real-time data acquisition and analysis. The significant increase in temporal data acquisition frequency (e.g., from one sample per year in the annual body check to one sample per hour for a (semi)continuous monitoring wearable sensor) presents a high potential to transform the current practices in health care and to catalyze the transition from traditional reactive medicine to preventive and personalized medicine.

While blood is the gold-standard biofluid for accessing the body's chemical information, the invasive nature of its sampling process (and its subsequent risk of infection and tissue damage) renders it unsuitable for wearable applications designed for the general population. To access analytes in a non-invasive or minimally invasive manner, alternative biofluids may be targeted instead, including interstitial fluid (ISF), saliva, sweat, and tears [5]. Each of these candidates has been shown to have distinct advantages and limitations:

- ISF: Analyte concentration in ISF is highly correlated with blood (nearly 1:1 for most analytes), which has been demonstrated in the case of glucose monitoring [6]. However, sampling ISF can be challenging as it does not have a naturally-existing secretion pathway.
- Sweat: Non-invasively and continuously accessible on the skin surface with minimal user intervention. The physiological significance of sweat readings need to be established via systematic investigation.
- Saliva: Wearable saliva monitoring was also demonstrated [7]. While saliva is easy to access, the analyte concentration in saliva is prone to the influence of meal intake.
- Tears: Sampling tears can be extremely challenging and may cause irritation [8].

1.2 Electrochemical sensors

Compared with wearable physical sensors, which aim to track the user's vital signs and mobility, wearable chemical sensors are designed for monitoring of chemical markers (analytes) continuously and obtaining comprehensive information about the individuals' health and wellness at the molecular level [1, 9]. To target a biomarker precisely, specific characteristics of ideal chemical sensors include:

- Low limit of detection and high sensitivity. While the precise partitioning mechanism of biomarkers into biofluids is unknown, these molecules are often significantly diluted compared to the concentrations in blood. It naturally follows that an ideal sensor will be sensitive to these low levels.

- High selectivity to the target biomarker(s) with minimal interference of biofluid matrix. Due to the myriad of compounds present in any biofluid, it is imperative that a sensor selectively target the biomarker(s) of interest without influencing by other molecules and biofluid conditions (e.g., pH, ionic strength).

- Long-term operational and storage stability. As wearable sensors are envisioned to operate for continuous monitoring applications, they must be able to function predictably over relatively long periods of time with minimal degradation. This property also extends to storage stability, which has obvious importance for commercial products.

- The convenience of application and maintenance during use. While biomarker sensor research has primarily focused on developing robust sensing platforms, convenient sensor applications, user comfort, and ease of maintenance/removal are necessary requirements for commercial products. For some, the ergonomic performance may even be of equal importance to the sensor's scientific potency.

- Capacity for integration within data-collection infrastructure. Most relevant for Internet-of-Thing (IoT) networks, sensors must be easily integrated with electronic devices that can convert sensed signals into useful data. These data could then be analyzed in real time or secured in cloud storage for larger data sets.

Various signal transduction mechanisms can be leveraged to facilitate chemical sensing, including electrochemical [10], optical [11], and mechanical [12]. Among those mechanisms,

electrochemical sensing methodology (chemical-to-electrical signal transduction) appears to be promising for wearable applications because of its ease of integration with electronics for signal process/transduction and eliminating user intervention. Therefore, the majority of the reported wearable sensors employed electrochemical methods aiming for a sample-to-answer manner.

Targeting for the selective and sensitive measurement of desired biomarkers, recognition elements (e.g., selective membrane, enzyme, antibody, or nucleic acid) are usually immobilized onto the surface of a transducer (e.g., metal electrodes or transistors), which can convert analyte-receptor interactions into a measurable signal. To this end, the electrochemical analysis approaches, such as amperometry, voltammetry, open circuit potential (OCP), can be tailored towards the detection of specific analytes in various concentration ranges and biofluids. In this chapter, we will discuss electroenzymatic, ion-selective, bioaffinity-based, synthetic receptor-based sensors, and recognition element-free sensors in detail. For each type, we will first discuss the nature of recognition followed by complete sensor construction and physical examples existing in a wearable format.

1.2.1. Electroenzymatic sensors

Electroenzymatic sensors have been widely employed in wearable sensing platforms due to their relatively simple design and the availability of commercialized enzyme products. Driven by the need for the management of diabetes, personal blood glucose monitors such as glucose strips and continuous glucose monitoring systems (CGMS) are arguably the most successful commercialized electroenzymatic sensors. In these devices, enzymes serve as highly specific biorecognition elements (due to their active sites' complex and naturally selected 3D structures) to target molecules even in complex biofluids.

Glucose and lactate are two popular sweat analytes in many reported wearable sensing platforms due to their great clinical significance and relatively high concentration levels in sweat (e.g., μM – mM). Recently, He et al. reported a wearable sweat analysis patch based on a silk fabric–derived carbon textile for simultaneous detection of multiple biomarkers, including glucose and lactate, which were monitored by electroenzymatic sensors constructed via immobilization of glucose and lactate oxidases by chitosan, respectively (Detection range: glucose, 50 – 150 μM ; lactate, 5 –15 mM). Amperometric methods were employed for the detection with an applied potential of -0.2 V for lactate and 0.65 V for glucose (versus Ag/AgCl). The responses of glucose sensors did not show significant change after different bending cycles, and they were stable over four weeks. The accuracy of the glucose sensor was validated by comparing the readout from a sweat analysis patch with that of liquid chromatography–mass spectrometry data (HPLC-MS) [13]. Additionally, Emaminejad et al. used a glucose enzymatic sensor, constructed on a flexible polyethylene terephthalate (PET) substrate to validate the physiological utility of sweat glucose by tracking the concentration elevation after glucose consumption. The sensing interface was fabricated on a gold electrode surface with Prussian Blue (PB) as a mediating layer and glucose oxidase as the biorecognition element [14] (Fig. 1.1A). The sensors were further coupled with a miniaturized iontophoresis interface for sweat extraction and in situ analysis. In addition to glucose and lactate, Heikenfeld et al. demonstrated a wearable sweat alcohol sensing platform, utilizing alcohol oxidase as the biorecognition element and amperometry as the electrochemical method, which can stimulate and collect sweat and continuously measure sweat ethanol concentrations. The system determined that sweat alcohol is correlated with blood ethanol, which provides further impetus for studies in wearables and sweat analysis [15].

As we can see, the aforementioned enzymatic sensors all utilized amperometry as the electroanalysis method and enzymes (e.g., oxidases) as biorecognition elements. The amperometric sensors rely on measuring the change in current (proportional to the analyte concentration change) with a constant potential applied between the working and reference electrodes. The current change is caused by the electro-oxidation/-reduction of hydrogen peroxide (H_2O_2), which is an electroactive byproduct of oxidase-based enzymatic reactions. For example, glucose oxidase can facilitate glucose consumption in the presence of oxygen and produce H_2O_2 as a byproduct. In that regard, selective and sensitive measurement of the H_2O_2 is crucial for high-performance oxidase-based enzymatic sensors.

However, the optimal working potential for H_2O_2 electroanalysis is usually around 0.6 - 0.7 V, which would electro-oxidize other naturally-existing electroactive species (e.g., ascorbic acid and uric acid) and therefore may mask the desired signal. In the majority of wearable enzymatic sensors, a mediating layer (e.g., PB) was often incorporated to reduce the working potential to ~0 V for selective H_2O_2 monitoring. However, Emaminejad et al. [16] recently demonstrated that the use of Prussian Blue for H_2O_2 analysis has fundamental challenges:

1. The susceptibility of the sensor response to ionic level variations. For example, potassium ions are often required to participate in the PB-based electron transfer reaction for charge balance. Accordingly, the sensor response is prone to potassium concentration changes.
2. The poor operational stability. The framework of PB (Fe-CN-Fe), which is responsible for catalytic capability, is prone to degradation at neutral pH (e.g., attack by OH^-) [17].

To this end, the authors provided an alternative sensor development methodology without utilizing the mediating layers. The sensing interface leveraged the high electrocatalytic capability of a platinum-carbon nanotube hybrid layer, the permselective nature of a polymer membrane [18],

and the biocatalytic capability of an enzyme layer (Fig. 1.1B). This methodology was proved in the context of constructing wearable glucose, lactate, and choline sensors, which were selective against a wide panel of interferents. The results showed great potential for the methodology to be employed in the development of wearable electroenzymatic sensors.

1.2.2. Ion-selective sensing interfaces

Sweat contains several important electrolytes, which can be monitored by ion-selective electrodes (ISEs). The sensing interface is constructed by depositing a membrane (e.g., containing sodium ionophore X or calcium ionophore) onto an electrode surface [19, 20]. Since only one ionic species is allowed to pass into the membrane, electrical potential buildup across the membrane reflects the concentration of the respective ion, which can be measured by potentiometric methods. According to the Nernst equation, the output voltage signals are logarithmically related to the concentration of the target ions in the solution.

ISEs have been successfully demonstrated for the analysis of electrolytes in a wearable format, including sodium (Na^+), potassium (K^+), and chloride (Cl^-). Emaminejad et al. demonstrated a sweat analysis wristband, which can extract sweat on-demand and analyze electrolytes in situ [14]. The system was deployed for tracking the chloride levels in cystic fibrosis patients and healthy subjects, where the CF patients showed elevated levels. The authors used electrodeposited poly(3,4-ethylenedioxythiophene) polystyrene sulfonate (PEDOT:PSS) as the ion–electron transducer for the potential drift minimization. In addition, Nyein et al [21]. developed a wearable platform for simultaneous monitoring of calcium (Ca^{2+}) and pH (H^+) in sweat. Calcium ionophore II (ETH 129) was included in the calcium sensors and polyaniline-based pH sensor was fabrication based on electrodeposition of aniline. The results showed that calcium

concentration increases with decreasing pH, which may provide insight into primary hyperparathyroidism or the presence of kidney stones.

1.2.3. Bioaffinity-based sensors

Wearable ion-selective and electroenzymatic sensors are generally used to target biomarkers in the μM - mM concentration range. Unfortunately, this significantly limits the applicability of wearable chemical sensors for the detection of low-concentration biomarkers (e.g., sub-micromolar range). Affinity-based electrochemical sensors, such as electrochemical aptamer-based (EAB) sensors and immunosensors, may provide a solution to this problem. Immunoassays are already quite popular for biomedical applications. Electrochemical immunosensors are antibody-based biosensors for the detection of target biomarkers, such as drugs and hormones. For example, Jang et al. [22] reported an antibody-based cortisol sensor, where the antibody was embedded in a polymer layer (here, poly(styrene-co-methacrylic acid)) formed on the remote gate of a transistor. The sensing interface showed a limit of detection of 1 ng/mL in artificial sweat.

Another promising option may be EAB sensors, which utilize structure-switching nucleic acid aptamers as biorecognition elements. An aptamer is a short and single-stranded DNA or RNA sequence that captures desired targets with high affinity (also known as artificial bioreceptor). A thiol-terminated aptamer can be immobilized onto gold electrode surfaces via self-assembly. Redox-active molecules, such as methylene blue (MB) and ferrocene, could be covalently linked to the other end of the aptamer as signal reporters. The EAB sensors provide a reagentless and substrate-specific biomarker detection platform. The binding of the target molecule to its respective aptamer induces the aptamer conformational changes, which leads to the spatial changes

of the signal reporters and alters the charge transfer rate (Fig. 1.2). This process can be probed by a variety of voltammetric methods, such as square wave voltammetry.

For example, Plaxco et al. developed an EAB-based platform for real-time measurement of small molecules (e.g., doxorubicin, kanamycin, gentamicin, and tobramycin) in awake animals [23]. In another study, the researchers used EAB sensors for continuous measurements in the circulatory systems of living animals [24]. Both works achieved precise molecular measurements at a clinically relevant concentration range. More importantly, the EAB sensors can function properly in human whole blood for several hours with high sensitivity and specificity, which is encouraging for medical applications [25].

1.2.4. Synthetic receptor-based chemical sensors

Biological receptors, such as enzymes, antibodies, and aptamers, often have limited reproducibility and stability during the sensor fabrication process and measurement. Therefore, synthetic receptors (e.g., molecularly imprinted polymers, or MIPs) may offer a promising alternative. A typical MIPs preparation procedure includes polymerization of the selected monomers by light or heat in the presence of a target analyte called the template. When the template is eluted, the structure is left with precisely-molded cavities that can act as artificial structural receptors (Fig. 1.3). Compared to biological receptors, MIPs are more stable in various conditions (e.g., pH, pressure, and temperature) and can function in organic solvents. For example, Parlak et al. reported a molecularly selective nanoporous membrane-based wearable sensing interface on styrene-ethylene-butylene-styrene (SEBS) substrate for the detection of cortisol. The polymeric membrane was formed by the mixture of cortisol (template), methacrylic acid (monomer), ethylene glycol methacrylate (cross-linker), and azobisisobutyronitrile (initiator) with

the aid of UV treatment. After template elution, the membrane with molecular memory was coupled with organic electrochemical transistors (OECTs) for signal transduction. Specifically, the molecularly imprinted polymer-based membrane was deposited on the channel materials (here, PEDOT: PSS) of the organic transistors. The fabricated device was used for both ex-situ and on-body sweat cortisol measurements.

1.2.5. Recognition element-free sensors

Another class of wearable sensors is based on carbon electrodes, which are suitable for the detection of various endo-/exogenous electroactive species (such as caffeine, ascorbic acid, and uric acid) using pulse voltammetric methods like differential pulse voltammetry (DPV). In these devices, electroactive molecules with distinct chemical structures are oxidized or reduced, displaying fingerprint peaks at different voltage positions. For example, Tai *et al.* [26] presented a wearable platform for the detection of caffeine based on the DPV method. Sweat caffeine levels were monitored under various conditions, such as with different caffeine dosages and different measurement times after caffeine intake. The device utilized a carbon working electrode modified with carbon nanotubes and Nafion layers. Additionally, Yang *et al.* [27] reported a laser-engraved graphene sensor for uric acid and tyrosine detection. Levels of uric acid in sweat were reported to be correlated with that in serum. The results showed that uric acid could be considered as a potential biomarker for gout management.

1.3 Access sweat and microfluidic interfaces

To have access to the molecular-level information, a reliable biofluid (e.g., sweat) sampling interface with minimal user intervention needs to be devised and integrated within the

wearable sensing platforms. In the context of wearable chemical sensing systems targeting sweat, exercise is widely utilized for sweat generation [28, 29]. However, while it can be particularly useful in some specific scenarios (e.g., monitoring of athletic performance), sweat monitoring based on exercise may not be suitable for large-scale deployment or for general population monitoring. The requirement for intensive physical activity makes it unrealistic to be used among the neonatal and elderly populations. In that regard, alternative methods of accessing sweat in sedentary settings are required. One such alternative is iontophoresis. Iontophoresis is widely used to stimulate local sweat secretion at a selected site and involves the delivery of stimulatory agonists (e.g., pilocarpine) to the sweat glands with the aid of minimal levels of electrical current [30]. As illustrated in Fig. 1.4, an iontophoresis sweat induction module consists of a pair of electrodes (connected with an external current source) and agonist-embedded hydrogel patches (interfacing electrodes and skin). By miniaturizing the required components in a small footprint, iontophoresis-based sweat induction and analysis can be performed in a wearable format without user intervention [14]. Repeated and prolonged iontophoresis-based sweat stimulation can be further achieved by adjusting the agonist type and iontophoresis operation setting [31, 32].

To facilitate reliable wearable biomarker analysis, various interfaces have been developed for biofluid sampling and storage, including absorbent pads, silicone elastomer-based 2D microfluidic housings, and tape-based 3D microfluidic housings. Absorbent pads were used to interface skin and sensor directly in the early sweat sensor prototypes [28, 33]. The water absorbance feature of the material makes it effective for sweat sampling and manipulation. However, this interface has fundamental challenges, including contamination (from residues of old samples) and lack of sensor protection.

To overcome these challenges, conformal microfluidic modules that are flexible, compact, and scalable need to be integrated in wearable sensing systems. Microfluidic interfaces based on silicone elastomer-based material (e.g., ecoflex, polydimethylsiloxane, PDMS) allow for conformal contact to the human body because they have similar elastic properties to those of skin [24]. As illustrated in Fig. 1.5, the fabrication process of traditional PDMS-based microfluidic devices includes: 1) silicon wafer cleaning, 2-4) photolithograph to transfer the designed pattern onto the silicon wafer and to create a resist-based PDMS mold. 5) PDMS microfluidic channel fabrication, and 6) device assembly. Rogers et al. has demonstrated silicone elastomer-based epidermal microfluidic devices with superior mechanical properties for sweat collection, manipulation, and biomarker analysis [29]. The standard cleanroom-based fabrication scheme renders silicone elastomer-based microfluidic modules with high resolution, accuracy, and scalability [25]. However, this method also has disadvantages as it is time-consuming and comes at high cost due to the heavy involvement of resource-intensive facilities. Also, the conventional bottom-up methodology of cleanroom-based fabrication constrains the microfluidic module spatially to two dimensions, which inherently limits its versatility for bioanalytical operations.

An alternative microfluidic interface for wearable application is the tape-based 3D microfluidic housing, which leverages laser-cutting and vertical assembly of thin layers of tape-based substrates (Fig. 1.6) [26, 27]. For device fabrication, the laser-cutter can be programmed at the software-level (by computer-aided design, or CAD) to rapidly define microfluidic features such as biofluid collection interface, microchannels, and vertical interconnect accesses (VIAs). By leveraging the adhesive property of the substrates and precise positioning of microfluidic VIAs, the 2D-patterned layers can simply be stacked to form leak-free, multilayered 3D architectures. Furthermore, to deliver a diverse set of operations, electrode-patterned layers can be incorporated

during the assembly process to facilitate electrochemical sensing and biofluid actuation functionalities, which will effectively increase the versatility and quantity of bioanalytical operations. A diverse set of wearable bioanalytical applications was demonstrated using this low cost, CAD-3D fabrication scheme [38].

1.4 Reference

1. J. Heikenfeld, A. Jajack, J. Rogers, P. Gutruf, L. Tian, T. Pan, R. Li, M. Khine, J. Kim, and J. Wang, *Lab on a Chip*, 18(2), 217–248, 2018.
2. J. C. Yeo and C. T. Lim, *Microsystems & Nanoengineering*, 2, 16043, 2016.
3. D. R. Seshadri, R. T. Li, J. E. Voos, J. R. Rowbottom, C. M. Alfes, C. A. Zorman, and C. K. Drummond, *NPJ digital medicine*, 2(1), 1–18, 2019.
4. T. Q. Trung and N. Lee, *Advanced materials*, 28(22), 4338–4372, 2016.
5. J. Heikenfeld, A. Jajack, B. Feldman, S. W. Granger, S. Gaitonde, G. Begtrup, and B. A. Katchman, *Nature biotechnology*, 37(4), 407–419, 2019.
6. J. P. Bantle and W. Thomas, *Journal of Laboratory and Clinical Medicine*, 130(4), 436–441, 1997.
7. J. Kim, S. Imani, W. R. de Araujo, J. Warchall, G. Valdés-Ramírez, T. R. L. C. Paixão, P. P. Mercier, and J. Wang, *Biosensors and Bioelectronics*, 74, 1061–1068, 2015.
8. J. Kim, M. Kim, M. Lee, K. Kim, S. Ji, Y. Kim, J. Park, K. Na, K. Bae, H. K. Kim, F. Bien, C. Y. Lee, and J. Park, *Nature Communications*, 8, 14997, 2017.
9. A. J. Bandodkar, I. Jeerapan, and J. Wang, *ACS Sensors*, 1(5), 464–482, 2016.
10. E. Bakker and M. Telting-Diaz, *Analytical Chemistry*, 74(12), 2781–2800, 2002.
11. C. McDonagh, C. S. Burke, and B. D. MacCraith, *Chemical reviews*, 108(2), 400–422,

2008.

12. N. V Lavrik, M. J. Sepaniak, and P. G. Datskos, *Review of scientific instruments*, 75(7), 2229–2253, 2004.
13. W. He, C. Wang, H. Wang, M. Jian, W. Lu, X. Liang, X. Zhang, F. Yang, and Y. Zhang, *Science advances*, 5(11), eaax0649, 2019.
14. S. Emaminejad, W. Gao, E. Wu, Z. A. Davies, H. Y. Y. Nyein, S. Challa, S. P. Ryan, H. M. Fahad, K. Chen, and Z. Shahpar, *Proceedings of the National Academy of Sciences*, 114(18), 4625–4630, 2017.
15. A. Hauke, P. Simmers, Y. R. Ojha, B. D. Cameron, R. Ballweg, T. Zhang, N. Twine, M. Brothers, E. Gomez, and J. Heikenfeld, *Lab on a Chip*, 18(24), 3750–3759, 2018.
16. X. Cheng, B. Wang, Y. Zhao, H. Hojaiji, S. Lin, R. Shih, H. Lin, S. Tamayosa, B. Ham, and P. Stout, K. Salahi, Z. Wang, C. Zhao, J. Tan, and S. Emaminejad, *Advanced Functional Materials*, 1908507, 2019.
17. R. Koncki, *Critical reviews in analytical chemistry*, 32(1), 79–96, 2002.
18. X. Wen, B. Wang, S. Huang, M.-S. Lee, P.-S. Chung, Y. T. Chow, I.-W. Huang, H. G. Monbouquette, N. T. Maidment, and P.-Y. Chiou, *Biosensors and Bioelectronics*, 131, 37–45, 2019.
19. Y. Yang and W. Gao, *Chemical Society Reviews*, 48(6), 1465–1491, 2019.
20. A. J. Bandodkar and J. Wang, *Trends in biotechnology*, 32(7), 363–371, 2014.
21. H. Y. Y. Nyein, W. Gao, Z. Shahpar, S. Emaminejad, S. Challa, K. Chen, H. M. Fahad, L.-C. Tai, H. Ota, and R. W. Davis, *ACS nano*, 10(7), 7216–7224, 2016.
22. H.-J. Jang, T. Lee, J. Song, L. Russell, H. Li, J. Dailey, P. C. Searson, and H. E. Katz, *ACS applied materials & interfaces*, 10(19), 16233–16237, 2018.

23. N. Arroyo-Currás, J. Somerson, P. A. Vieira, K. L. Ploense, T. E. Kippin, and K. W. Plaxco, *Proceedings of the National Academy of Sciences*, 114(4), 645–650, 2017.
24. B. S. Ferguson, D. A. Hoggarth, D. Maliniak, K. Ploense, R. J. White, N. Woodward, K. Hsieh, A. J. Bonham, M. Eisenstein, and T. E. Kippin, and K. W. Plaxco, *Science translational medicine*, 5(213), 2013.
25. Y. Xiao, A. A. Lubin, A. J. Heeger, and K. W. Plaxco, *Angewandte Chemie International Edition*, 44(34), 5456–5459, 2005.
26. L. C. Tai, W. Gao, M. Chao, M. Bariya, Q. P. Ngo, Z. Shahpar, H. Y. Y. Nyein, H. Park, J. Sun, Y. Jung, E. Wu, H. M. Fahad, D. H. Lien, H. Ota, G. Cho, and A. Javey, *Advanced Materials*, 30(23), 2018.
27. Y. Yang, Y. Song, X. Bo, J. Min, O. S. Pak, L. Zhu, M. Wang, J. Tu, A. Kogan, and H. Zhang, *Nature biotechnology*, 1–8, 2019.
28. W. Gao, S. Emaminejad, H. Yin, Y. Nyein, S. Challa, K. Chen, A. Peck, H. M. Fahad, H. Ota, H. Shiraki, D. Kiriya, D. Lien, and G. A. Brooks, R.W. Davis, and A. Javey, *Nature*, 529(7587), 509–514, 2016.
29. A. Koh, D. Kang, Y. Xue, S. Lee, R. M. Pielak, J. Kim, T. Hwang, S. Min, A. Banks, and P. Bastien *et al.* *Science translational medicine*, 8(366), 366ra165-366ra165, 2016.
30. E. P. Carter, A. D. Barrett, A. F. Heeley, and J. A. Kuzemko, *Archives of disease in childhood*, 59(10), 919–922, 1984.
31. P. Simmers, S. K. Li, G. Kasting, and J. Heikenfeld, *Journal of dermatological science*, 89(1), 40–51, 2018.
32. P. Simmers, Y. Yuan, Z. Sonner, and J. Heikenfeld, *Biomicrofluidics*, 12(3), 34101, 2018.

33. H. Yin, Y. Nyein, W. Gao, Z. Shahpar, S. Emaminejad, S. Challa, K. Chen, H. M. Fahad, L. Tai, H. Ota, R. W. Davis, and A. Javey, *ACS Nano*, 10(7), 7216-7224, 2016.
34. Y. Liu, M. Pharr, and G. A. Salvatore, *ACS nano*, 11(10), 9614–9635, 2017.
35. D. Qin, Y. Xia, and G. M. Whitesides, *Nature protocols*, 5(3), 491, 2010.
36. P. Nath, D. Fung, Y. A. Kunde, A. Zeytun, B. Branch, and G. Goddard, *Lab on a Chip*, 10(17), 2286–2291, 2010.
37. D. I. Walsh III, D. S. Kong, S. K. Murthy, and P. A. Carr, *Trends in biotechnology*, 35(5), 383–392, 2017.
38. H. Lin, Y. Zhao, S. Lin, B. Wang, C. Yeung, X. Cheng, Z. Wang, T. Cai, W. Yu, K. King, J. Tan, K. Salahi, H. Hojajji, and S. Emaminejad, *Lab on a Chip*, 19(17), 2844–2853, 2019.

Chapter 2. Thin hydrogel-coated sensors for natural perspiration sampling and in-situ electrochemical analysis

2.1 Introduction

Recent advances in miniaturized electronics, microfluidics, and electrochemical sensing platforms have paved the path for the realization of chemo/bio-sensing networks geared toward general population health and wellness monitoring [1-4]. To this end, a sweat-based sensing modality presents a great potential for the integration into such networks, as it provides non-invasive access to molecular-level information, enabling insight into the body's dynamic chemistry [5-7]. However, realizing effective sweat sampling remains a fundamental challenge in non-invasive chemo/bio-sensing [8]. Previous studies have mainly relied on either physical or chemical stimulation procedures (e.g., exercise [9-10], heat [11], and iontophoresis [12]) to induce sweat production in substantial volumes ($\sim 50 \mu\text{L}$). While useful for infrequent analysis in laboratory settings, challenges remain when implementing these methods in the context of (semi)continuous measurements: exercise requires strenuous physical activity, which may not be suitable for all potential users (especially the bedridden, neonatal, or elderly populations); heat can lead to exhaustion and discomfort, which could cause noncompliance if used in a device for patients; and iontophoresis has numerous challenges related to the integration of device- and circuit-level stimulating components, which are currently being addressed [13]. It is also worth noting that the analyte concentration in sweat has been shown to be sweat gland secretory rate-dependent [14], which, in the absence of corrective calibration mechanisms, leads to distortion in the biomarker measurements when relying on stimulation-based sweat sampling.

Given the challenges of these sampling methods, alternative methods of accessing sweat biomarkers may warrant exploration. One such alternative is naturally occurring/background thermoregulatory perspiration (hereinafter, referred to as natural perspiration). Natural perspiration-based sampling eliminates the need for active stimulation and provides a stable secretion rate (on the order of 1 nL/min per gland) within the time window of sampling [13]. This minimizes the confounding effect of sweat rate variability and leads to more accurate analysis. Furthermore, owing to its low secretion rate, natural perspiration is speculated to give adequate time for the low-membrane-permeability analytes to partition from blood to sweat, and thus sweat-blood correlation can be established for a wider-range of biomarkers [15-16]. While this phenomenon has not been widely used for bioanalytical device development, academic forensic science studies have already demonstrated its utility in residual fingerprint analysis for simultaneous rendering of biochemical and user-identification information [17]. In one respect, drugs or metabolites of target compounds can be extracted from the sweat, yielding information about the individual's consumption of illicit substances with the added potential to make inferences regarding the individual's general health state [18].

To fully realize the potential of natural perspiration for non-invasive health monitoring applications, two fundamental challenges related to biomarker sampling and sensing must be addressed. First, instantaneous secreted sweat droplet sampling is challenging because of its low flow rate and associated volume of secretion, and such sampling requires sweat collection by accumulation over a period of time in suitable interfaces/reservoirs to facilitate effective analyte partitioning and collection from sweat glands. Second, in-situ electrochemical techniques (which are commonly used for sweat analysis at the "point-of-person") require a reliable medium to

envelop and protect sensing electrodes as well as facilitate analyte transport to those electrodes for detection.

Previous work demonstrating analyte sampling interfaces for natural perspiration from the skin can generally be categorized by interface type (either dry or wet). Dry interfaces (like unwetted filter paper or the commercial Pharm-ChekTM skin patches) typically require longer collection periods (on the order of days), and are thus more useful in obtaining a binary presence metric indicating if a compound has accumulated to sufficient levels for detection [19-20]. Hydrated interfaces (like wetted filter paper or hydrogels), on the other hand, are better suited for health monitoring devices and terminals aiming to study and characterize pharmacokinetic and metabolic profiles of the subjects due to their shorter sampling times and improved partitioning efficiency (greater analyte collection) [21-23]. Both interface types, however, are commonly used only as reservoirs for subsequent analysis in a decoupled manner with bulky laboratory instruments (e.g., mass spectrometers).

Here, we devise a thin hydrogel (TH) patch for simultaneous natural perspiration collection and in-situ electrochemical analysis (Fig. 2.1A). To characterize THMP's natural perspiration sampling performance, caffeine and lactate were selected as two representative target molecules. The choice of caffeine was motivated by its therapeutic potential for the treatment of airway obstruction and apnea of prematurity [24-25] and the fact that it is a xenobiotic. We particularly exploit its xenobiotic nature to perform controlled studies for determining optimal sampling conditions and demonstrating the utility of the approach for tracking dosage levels and metabolic patterns. The choice of lactate was motivated by its clinical significance in a variety of applications [26] and the fact that lactate-targeting sensors have been extensively explored for sweat analysis [27-28].

The devised TH was then coupled with electrochemical sensors to form TH-sensors for in-situ biomonitoring and touch-based sensing. To this end, a dedicated sensor design and a signal interpretation framework must be developed to account for the unique—yet previously unexamined—analyte mass transport behavior at hand. To elaborate, unlike the conventional sample-to-answer biochemical sensing scenarios, where the analyte concentration in a given biofluid sample is directly measured as the primary quantity of interest (in a quasi-static setting)—in touch-based TH-sensing, the continuous epidermal influx of analytes into the hydrogel is primarily measured. The development of this framework is crucial for guiding the sensor development efforts, decoupling the influence of confounding factors, and ultimately translating the TH-sensor readouts to physiologically meaningful measurements.

Addressing such TH-sensing limitations, here, we present a dedicated framework for TH-sensor design and signal interpretation and illustrate its physiological utility by augmenting it with newly developed specialized TH-sensors. We particularly formulated and validated the proposed framework via convergent mass transport modelling, simulation, and in-vitro characterization (using an artificial fingertip setup). Critical for rendering physiologically relevant readouts, this framework was utilized to decouple the signal-distorting effect of the pressing force variability—a previously overlooked but major confounder—which is intrinsic to the touch-based HMI modality. Furthermore, guided by this framework, we thinned-down the hydrogel interface to minimize the required fingertip/TH-sensor contact time (~ 30 s) well below the wait/contact time reported in previous TH-sensor studies (on the order of minutes) [29,30].

Our TH-sensor development efforts focused on targeting ethanol (for alcohol monitoring) and acetaminophen (APAP, a widely used analgesic medication), as example analytes with high significance in personal biomonitoring. For example, monitoring of alcohol could prevent

personal/societal harmful outcomes such as alcohol abuse and driving under the influence (DUI) [31]. Also, monitoring of APAP may be particularly beneficial in promoting patient compliance and safety, given that APAP supratherapeutic administration is the leading cause of liver failure in the United States [32]. We specifically developed an amperometric TH-sensor to enzymatically measure ethanol and an interference-free voltammetric TH-sensor to target APAP. Particularly noteworthy is the importance of the devised voltammetric TH-sensing methodology in broadly enabling the detection of electroactive biomarkers such as many pharmaceuticals in the presence of non-targeted interfering electroactive species.

2.2. Experimental Section

2.2.1. Materials and Reagents

Agarose, bovine serum albumin (BSA), glutaraldehyde solution (25 wt.%), *m*-phenylenediamine, *d*-(+)-glucose, sodium L-lactate, potassium chloride (KCl), sodium chloride (NaCl), uric acid (UA), chitosan (high molecular weight), *L*-tyrosine, *L*-tryptophan, ascorbic acid (AA), Nafion perfluorinated resin solution (5 wt.%), alcohol oxidase (AOx) from *Pichia pastoris* (10-40 units/mg protein), chloroplatinic acid hexahydrate ($\text{H}_2\text{PtCl}_6 \cdot 6\text{H}_2\text{O}$), formic acid, sulfuric acid (H_2SO_4), and APAP were purchased from Sigma-Aldrich. Phosphate-buffered saline (PBS, 1 \times , pH 7.2; Gibco), ethanol, and all the reagents used in the high-performance liquid chromatography were purchased from Fisher Scientific. Polyethylene terephthalate (PET, 100 μm thick) was purchased from MG Chemicals. Double-sided tape (170 μm thick, 9474LE 300LSE) and Scotch single-sided self-seal laminating sheets were purchased from 3M Science. BDDE sensor (reference electrode: silver; counter electrode: carbon) was purchased from Metrohm USA. Silver–silver chloride (Ag/AgCl) ink was purchased from Ercon Incorporated. Polycarbonate

membrane (thickness: 10 μm , pore size: 0.2 μm , pore density: $3 \times 10^8 \text{ cm}^{-2}$) was purchased from Sterlitech. 10 kDa molecular weight cut-off (MWCO) centrifugal filters (Amicon Ultra-0.5) were purchased from Sigma-Aldrich. CF1 absorbent pads were purchased from GE Healthcare Bio-Sciences (PA, USA). Espresso containing 75 mg caffeine per shot used for caffeine testing in human subjects was purchased from Peet's Coffee (CA, USA).

2.2.2. TH Fabrication

The thin hydrogel was prepared using a vertically-assembled mold, which consists of a glass substrate, a double-sided tape layer, and a PET capping layer. PET and tape layers were patterned by laser cutting (VLS2.30, Universal Laser Systems) to form hydrogel chambers and access ports. Hydrogel was prepared by dissolving agarose powder (2 wt.%) in a PBS solution (80 °C water bath for 20 min). The solution was then injected into the assembled mold. Following the sufficient hydrogel gelation (~ 10 min), the tape/PET layers were removed, and the hydrogel was picked up. To further decrease its thickness, the hydrogel was dried for 3 hours in an ambient environment, and then rehydrated with PBS solution. The thickness of the thin hydrogel was measured to be $220 \pm 20 \mu\text{m}$. The hydrogel can be stored in a 100% humidity environment for at least one week before use. In our studies, the hydrogels were used within 10 min post-storage and at room conditions (temperature and humidity).

2.2.3. TH-sensor Construction

The ethanol sensor was fabricated by modifying the gold electrodes, which were patterned on a PET substrate with the aid of a shadow mask (200-nm-thick gold on a 30 nm-thick chromium as an adhesion layer, working electrode diameter: 1.2 mm). All the electrochemical

deposition/measurement experiments were performed using CHI660E or CHI1040C electrochemical workstation (CH Instruments, Inc.). First, PtNPs were deposited on the gold electrode via an amperometric method (-0.2 V vs. Ag/AgCl, 720 s). The PtNP deposition solution contained 2.5 mM H_2PtCl_6 and 1.5 mM formic acid. Then a PPD layer was electrochemically deposited onto the PtNPs/Au electrode (0.85 V vs. Ag/AgCl, 120 s) using a PBS solution containing 5 mM m-phenylenediamine. To immobilize AOX, 1.2 μL AOX-BSA solution (34.67 mg/mL AOX and 16.67 mg/mL BSA) was dropped onto the PPD/PtNPs/Au electrode and dried for 30 min at room temperature. The electrode was further coated by 1.2 μL 0.5 wt.% chitosan solution, which was prepared by dissolving chitosan in a 0.25% acetic acid solution at 60 °C for 30 min. Finally, a 1.6 μL 0.6% glutaraldehyde solution was dropped on top of the sensor surface to crosslink the AOX, BSA and chitosan. All sensors were dried at 4 °C overnight before use. The reference electrode was fabricated by dropping ~ 2 μL Ag/AgCl ink onto the gold substrate, followed by drying at 65 °C for 30 min. The reference electrode was fabricated before the enzyme coating step to prevent the heat-induced AOX deactivation.

The APAP sensor fabrication was detailed in Chapter 5. The BDDE was cleaned by repetitive cyclic voltammetry (CV) scanning in 0.5 M H_2SO_4 solution. The CV scanning was performed in the potential range of -0.5 V to 1.5 V (vs. Ag/AgCl; scan rate: 0.5 V/s) until a stable voltammogram was obtained. Nafion coating was performed by drop casting 1.8 μL 5 wt.% Nafion solution onto the working electrode, followed by a drying step in an ambient environment. To form TH-sensors, freshly prepared hydrogels were mounted onto the corresponding electrochemical sensors right before testing.

2.2.4. Characterization of TH-based natural perspiration sampling

For natural perspiration sampling intended for caffeine analysis, participants with regular caffeine intake (e.g., routine or daily consumption of caffeinated beverages) were excluded to avoid confounding factors (e.g., caffeine accumulation in body) and all the participants were required to abstain from the consumption of food, beverages, and drugs containing caffeine for 24 hours prior to the experiment. The skin sampling regions of interest were washed with hand soap sheets (Travelon, IL, USA) and DI water followed by wiping with Kimwipes containing 70% IPA. A TH or absorbent pad was placed on the skin for five minutes for sweat sampling, and a polyethylene plastic film was used to cover the device to avoid evaporation. Given that the natural perspiration rate, on the high end, is on the order of $0.4 \text{ mg/cm}^2/\text{min}$ [33], the incremental volume contribution of natural perspiration to the TH is less than $1 \text{ }\mu\text{L}$. As the original TH volume is $\sim 8 \text{ }\mu\text{L}$, the volumetric contribution by natural perspiration results in dilution by a factor of ~ 10 , allowing to establish a linear relationship between the collected analyte amount and the corresponding analyte concentration in perspiration.

2.2.5. Lactate Quantification with Lab Instrument

After natural perspiration sampling, the TH or absorbent pad was placed into an Eppendorf tube containing $100 \text{ }\mu\text{L}$ of acetate buffer (0.01 M , $\text{pH} = 5$) and the tube was sonicated for five minutes at room temperature for the extraction of the target molecules. The lactate concentration in the tube was quantified directly with the YSI 2900 analyzer (YSI Incorporated, OH, USA) in duplicate and the average value was used. Amount of lactate sampled per unit area was determined from the concentrations in the extraction buffer, extraction buffer volume, and the area of the TH or absorbent pad.

2.2.6. *Caffeine quantification with liquid chromatography – tan-dem mass spectrometry (LC-MS/MS).*

The amount of caffeine sampled with the TH or absorbent pad was measured by LC-MS/MS with multiple reaction monitoring (MRM) technique. ^{13}C isotopically labeled caffeine (caffeine- $^{13}\text{C}_3$) was used as the internal standard (IS). For calibration, different concentrations of caffeine were spiked into water (Optima™ LC/MS grade) to make standard solutions of 0.0, 1.0, 2.0, 5.0, 10.0, 50.0, 100.0, 200.0 nM. For the analysis of real samples, the perspiration-sampled TH or absorbent pad was placed into an Eppendorf tube containing 200 μL of acetate buffer (0.01 M, pH = 5) and the tube was sonicated for 5 min at room temperature for target molecules extraction. Molecular weight cutoff (MWCO) filtering was used to remove any particulate matter from the sample. 150 μL of the standard solution or real sample extraction was mixed with 1.5 μL 10.0 μM IS (to reach a final IS concentration of 0.1 μM), loaded into a 10 kDa MWCO filter, and centrifuged at $14,000 \times g$ for 10 min. The low molecular weight filtrate was then transferred into an autosampler vial for caffeine quantification.

Agilent 1200 series HPLC (Agilent Technologies, CA, USA) equipped with HTS PAL autosampler (CTC Analytics, MN, USA) was coupled to an API 4000 triple quadrupole mass spectrometer (Sciex, ON, Canada) for MRM experiments. Zorbax 300 SB-C18 column (0.5 ID \times 150 mm L, 5 μm , Agilent Technologies) was used for separation. Solvent A was water with 0.1% formic acid and solvent B was acetonitrile with 0.1% formic acid. Flow rate was 400 $\mu\text{L}/\text{min}$ with the following gradient: 5% B (0-0.5 min), from 5 to 90% B (0.5-5.5 min), 90% B (5.5-8.5 min), from 90 to 5% B (8.5-9.0 min), 5% B (9.0-11.0 min). Sample vials were maintained at 4 $^{\circ}\text{C}$ in the autosampler tray. 20 μL of sample was loaded onto the column each time.

The instrument was operated in MRM mode with the following m/z transitions: 195.2→138.1 for caffeine and 198.1→140.1 for caffeine-¹³C₃. The declustering potential (DP), entrance potential (EP), collision energy (CE), and collision cell exit potential (CXP) were optimized at 71 V, 10 V, 27 V, and 8 V for caffeine, and 86 V, 10 V, 27 V, and 8 V for caffeine-¹³C₃, respectively. Ionspray voltage and temperature were 5500 V and 400 °C, respectively. Collision gas, curtain gas, and ion source gas 1 and 2 were set at 4, 30, 30, and 50 psi, respectively.

2.2.7. Microfluidic artificial fingertip fabrication and characterization

The construction of the microfluidic artificial fingertip builds upon a previously reported work by Heikenfeld et al. [34]. Specifically, multiple layers were vertically aligned on a polystyrene substrate: 1) two layers of double-sided tape and a single PET layer to form the microfluidic chamber; 2) a single layer of double-sided tape with laser-patterned μ-pores; 3) a porous polycarbonate film; and 4) a scotch tape layer with laser-patterned μ-pores. All the geometric features were defined by AutoCAD (Autodesk) and realized by laser cutting. The sensor interfacing area of the artificial fingertip was adjusted according to the tested sensors' dimensions. Upon its construction, the artificial fingertip was connected to a programmable syringe pump (PHD ULTRATMCP, Harvard Apparatus), which delivered input fluid with different compositions and at adjustable flow rates (300-1000 nL/min/cm²). To monitor the hydraulic pressure of the developed artificial fingertip, the assembled device was connected to a pressure sensor (Blood Pressure Transducers, APT 300, Harvard Apparatus) and a transducer amplifier module (TAM-D, Harvard Apparatus).

2.2.8. Simulation of analyte flux

Finite element analysis (FEA) software, COMSOL 5.2, was used to simulate the analyte concentration profile within a hydrogel layer for different levels of analyte flux inputs. In the simulation software, “transport of diluted species” simulation package was employed in the context of a 3D hydrogel structure with the same size used in the experiment. Input analyte was introduced from the top surface of the hydrogel with the same flux levels as the ethanol TH-sensor ex-situ testing experiment (concentration range: 0-10 mM, flow rate: 320 nL/min/cm²). The analyte flux for the other surface boundaries was set to zero. The diffusion coefficient of target analyte (here, ethanol) in the hydrogel was set as $9 \times 10^{-6} \text{ cm}^2 \text{ s}^{-1}$ [35]. The analyte concentration at the vicinity of the sensor surface (at its midpoint) was extracted to infer the sensor’s response (assuming a mass transport limitation scenario).

2.2.9. Ex-situ TH-sensor characterization

The sensitivity and the selectivity of ethanol and APAP sensors were characterized using a standard electrochemical cell (reference electrode: Ag/AgCl, counter electrode: platinum) in the PBS solution. The ethanol sensor was tested by performing amperometric measurement at 0.5 V vs. Ag/AgCl. The APAP sensor was tested using differential pulse voltammetry (DPV, increment: 5 mV, amplitude: 50 mV, pulse width: 0.1 s, sampling width: 16.7 ms, and pulse period: 0.5 s). The ex-situ TH-sensor characterization was performed using the artificial fingertip with the same electrochemical testing methods. For the ethanol TH-sensor, the amperometric response of the TH-sensor was recorded continuously. After a stable amperometric baseline was obtained, the TH-sensor was mounted onto the artificial fingertip. The measured amperometric current was linearly fitted (for the duration of measurement of 0-60 s, after contacting the artificial fingertip). The

derived current slope was considered as the sensor signal. For the APAP TH-sensor, a DPV scan was performed 3 min after mounting the sensor onto the artificial fingertip. The baseline estimation and voltammetric signal extraction were performed using MATLAB (MathWorks) following our reported analytical framework (detailed in Chapter 4). For all the TH-sensor testing, a new hydrogel was used for each measurement. To characterize the effect of pressing force, weights were used to emulate force exertion with different strengths.

2.2.10. Institutional Review Board (IRB) Approval for Human Subject Testing:

The conducted human subject experiments were performed in compliance with the protocols that have been approved by the Institutional Review Board at the University of California, Los Angeles (IRB No. 17-000170). All subjects gave written informed consent before participation in the study.

2.3. Naturally perspired analyte sampling

In order to set up a framework for natural perspiration-based analyte sampling, we expand upon the first-order microfluidic models of eccrine sweat glands presented in previous studies [16]. As shown in Fig. 2.1B, P_{in} is the varying hydrostatic-osmotic pressure (originating from the accumulation of Na^+ and Cl^- ions in the secretory lumen), which pumps sweat from the glands to the pores on the skin surface, forming sweat droplets. R_c , R_d , and R_s are the fluidic resistances of the upper coiled duct, the dermal duct, and the secretory coil, respectively. The surface tension-induced Laplace pressure, P_L , acts to oppose sweat secretion, where the surface tension corresponds to that of a sweat droplet with a finite radius of curvature forming on the surface of the skin. For natural perspiration to occur, P_{in} must be increased beyond P_L . Once perspiration has

occurred, P_{in} will be reduced (due to the loss of the accumulated Na^+ and Cl^- ions upon secretion) and must rise above the P_L threshold again to induce the next cycle of the sweat secretion, giving rise to the pulsatile behavior of natural perspiration. This behavior is consistent with previous observations [16] and our own examination of natural perspiration, where the naturally perspired droplets were generated, and then evaporated.

To eliminate the P_L pressure barrier, a hydrogel-based collection interface is devised. By creating a continuous hydrophilic fluidic path connecting the secretory coil and sampling reservoir, the hydrogel effectively reduces P_L to zero (Fig. 2.1B, right). In this way, even a small P_{in} build-up will result in sweat secretion that can be utilized for analyte collection by the hydrogel. In addition, due to its aqueous nature, the hydrogel interface also serves to facilitate diffusion of analytes from sweat to the reservoir. These two features render the hydrogel an effective collection reservoir for capturing analyte flux. To illustrate the analyte collection efficacy of the devised TH, perspiration sampling experiments targeting caffeine and lactate (as two representative molecules) were performed. The caffeine sampling experiments were performed two hours after the consumption of caffeinated beverages. The analyte collection capability of the TH was compared with that of the dry absorbent pad (which can be effectively considered as an open-air sampling interface in the described model, laser cut to be the same size of the TH). For each target, the two sampling media were placed side-by-side on a subject's fingertip. After sampling, the two media were immersed in acetate buffer solutions for analyte extraction followed by quantification. Caffeine concentration levels were measured by LC-MS/MS and lactate concentration levels were measured by a YSI analyzer. The analyte sampling characterization results for both molecules indicated that the hydrogel interface sampled approximately three times as much analytes as the

dry pad interface (Fig. 2.1C,D), which is in agreement with the described first-order model and informs the enhanced analyte collection capability of the TH.

To further validate the suitability of TH for analyte sampling, it was deployed on eight different body sites for caffeine sampling on three subjects. Figure 2.2A shows that the hydrogel micropatch was able to collect detectable (by LC-MS/MS) levels of xenobiotics for most of the sampling points. In particular, for all the subjects, the highest amounts of analytes (per unit area) were collected from the fingertips among the investigated body sites. This observation may be attributed to the fact that fingertips have the highest density of eccrine sweat glands [36] and/or that blood capillaries lie in close proximity to the fingertip's sweat glands [37]. From this investigation, fingertips were determined to be the optimal site for sampling due to their higher analyte yield, and thus this site was used to conduct the subsequent analyte collection characterization experiments.

To illustrate the utility of the TH for natural perspiration sampling, we demonstrated its capability to track different caffeine intake dosage levels in a subject. Accordingly, the subject was instructed to consume caffeine-based beverages with four different caffeine amounts (0 mg, 75 mg, 150 mg, and 225 mg) and at least 24 hours of wash-out period was included in between to avoid the carryover effect. TH-based sampling was performed two hours after each caffeine intake. As shown in Fig. 2.2B, the quantification results indicate that the amount of caffeine sampled in the hydrogel increased linearly with increasing dosage, which in turn illustrates the reliability of the TH-based sampling method. Furthermore, we employed TH to characterize the temporal metabolic pattern of caffeine (as a xenobiotic). Accordingly, TH-based sampling on a subject's fingertip was performed at 30-min intervals before and after the consumption of a beverage containing 150 mg of caffeine. As shown in Fig. 2.2C, for this subject, the sampled caffeine peaked

around 2.5 hours after caffeine intake followed by a steady decline. Similar experiments with 1-hour sampling intervals were also conducted for three additional subjects, where the captured caffeine metabolic patterns (Fig. 2.3) were consistent with that observed in the 30-minute interval study. On a broader level, the results also inform the feasibility of utilizing this approach to construct the pharmacokinetic pro-files of xenobiotic compounds including pharmaceutical drugs. As a complementary test, to evaluate the TH's ability to render an endogenous compound's temporal profile, TH-based fingertip sampling was performed targeting lactate. Accordingly, one subject was monitored at 30-minute intervals in a sedentary state (where no significant change in sweat lactate level was expected). The results indicate that sampled lactate by the TH was relatively stable over the duration of the test (Fig. 2.2D), validating the consistency of the analyte sampling capability of the TH.

2.4. Formulation of an epidermal TH-sensing signal interpretation framework

To acquire physiologically interpretable TH-sensor readouts, we formulated a generalizable TH-sensing signal interpretation framework. This framework specifically accounts for the unique mass transport context at hand, involving the continuous epidermal influx of analytes into the hydrogel medium, and subsequently onto the sensing surface. For simplicity and toward building intuition, we first assume that epidermally-delivered analytes are diffused immediately and uniformly within the hydrogel. In this setting, the analyte concentration in the hydrogel C_H during the sampling/measurement time t can be described as:

$$C_H(t) = \frac{N(t)}{V_H + V_T(t)} \quad (1)$$

, where N denotes the amount of analytes in the hydrogel, V_H denotes the original volume of the hydrogel, and V_T accounts for the added volume contributed by transepidermal processes such as

the natural perspiration and water loss. Assuming that natural perspiration is the dominant process for epidermal analyte flux, C_H can be represented as:

$$C_H(t) = \frac{A_H \cdot \int_0^t C_p(\tau) \cdot R_p(\tau) d\tau}{V_H + A_H \cdot \int_0^t R_p(\tau) d\tau} = \frac{A_H \cdot \int_0^t J(\tau) d\tau}{A_H h + A_H \cdot \int_0^t R_p(\tau) d\tau} \quad (2)$$

In this equation, A_H and h denote the hydrogel's fingertip facing-area and height, respectively. Further, C_p and R_p denote the perspired analyte concentration and natural perspiration rate (secreted volume per unit area and time) correspondingly, where their product effectively captures the analyte influx (J) in our case. Given the presumed relatively short sampling time, C_p , R_p , and subsequently, J can be considered to be constant during the course of sampling, or equivalently, representable by their average values. Following the same assumption, the contributed volume by the perspiration can be neglected as compared to the volume of the hydrogel. In this way, the derived expression for C_H can be simplified as:

$$C_H(t) = \frac{J \cdot t}{h} \quad (3)$$

Examining this equation can yield insight in a number of ways. First, considering the inherent proportionality of the underlying sensor readout to C_H , and J to C_p , this equation allows for meaningfully correlating the sensor readout to the perspired analyte concentration, which serves as a non-invasive proxy measure of the analyte's circulating level. Second, noting the time linear-dependency of the sensor readout motivates defining the signal based on the first-derivative of the sensor readout with respect to time. This definition allows for both extracting the analyte flux information and eliminating the influence of relatively time-independent confounding factors. And third, this equation illustrates that by thinning down the hydrogel (decreasing h), we can effectively amplify the signal, which could be particularly useful in quantifying analytes with low circulating levels (e.g., many pharmaceuticals and hormones).

Revisiting our formulated model, we can more specifically account for analyte diffusion within the hydrogel by considering the time that it takes for the introduced analytes to diffuse to the sensing surface (t_D). In our context, t_D can be estimated following Fick's law:

$$t_D \approx \frac{h^2}{2D} \quad (4)$$

, where D is the analyte diffusion coefficient within the hydrogel. This time scale manifests as a lag-time between the fingertip contact and the observed sensor response, indicating another advantage of using thin hydrogels in TH-sensing (i.e., facilitating rapid response).

To validate our simplified model, we performed a finite element analysis (FEA), simulating the analyte transport behavior (using COMSOL software). We primarily simulated the analyte concentration profile (within the hydrogel layer) across time for different levels of analyte flux inputs. As shown in Fig. 2.4A, for a given input flux, after an initial lag-time (related to t_D), the analyte concentration at the vicinity of the sensing surface increases linearly with time. The observed slope for each case is proportional to the input flux (Fig. 2.4B). We further extended the simulation to capture the influence of hydrogel thickness on the TH-sensing performance. As shown in Fig. 2.4C, a thinner hydrogel results in a reduced time-lag and an enhanced on-sensor flux—aligned with the conclusions derived from our simplified model. Guided by these results, in our TH-sensor fabrication effort, we particularly thinned down the hydrogel layer (by introducing a rehydration step in the fabrication process) to enhance the sensor performance.

2.5. Development of a microfluidic artificial fingertip for characterization and empirical validation of the TH-sensors and signal interpretation framework

To empirically validate the presented model and characterize the subsequently developed TH-sensors in an ex-situ setting, we created a microfluidic artificial fingertip, which emulates the

analyte flux on a fingertip via natural perspiration (Fig. 2.4D,E, Fig. 2.5). This setup is particularly useful for characterizing the TH-sensors' responses with respect to the analyte-related parameters (e.g., concentration, mass transport delivery rate) and measurement-specific influential factors (e.g., fingertip mechanical contact force). The developed artificial fingertip consists of: 1) a microfluidic chamber to facilitate the delivery of the input fluids (with dynamically-varying composition and at adjustable flow rates) via a programmable pump (mimicking the thermoregulatory sweat secretion by the secretory coil); 2) a pressure regulation layer [37], mimicking the highly fluidically-resistive sweat duct, to render a stable low flow rate ($< 1 \mu\text{L}/\text{min}/\text{cm}^2$, corresponding to the natural perspiration rate [38]); and 3) a laser-patterned pore layer (with the pore size comparable with the sweat duct diameter, $\sim 80 \mu\text{m}$ [39]), mimicking the fingertip skin surface (to be interfaced with the TH-sensor). To characterize the constructed artificial fingertip from the standpoint of fluid secretion, we monitored the hydraulic pressure across the microfluidic chamber, under various input flow rates. For each of the flow rates, a relatively flat pressure profile was measured, indicating the artificial fingertip's microfluidic capability to reliably deliver the intended analyte flux within the expected range of secretion rate.

2.6. Development and ex-situ characterization of TH-sensors for epidermal biosensing

Recognizing the identical biofluidic origin of our target analytes in our epidermal TH-sensing and conventional sweat sensing contexts, to develop our TH-sensors, we adapted electrochemical sensing methodologies that enable reliable analyte quantification in the complex sweat matrix. Accordingly, to construct the underlying sensing surface of the ethanol TH-sensor (Fig. 2.4F), we utilized a mediator-free electro-enzymatic sensing methodology, which is advantageous over conventional mediator-based enzymatic sensing approaches that are prone to ionic interference

[36]. Furthermore, to construct the underlying sensing surface of the APAP TH-sensor (Fig. 2.4G), we utilized a surface engineering technique that allows for creating an “undistorted potential window” within which the target analyte’s voltammetric response becomes dominant and interference is eliminated.

The constructed ethanol sensor is comprised of: 1) an enzyme layer (alcohol oxidase, AOx) to catalyze the oxidation of ethanol and generate hydrogen peroxide (H_2O_2) as a detectable byproduct; 2) a permselective membrane (poly-*m*-phenylenediamine, PPD) to reject interfering electroactive species; and 3) an electroanalysis layer (platinum nanoparticle, PtNP) to detect the generated H_2O_2 . The constructed APAP sensor is based on: 1) a polymeric coating (Nafion) to mitigate the interference of the electroactive species and enhance the biofouling resistance and 2) a voltammetric sensing electrode (hydrogen-terminated boron-doped diamond electrode, H-BDDE) to selectively detect the oxidation peak of APAP. The developed sensing surfaces were coupled with a thin hydrogel layer to form the envisioned TH-sensors, and further augmented with our custom-developed signal interpretation framework to contextualize their readings for on-body applications.

To characterize the TH-sensor’s response in relation to the envisioned touch-introduced analyte flux, we particularly exploited the ethanol sensor, which allows for tracking its response in real-time via amperometry. Accordingly, we interfaced the artificial fingertip with the ethanol TH-sensor and configured it to continuously deliver ethanol molecules at a set flux (here, $0.64 \text{ nmol/min/cm}^2$). Also, we utilized a commercial benchtop potentiostat to record the generated sensor response. As illustrated in Fig. 2.4H, after an initial current jump (corresponding to the formation of the microfluidic fingertip/hydrogel contact), the sensor presented increasingly current response levels with a constant slope (denoted as k). Since the sensor’s response is proportional to

C_H , aligned with our aforescribed theoretical analysis, the observed slope is leveraged to represent the introduced analyte flux J .

Relevant to the envisioned touch-based sensing context, the same artificial fingertip characterization setup was utilized to investigate the potential confounding influence of variability in the strength of the pressing force. Accordingly, as the sensor response was being recorded continuously, different weights were mounted onto the artificial fingertip to mimic different strengths of pressing (corresponding to the normal pressure range exerted by finger pressing [40]). As shown in Fig. 2.4I, while initially a current jump was observed when making a contact between the weight-mounted artificial fingertip and the TH-sensor, mounting additional weights did not significantly alter the sensor response. In particular, zero slope was consistently measured in the absence of analyte flux (i.e., using a blank buffer solution as fluid input) and a relatively unchanged finite slope was observed for the case of non-zero analyte flux.

Furthermore, the artificial fingertip was utilized to systematically validate the TH-sensor's ability to track the analyte flux for varying introduced analyte concentration and flow rate conditions. In our context, given the exogenous nature of the target analytes, the relative variations in analyte concentration (during the course of analyte circulation) is more significant than the relative changes in the natural perspiration rate (which in stationary settings is relatively stable [41]). Therefore, for this study, we primarily focused on modulating the analyte concentration, while fixing the input flow rate within the physiologically-relevant range.

Figure 2.6A shows the real-time amperometric readouts of the ethanol TH-sensor, where the observed slopes linearly scale with the input concentrations (concentration range: 0-10 mM, flow rate: 320 nL/min/cm²). Figure 2.6B illustrates the corresponding calibration curve constructed based on the measured slopes ($R^2 = 0.99$). To characterize the APAP TH-sensor, we captured the

sensor's voltammograms (3 min after the sample introduction) for the APAP concentrations ranging from 0 to 80 μM (introduced at the same aforementioned flow rate, Fig. 2.6C). For each case, the voltammetric peak height (serving as the voltammetric signal) was extracted by applying our previously reported analytical framework and correcting for the effect of baseline variation [42]. Figure 2.6D shows the highly linear relationship between the input APAP concentration and the extracted signal ($R^2 = 0.99$). The characterizations of the two TH-sensors were further extended (using the same setup), by modulating the input flow rate (mimicking the natural perspiration rate variations), while keeping the respective analyte concentration constant. As shown in Fig. 2.7, for both cases, linear relationships between the measured signals and the corresponding input flow rates were observed.

2.7 Conclusions

In conclusion, a thin hydrogel was devised for simultaneous natural perspiration collection and in-situ electrochemical analysis. A first-order fluidic model was used to describe the enhanced analyte collection capability of the hydrogel, a property which was verified through caffeine and lactate sampling. Informed by the biomarker sampling characterization results across different body locations, the fingertip was determined as the optimal site for natural perspiration sampling, which was subsequently used to demonstrate the successful tracking of the dosage level and metabolic pattern of the caffeine intake among different subjects.

Furthermore, the developed TH was coupled with electrochemical sensors (forming TH-sensors) for non-invasively and inconspicuously analyte analysis. We developed a signal interpretation framework, which was formulated and supported with the aid of an introduced analyte transport model and an artificial fingertip characterization setup, allowed for extracting the

epidermal analyte partitioning flux information, decoupling the confounding effect of the pressing force variability, and correlating the epidermal readings to the corresponding analyte circulating levels. Expanding the detection capabilities of TH-sensing, we demonstrated a voltammetric TH-sensing method, which is particularly useful for measuring electroactive species such as pharmaceuticals and central to the translation of the CB-HMI into broader biomedical applications (as illustrated here in the context of medication adherence monitoring).

Collectively, the devised TH-sensing technique bypasses the fundamental challenge of circulating analyte accessibility (posed by the skin's barrier function), enabling the perception of body's chemistry at molecular levels.

2.8. Reference

1. Byrne, R.; Diamond, D., *Nat. Mater.* 2006, 5, 421-424.
2. Lin, H.; Zhao, Y.; Lin, S.; Wang, B.; Yeung, C.; Cheng, X.; Wang, Z.; Cai, T.; Yu, W.; King, K.; Tan, J.; Salahi, K.; Hojaiji, H.; Emaminejad, S. *Lab Chip* 19, 2844-2853, 2019.
3. Lin, H.; Hojaiji, H.; Lin, S.; Yeung, C.; Zhao, Y.; Wang, B.; Malige, M.; Wang, Y.; King, K.; Yu, W.; Tan, J.; Wang, Z.; Cheng, X.; Emaminejad, S., *Lab Chip* 2019, 19, 2966-2972, 2019.
4. Heikenfeld, J.; Jajack, A.; Rogers, J.; Gutruf, P.; Tian, L.; Pan, T.; Li, R.; Khine, M.; Kim, J.; Wang, J. *Lab Chip* 2018, 18, 217-248.
5. Lee, H.; Choi, T. K.; Lee, Y. B.; Cho, H. R.; Ghaffari, R.; Wang, L.; Choi, H. J.; Chung, T. D.; Lu, N. S.; Hyeon, T.; Choi, S. H.; Kim, D. H. *Nat. Nanotechnol.* 2016, 11, 566-572.
6. Koh, A.; Kang, D.; Xue, Y.; Lee, S.; Pielak, R. M.; Kim, J.; Hwang, T.; Min, S.; Banks, A.; Bastien, P.; Manco, M. C.; Wang, L.; Ammann, K. R.; Jang, K. I.; Won, P.; Han, S.; Ghaffari, R.;

- Paik, U.; Slepian, M. J.; Balooch, G.; Huang, Y. G.; Rogers, J. A. *Sci. Transl. Med.* 2016, 8, 366ra165.
7. Bariya, M.; Nyein, H. Y. Y.; Javey, A. *Nat. Electron.* 2018, 1, 160-171.
8. Heikenfeld, J. *Electroanal.* 2016, 28, 1242-1249.
9. Martin, A.; Kim, J.; Kurniawan, J. F.; Sempionatto, J. R.; Moreto, J. R.; Tang, G. D.; Campbell, A. S.; Shin, A.; Lee, M. Y.; Liu, X. F.; Wang, J. *ACS Sens.* 2017, 2, 1860-1868.
10. Gao, W.; Emaminejad, S.; Nyein, H. Y. Y.; Challa, S.; Chen, K. V.; Peck, A.; Fahad, H. M.; Ota, H.; Shiraki, H.; Kiriya, D.; Lien, D. H.; Brooks, G. A.; Davis, R. W.; Javey, A. *Nature* 2016, 529, 509-514.
11. Zhang, Y.; Guo, H. X.; Kim, S. B.; Wu, Y. X.; Ostojich, D.; Park, S. H.; Wang, X. J.; Weng, Z. Y.; Li, R.; Bandodkar, A. J.; Sekine, Y.; Choi, J.; Xu, S.; Quaggin, S.; Ghaffari, R.; Rogers, J. A. *Lab Chip* 2019, 19, 1545-1555.
12. Simmer, P.; Li, S. K.; Kasting, G.; Heikenfeld, J. *J. Dermatol. Sci.* 2018, 89, 40-51.
13. Emaminejad, S.; Gao, W.; Wu, E.; Davies, Z. A.; Nyein, H. Y. Y.; Challa, S.; Ryan, S. P.; Fahad, H. M.; Chen, K.; Shahpar, Z.; Talebi, S.; Milla, C.; Javey, A.; Davis, R. W. *Proc. Natl. Acad. Sci.* 2017, 114, 4625-4630.
14. Kim, J.; Campbell, A. S.; de Avila, B. E. F.; Wang, J. *Nat. Biotechnol.* 2019, 37, 389-406.
15. Jajack, A.; Brothers, M.; Kasting, G.; Heikenfeld, J. *Plos One* 2018, 13, e0200009.
16. Sonner, Z.; Wilder, E.; Heikenfeld, J.; Kasting, G.; Beyette, F.; Swaile, D.; Sherman, F.; Joyce, J.; Hagen, J.; Kelley-Loughnane, N.; Naik, R. *Biomicrofluidics* 2015, 9, 031301.
17. Leggett, R.; Lee-Smith, E. E.; Jickells, S. M.; Russell, D. A. *Angew. Chem. Int. Edit.* 2007, 46, 4100-4103.
18. Hazarika, P.; Russell, D. A. *Angew. Chem. Int. Edit.* 2012, 51, 3524-3531.

19. Burns, M.; Baselt, R. C. *J. Anal. Toxicol.* 1995, 19, 41-48.
20. Dolan, K.; Rouen, D.; Kimber, J. *Drug Alcohol Rev.* 2004, 23, 213-217.
21. Dutkiewicz, E. P.; Lin, J. D.; Tseng, T. W.; Wang, Y. S.; Urban, P. L. *Anal. Chem.* 2014, 86, 2337-2344.
22. Dutkiewicz, E. P.; Chiu, H. Y.; Urban, P. L. *J. Mass. Spectrom.* 2015, 50, 1321-1325.
23. Kuwayama, K.; Tsujikawa, K.; Miyaguchi, H.; Kanamori, T.; Iwata, Y. T.; Inoue, H. *Anal. Bioanal. Chem.* 2013, 405, 3945-3952.
24. Schmidt, B.; Roberts, R. S.; Davis, P.; Doyle, L. W.; Barrington, K. J.; Ohlsson, A.; Solimano, A.; Tin, W. *New Engl. J. Med.* 2006, 354, 2112-2121.
25. Dobson, N. R.; Liu, X. X.; Rhein, L. M.; Darnall, R. A.; Corwin, M. J.; McEntire, B. L.; Ward, R. M.; James, L. P.; Sherwin, C. M. T.; Heeren, T. C.; Hunt, C. E. *Brit. J. Clin. Pharmacol.* 2016, 82, 754-761.
26. Derbyshire, P. J.; Barr, H.; Davis, F.; Higson, S. P. J. *J. Physiol. Sci.* 2012, 62, 429-440.
27. Jia, W. Z.; Bandodkar, A. J.; Valdes-Ramirez, G.; Windmiller, J. R.; Yang, Z. J.; Ramirez, J.; Chan, G.; Wang, J. *Anal. Chem.* 2013, 85, 6553-6560.
28. Khodagholy, D.; Curto, V. F.; Fraser, K. J.; Gurfinkel, M.; Byrne, R.; Diamond, D.; Malliaras, G. G.; Benito-Lopez, F.; Owens, R. M. *J. Mater. Chem.* 2012, 22, 4440-4443.
29. J.-M. Moon, et al., *Angew. Chem. Int. Ed.* 60, 19074–19078, 2021.
30. J. R. Sempionatto, J.-M. Moon, J. Wang, *ACS Sens.* 6, 1875–1883, 2021.
31. World Health Organization, ProQuest (Firm), Global status report on road safety 2018 (World Health Organization, 2018).
32. A. M. Larson, et al., *Hepatology* 42, 1364–1372, 2005.

33. Ohshima, Y.; Shimizu, H.; Yanagishita, T.; Watanabe, D.; Tamada, Y.; Sugeno, J.; Tsuda, T.; Matsumoto, Y. *Arch. Dermatol. Res.* 2008, 300, 595-600.
34. L. Hou, et al., *Lab Chip* 13, 1868–1875, 2013.
35. B. A. Westrin, A. Axelsson. *Biotechnol. Tech.* 5, 303–306, 1991.
36. A. Hauke, et al., *Lab Chip* 18, 3750–3759, 2018.
37. L. Hou, et al., *Lab Chip* 13, 1868–1875, 2013.
38. M. J. Patterson, S. D. R. Galloway, M. A. Nimmo, *Exp. Physiol.* 85, 869–875, 2000.
39. S. R. Tripathi, E. Miyata, P. B. Ishai, K. Kawase, *Sci. Rep.* 5, 9071, 2015.
40. M. Ayyildiz, M. Scaraggi, O. Sirin, C. Basdogan, B. N. J. Persson, *Proc. Natl. Acad. Sci. U.S.A.* 115, 12668–12673, 2018.
41. U. Jacobi, J. Bartoll, W. Sterry, J. Lademann, *Arch. Dermatol. Res.* 296, 332–338, 2005.
42. S. Lin, et al. *Proc. Natl. Acad. Sci. U.S.A.* 117, 19017–19025, 2020.

Chapter 3. A touch-based multi-modal and cryptographic bio-human-machine interface

3.1. Introduction

Human machine interfaces (HMIs)—with built-in data acquisition, processing capabilities and data security measures—are necessary for acquiring awareness of the individuals’ status and assisting them with achieving optimal outcomes. Accordingly, various classes of HMIs have been developed and integrated within the ubiquitous electronics ecosystem to capture user-specific inputs through various channels, including touch [1], voice [2], and gesture [3, 4]. Such HMI modalities have laid the foundation for emerging technologies such as robotics [5], smart home [6], autonomous driving [7], and augmented reality [8], which are already transforming our current ways of living.

However, these HMIs provide limited awareness of the individuals’ biological status, which in turn prohibits their utility to unlock broader applications such as those in the healthcare domain [9]. This limitation is because of their intrinsic shortcomings in collectively accessing informative biochemical and biophysical indices—in other words, they lack “biological perception”. Toward devising a suitable HMI modality that bypasses such shortcomings, a key point of consideration is that biochemical indices (e.g., circulating biomarker molecules) are not trivially accessible due to the natural skin barrier function [10]—in contrast to putative biophysical indices (e.g., heart rate), which can be accessed inconspicuously using existing HMI-compatible sensors (e.g., optical devices). Also relevant to the context at hand, given the personal and sensitive nature of the target indices, any devised bio-centered HMI modality should account for user identification and data protection (e.g., encryption) [11, 12].

To this end, fingertips could serve as ideal human body sites for engineering the envisioned HMI for numerous reasons. Firstly, many of the circulating biomarker molecules partition onto the skin surface of the fingertip (primarily via natural perspiration) with a relatively high flux [13-17]. Leveraging this phenomenon, we previously introduced a thin hydrogel-based sensing modality to noninvasively acquire such biochemical indices at the point of fingertip [18]. The inconspicuous nature of this sampling method allows for bypassing the challenges associated with conventional biomarker sampling modalities, which are invasive (e.g., fingerstick blood sampling), require external stimulation (e.g., iontophoretic sweat or interstitial fluid sampling [19-21]), and/or deviate from individuals' routine behavior (e.g., drooling for saliva collection). Secondly, clinically significant biophysical indices such as heart rate (HR) and oxygen saturation level (SpO₂) can be simultaneously acquired from fingertips using standard non-invasive methods (e.g., photoplethysmography). Thirdly, the fingertip's unique biometric feature (i.e., fingerprint) can be leveraged for user identification and as a personalized cryptographic key for in-situ data encryption [22]. And fourthly, fingertip-based interactions are already the primary mode of communication in the readily proliferated HMIs (e.g., touch-sensitive screens, console controllers, trackpads, and keyboards).

Accordingly, here, we devised a touch-based cryptographic bio-HMI (namely, CB-HMI, Fig. 3.1A), which simultaneously acquires user's biochemical, biophysical, and biometric indices (as bio-inputs, Fig. 3.1B) using dedicated multi-modal data acquisition and processing modules. The data acquisition module consists of: 1) a thin hydrogel-coated electrochemical sensor (hereinafter, referred to as TH-sensor) to measure target biomarker molecule flux onto the skin (characterized and validated by a mass-transport simulation model and a microfluidic artificial fingertip); 2) a photoplethysmography (PPG) sensor to track HR and SpO₂ level; 3) a fingerprint

scanner to obtain the minutiae pattern (as a biometric index); and 4) the associated front-end circuitry for signal conditioning. The data processing module features inference algorithms to contextualize the readouts for decision making and user identification, as well as a biometric encryption algorithm to create a personalized key based on the imaged minutiae pattern for data encryption. In this way, the devised CB-HMI can render bio-perception and interpretation functionalities. Harnessing these functionalities, the CB-HMI can be augmented with other entities to determine and deliver the appropriate course of action (feedback, Fig. 3.1C). Example entities include robotic systems to facilitate intelligent machine operations (via mechanical/visual stimuli) and cloud servers (for data storage).

To illustrate the utility of the devised CB-HMI, we demonstrated its application within two representative scenarios toward improving the individuals' quality of life: driving safety and medication use. To acquire the biochemical index relevant to each of the scenarios, we developed and employed specialized TH-sensors. Specifically, we devised an enzymatic TH-sensor to target ethanol for the determination of alcohol intake and a voltammetric TH-sensor to target acetaminophen (APAP) as a model medication (a widely used analgesic and antipyretic). By incorporating our TH-sensors in human subject validation studies, we demonstrated the physiological significance of the acquired biochemical indices (on fingertip)—specifically, the correlation of the readings to the target molecules' circulating levels.

For the driving safety scenario, we integrated the CB-HMI within an in-vehicle interactive system, which is capable of bio-authenticating the drivers (on the basis of the driver's biometric match and alcohol-free state) for vehicle activation, as well as alerting the driver to potential drowsiness. For the medication use scenario, we integrated the CB-HMI within a custom-developed pill case to realize an unprecedented crypto-smart medication dispensing robotic

system. This system uniquely bio-authenticates the user prior to supplying the medication, verifies the medication intake (both based on the biometric match and the detected drug-level), and logs the biometrically-encrypted record of the events and bio-inputs on a cloud-connected server.

These demonstrated applications illustrate the CB-HMI's capability in upgrading the surrounding objects to attain biological perception. The ubiquitous proliferation of the CB-HMI, together with other classes of intelligent HMIs, will ultimately create smart surroundings equipped with comprehensive and deep awareness of the individuals' psychophysiological state and needs (Fig. 3.1D).

3.2. Experimental Section

3.2.1. TH-sensor fabrication and in-situ characterizations

TH-sensors targeting ethanol and APAP were fabricated following the method described in Chapter 2. To characterize these TH-sensors in-situ, two human subjects participated in the characterization of each type of TH-sensor. For each trial, the subjects were instructed to wash their index fingertips with deionized (DI) water before testing and to rinse their mouth with cold water immediately after the beverage/medication intake (to avoid contamination from residue). Touch-based measurements were performed using corresponding TH-sensors before and at intermittent time points after the beverage/medication intake. The water loss from the fingertip was monitored by an evaporimeter (VapoMeter, Delfin Technologies). The fingertip temperature was monitored by a thermocouple (HT-9815, RISEPRO). For ethanol measurement, the amperometric current was linearly-fitted (for the duration of measurement of 10-30 s, after finger pressing) and the derived current slope was considered as the sensor signal. BAC was estimated using an alcohol breathalyzer (S80, BACtrack Inc.). The subject was provided with ~ 100 mL

alcoholic beverages (12.5%, from the local market). For APAP measurement, a DPV scan was performed 3 min after finger pressing, and the acquired readout was analyzed using the same analytical framework as the ex-situ study. Saliva samples were collected by direct salivation with the aid of the Saliva Collection Aid (Salimetrics) and analyzed using the liquid chromatography with tandem mass spectrometry following our previous established protocol (31). The experiments were performed in accordance with the subjects' originally-scheduled medication intake (Regular Strength Pain Relief, CVS Health, containing 650 mg APAP in total).

3.2.2. PPG signal acquisition and processing

The PPG sensing interface was constructed using an integrated PPG-based sensor module (MAX30101, Maxim Integrated Inc.) with a sampling rate of 80 Hz. The sensor module consists of a red and an IR light-emitting diode (red: 660 nm, IR: 880 nm), as well as a photodiode to detect the tissue-reflected light. A standard pulse oximeter (Zacurate Pro Series 500DL) was utilized to validate the sensor readout. The pulse oximeter was placed on a different fingertip of the subject's same hand. Continuous HR and SpO₂ readings from the standard pulse oximeter were video-recorded and compared with the readouts from the developed sensing interface. The PPG readout of the sensing interface was processed using MATLAB. Accordingly, upon signal smoothing, the peaks and troughs for both wavelengths were extracted using a local minima-maxima finding algorithm.

The HR was extracted by calculating the time interval between consecutive systolic peaks (average of 6 consecutive peaks). To derive the SpO₂ level, the non-pulsatile DC component and the pulsatile AC component for both wavelengths were extracted (DC_{red} , DC_{IR} , AC_{red} , AC_{IR}). For each peak-trough pair, the trough level was used as the DC component and the difference between

the peak and trough levels was used as the AC component. Then, the ratio of the normalized red and IR readings ($R_{red/IR}$) for each peak-trough peak was determined as

$$R_{red/IR} = \frac{AC_{red}/DC_{red}}{AC_{IR}/DC_{IR}}$$

The SpO₂ levels were estimated following a previously reported simplified linear calibration approach [23], where the measurements by the standard pulse oximeter served as reference.

3.2.3. Fingerprint acquisition and user identification

The fingerprint sensing interface was constructed using a capacitive fingerprint scanner (AS-108M, Sparkfun). The acquired fingerprint image was processed using MATLAB following a previously reported algorithm [24, 25]. Briefly, for both query and template fingerprints, upon performing a feature enhancement step, the friction ridges were identified, and the minutiae pattern was extracted and outputted as a list of minutiae features. To assess the degree of similarity, different permutations of one-to-one pairing between the query and template minutiae features were constructed. To account for the slight differences in fingerprint input angle, the rotated versions of the minutiae patterns were also constructed (relatively rotated within 5°) and compared. For each pairing permutation, the paired minutiae features were compared individually: two minutiae were defined as a match if their relative distance and ridge direction difference were both below defined thresholds (threshold distance: 15 pixels, threshold direction difference: 14°). The degree of similarity (s) was determined by considering the permutation that produced the maximum number of matched pairs (following the definition presented in the Results section). The query fingerprint was determined to match the template if the calculated s was greater than the defined threshold of 50%.

3.2.4. CBS Construction

The fingerprint-based CBS follows a previously reported fuzzy vault scheme (implemented in MATLAB) [26]. For data encryption, a sequence of integers was formed (secret) by appending the TH-sensor, HR, and SpO₂ readouts (each 3 digits long), together with a single-digit indicative of the feedback status (0: medication supply request rejected; 1: medication supply request granted; 2: medication intake pending; and 3: medication intake verified). A 3-bit cyclic redundancy check (CRC-3) was calculated based on the secret (with the aid of the standard CRC-3 generating polynomial), and the equivalent decimal value was derived and prepended to the secret. Similarly, an error-prevention digit (“0”) was appended to the secret to mitigate the influence of fitting error in the subsequent decryption process. The modified secret was then divided into four segments, each serving as a coefficient in a third-degree polynomial $f(x)$ expression. The 10-digit biometric key $\{x_i\}$ ($i = 1$ to 10) was generated using the minutiae pattern of the template fingerprint by calculating the relative distance of the extracted minutiae features with respect to a given extracted feature as a reference. Then the generated key was projected onto the polynomial to create a set of genuine points $\{(x_i, f(x_i))\}$. With the aid of a random number generator, a set of chaff points was created as $\{(a_j, b_j)\}$ ($j = 1$ to 40), where $a_j \neq x_i$ ($i = 1$ to 10) and $b_j \neq f(a_j)$. The vault $\{(u_k, v_k)\}$ ($k = 1$ to 50) was created by assembling and scrambling the genuine and chaff sets.

To decrypt the secret, a biometric key $\{y_i\}$ ($i = 1$ to 10) was first generated using the query fingerprint similar to the encryption procedure. Then $\{y_i\}$ was compared with the abscissa values of the vault $\{u_k\}$: if any y_i was equal to u_k , the corresponding (u_k, v_k) was identified as a genuine point candidate. The genuine point candidates were used to reconstruct the third-degree polynomial of best fit (with the aid of a polynomial fitting function). The original secret was then retrieved based on the coefficients of the reconstructed polynomial. For the entries where the

number of genuine point candidates were insufficient for polynomial fitting or that the CRC decoding failed, the decryption process was considered and labelled as a “Fail”. Otherwise, the retrieved secret was presented as the corresponding bio-input values to the user.

3.2.5. CB-HMI construction

The data acquisition module consists of two printed circuit boards (PCBs): a primary PCB to host the TH-sensor, the fingerprint scanner, and the PPG sensor, and a secondary PCB, which hosts the signal conditioning circuitry and a Bluetooth module (HM-11; Seeed Technology Co.). The TH-sensor was connected to the primary PCB with the aid of a flexible cable (Molex) and a double-sided adhesive anisotropic conductive film (9703; 3M). The secondary PCB was interfaced with a data processing module (implemented on Raspberry Pi 3 model B+, Raspberry Pi Foundation). To acquire the biochemical indices, the excitation potential waveform was applied to the corresponding TH-sensor with the aid of a 16-bit digital-to-analog converter (DAC, DAC8552, Texas Instruments). For ethanol sensing the excitation waveform was a constant voltage, and for APAP sensing the waveform followed a DPV format (following the same parameters as respective potentiostat measurements). The current response of the TH-sensors was converted into a digital voltage output with the aid of a transfer impedance amplifier (TIA) (LT1462; Linea Technology) and a 24-bit analog-to-digital converter (ADC) (ADS1256; Texas Instruments). The PPG sensor and the fingerprint scanner directly communicated with the Raspberry Pi through the inter-integrated circuit (I2C) protocol and the universal asynchronous receiver-transmitter (UART) interface, respectively. The MATLAB data processing codes (implementing the inference, bio-authentication, and encryption algorithms) were loaded on the Raspberry Pi. A single,

miniaturized, rechargeable lithium-ion polymer battery with a nominal voltage of 3.7 V was used to power the PCBs and the Raspberry Pi.

3.2.6. Construction of CB-HMI-enabled systems

For both in-vehicle and medication dispensing systems, the Raspberry Pi was connected to a 1.44-in color thin-film-transistor LCD screen (SF-TS144C-9082A-N; Shenzhen SAEF Technology) to provide visual feedback. The in-vehicle safety system was constructed by mounting the CB-HMI and the LCD screen onto a steering wheel (via a double-sided tape). The medication dispensing system was constructed by repurposing a motorized box (Useless Box, Calary). The front panel of the box was laser-patterned (Speedy 300, Trotec) to accommodate the CB-HMI and the LCD screen. The robotic arm movement was controlled by the Raspberry Pi with the aid of a motor driver (L298N; STMicroelectronics). The acquired and in-situ encrypted bio-inputs were communicated (via Bluetooth) to a user interface (e.g., a laptop), which in turn served as an intermediary terminal for data transmission to a cloud server (here, a custom-developed Google Cloud platform).

3.2.7. Human subject testing using the CB-HMI-enabled systems

For the in-vehicle system, the fingerprint of the vehicle owner was collected and stored in the Raspberry Pi as a template. For each entry, the subject was instructed (via LCD) to press the fingertip onto the CB-HMI until all the bio-inputs were acquired (~ 40 s). During this period, the ethanol (10-30 s post fingertip pressing), PPG, and fingerprint readouts were acquired sequentially. The raw readouts were transmitted to the Raspberry Pi for data processing. Bio-authentication was performed by comparing the processed data with the corresponding thresholds. The determined

alcohol state of the subject, the derived HR and SpO₂ information, and the concluded bio-authentication status were transmitted and displayed on the LCD screen. For the medication dispensing system, the fingerprint information was also collected and stored in the Raspberry Pi as a template. For each entry, the subject was instructed (via LCD) to press the fingertip onto the CB-HMI for ~ 30 s. During the fingertip pressing period, the fingerprint and the PPG readouts were acquired sequentially. The DPV scanning was performed afterwards (~ 30 s). All the raw readouts were transmitted to the Raspberry Pi for data processing, bio-authentication, and medication dispensing (if applicable). The interpreted bio-inputs and the feedback status were transmitted to and displayed on the LCD screen.

3.2.8. Institutional Review Board Approval for Human Subject Testing

The conducted human subject experiments were performed in compliance with the protocols that have been approved by the Institutional Review Board at the University of California, Los Angeles (IRB No. 17-000170). All subjects gave written informed consent before participation in the study.

3.3. In-situ characterization of the thin hydrogel-coated electrochemical sensors

To access biochemical indices, which are central to the realization of bio-perception, we engineered specialized TH-sensors. The fabrication and ex-situ characterization of ethanol and APAP TH-sensors are detailed in Chapter 2. Here, we first validated the core in-situ detection capability of the described TH-sensors (Fig. 3.2A-F). We specifically employed the ethanol TH-sensor to assess whether the sensor is capable of differentiating between two states: no alcohol-intake vs. recent intake of an alcoholic beverage. For this context, we defined the measured signal

S as the slope of the sensor's amperometric response, and the threshold as $S_{\text{free, avg}} + 3 \times S_{\text{free, SD}}$, where $S_{\text{free, avg}}$ and $S_{\text{free, SD}}$ are the average and standard deviation of the signals obtained from the alcohol-free subject (three trials). In our studies, the threshold for determining the alcohol-free state was measured as 0.36 nA/min. We then performed touch-based TH-sensor measurements before ($t = -20$ min) and after ($t = +60$ min) the intake of an alcoholic beverage (~ 100 mL, 12.5% alcohol). As shown in Fig. 3.2A,B, the ethanol TH-sensor was capable of differentiating the pre/post-intake events, as evident from the near-zero amperometric current slope for the pre-intake measurement and the relatively steep positive slope in the post-intake measurement ($S = 21.5$ nA/min).

We adopted a similar study framework to evaluate the in-situ detection capability of APAP TH-sensor. For this context, the measured signal is defined as the voltammetric current peak height (I_P), and the threshold for determining the APAP-free state was measured as 3.7 nA (three trials). Figure 3.2D,E show the corresponding voltammograms measured by the APAP TH-sensor, 10 min before and 60 min after the intake of an APAP-based medication (containing 650 mg APAP). The comparison of the two voltammograms and the corresponding extracted current peaks ($I_{P, \text{pre-intake}} \sim 0$ nA vs. $I_{P, \text{post-intake}} \sim 15$ nA) validates that the developed TH-sensor is capable of detecting the presence of circulating APAP molecules via the devised touch-based modality.

To further illustrate the physiological significance of the biochemical readings obtained from this modality, we extended our study framework to take fingertip-based measurements with a higher temporal resolution and compare the extracted profile with the target molecules' circulating levels. Accordingly, the fingertip-based measurements were performed before and at intermittent time points after the alcoholic beverage/medication intake. To track the molecules' circulating profile, standardized proxy measurements were performed: blood alcohol content

(BAC) was estimated using an alcohol breathalyzer and salivary APAP was analyzed with mass spectrometry following our previously reported method [27]. As shown in Figure 3.2C,F, the temporal profiles of target molecules captured by the TH-sensors closely mirror the molecules' circulating profiles. Similar trend was observed in a second subject following the same study framework (Fig. 3.3).

Furthermore, to verify that the observed trend of the analyte flux is due to the underlying changes in the analyte circulating levels but not the variations in perspiration rate, in a separate study the perspiration rate was monitored intermittently following the same framework and over the same time window. We specifically utilized a commercially available evaporimeter (Delfin VapoMeter) and a standard temperature probe to directly/indirectly measure the natural perspiration rate profile [28]. As shown in Fig. 3.4, all the measurements presented relatively stable profiles, indicating that the perspiration characteristic was relatively consistent in the context of our study.

3.4. Develop and integration of the multimodal data acquisition and processing modules

To render biophysical index acquisition and processing, we implemented a PPG-based sensing interface and the associated inference algorithms to derive the underlying physiological signals such as HR and SpO₂. Here, PPG was specifically selected, because of its established clinical utility in assessing the user's overall physiological status (e.g., cardiovascular health and respiration), and its non-invasive and touch-based nature (inline with our envisioned interaction modality) [29]. The PPG sensor consists of a red and an infrared (IR) light-emitting diode (with corresponding wavelengths of 660 nm and 880 nm), as well as a photodiode to detect the tissue-reflected light.

Figure 3.2G shows representative real-time sensor readouts of the red and IR channels acquired from the fingertip of a subject. To derive the HR information, the pulsing frequency of the measured photoplethysmogram is first extracted by applying a peak identification algorithm. To validate the accuracy of the acquired HR, the processed sensor readouts from five subjects were compared with their corresponding HR obtained by a standard pulse oximeter. As illustrated in Fig. 3.2H, the two measurement sets are closely matched (difference < 3 beats per minute, bpm). Moreover, the ratio of the normalized red and IR readings ($R_{\text{red/IR}}$) were used to derive the SpO₂ information. In order to calibrate the readouts and validate the utility of the sensing module in capturing the SpO₂ temporal profile, a breath holding experiment was performed to induce variations in SpO₂, following a previously reported protocol [30]. In this context, SpO₂ data was acquired continuously on two fingertips using the corresponding devised acquisition/processing modules and a standard oximeter. As shown in Fig. 3.2I, as acquired by both methods, the holding of the breath led to a significant SpO₂ drop, followed by a rapid increase back to the normal value. Collectively, the results illustrate the physiological significance of the acquired biochemical and biophysical indices. To seamlessly associate these bio-inputs to the user, while preserving the user's privacy, we developed a built-in user identification/data encryption scheme. This scheme capitalizes on the unique biometric feature of the fingerprint, which is inherently accessible in our envisioned HMI. Accordingly, we implemented a fingerprint scanner and developed dedicated image processing algorithms to identify the user and biometrically encrypt the data based on the scanned fingerprint (Fig. 3.2J). In our image processing approach, the unique minutiae pattern is extracted from the scanned fingerprint by applying feature enhancement and extraction algorithms (Fig. 3.2K). The extracted minutiae features are described by their x-coordinate, y-coordinate, and local ridge direction attributes [31]. To identify the query fingerprint, its minutiae features are

compared with those of the template fingerprint (Fig. 3.2L). In this context, their degree of similarity (s) can be described as:

$$s = \frac{\max_i \{n_{match}\}}{\sqrt{n_{query} \cdot n_{template}}} \times 100\%$$

, where n_{match} , n_{query} , and $n_{template}$ correspond to the number of matched-, query-, and template minutia, respectively for a given query-template minutiae pairing permutation i . Here, we define the threshold of 50% for s , as the criterion to determine that any two fingerprints are matched [32].

The collected biometric index is further utilized to realize a crypto-biometric system (CBS), which encrypts the secret (here, bio-inputs) using a biometric key generated from the minutiae pattern. To this end, here we adopted a fuzzy vault scheme (Fig. 3.2M) that is particularly suitable for the construction of fingerprint-based CBS as it can tolerate the fuzziness inherent to the biometric entries (i.e., input-to-input variations of the minutiae features for the same user) [33]. In short, the bio-inputs are encrypted in a vault using the minutiae-generated key A , which can be decrypted by query minutiae-generated key B only if B overlaps with A substantially (i.e., the two fingerprints are from the same individual). As shown in Fig. 3.5A, this encryption process involves: 1) transformation of the bio-inputs into the coefficients of a polynomial equation; 2) projection of the fingerprint minutiae (here, distances among minutiae) onto the polynomial equation to create genuine points; 3) generation of polynomial-offset chaff points; and 3) creation of the vault list using the scrambled genuine points and chaff points. Figure 3.5B illustrates the corresponding decryption process. This process involves identifying the genuine points using the query minutiae feature and polynomial fitting to extract the coefficients, followed by reconstructing the bio-inputs. Furthermore, Fig. 3.6 shows the application of the implemented CBS given a hypothetical input, illustrating that the input is successfully encrypted/decrypted.

3.5. Development and application of a CB-HMI-enabled in-vehicle safety system

The validated acquisition/processing modules for the bio-inputs of interest are integrated within an embedded system (Fig. 3.7, 3.8) to realize the envisioned multimodal CB-HMI. The multimodal CB-HMI can be augmented with other entities (e.g., robotic systems, cloud servers) to facilitate feedback and data storage.

To demonstrate its utility in a vehicle environment (integral part of our daily experience), we first integrated the CB-HMI on a steering wheel to form an in-vehicle interactive system towards improving driving safety (Fig. 3.9A,B). Enabled by the CB-HMI, the system can perceive the driver's ethanol level (using the ethanol TH-sensor), fingerprint, and PPG signal. These degrees of bio-perception can be leveraged to bio-authenticate the drivers (interpretation) for vehicle activation (feedback). For bio-authentication, the system utilizes the bio-input entries to verify the driver's alcohol-free state, biometric match, and liveness of the biometric input (to avoid tampering, by exploiting the PPG signal as a liveness indicator [34]). Also applicable to this example setting, the derived HR and SpO₂ information from the PPG measurements can serve as useful feedback to the driver, as they are informative measures of potential drowsiness [35]. As a proof-of-concept, here the authentication status, together with the acquired indices, are transmitted and displayed on a steering wheel-mounted LCD screen to provide visual feedback.

To demonstrate the bio-authentication function of the developed in-vehicle interactive system, the system was tested in three hypothetical scenarios. For each scenario, upon finger pressing, the ethanol readout, the PPG readout, and the fingerprint readout were acquired by the CB-HMI and the feedback information was communicated to the user via an LCD. Figure 3.9C-E shows the input status, the raw and interpreted bio-inputs (recorded and processed by the integrated modules), together with the generated feedback for each of the scenarios. In the first scenario (Fig.

3.9C), while the presence of alcohol in the subject's system was not detected ($k < 0.36$ nA/min), the activation request was rejected since the query fingerprint did not match the template of the vehicle owner ($s < 50\%$). In the second scenario (Fig. 3.9D), the activation request was rejected because of the detection of alcohol presence ($k > 0.36$ nA/min) in the driver's circulating system (despite verification of the owner's identity, $s > 50\%$). In the last scenario (Fig. 3.9E), biometric match and alcohol-free readouts were obtained ($k < 0.36$ nA/min, $s < 50\%$), and the liveness of the biometric entry was verified, leading to granting the vehicle activation request. For all these scenarios, the system acquired and interpreted the relevant bio-inputs successfully and identified and communicated the intended course of action correctly.

3.6. Development and application of a CB-HMI-enabled medication dispensing robotic system

To demonstrate the versatility of the CB-HMI and its enabling application, we illustrated its utility for assisting the user(s) with their pharmacotherapy regimen. Accordingly, we integrated the CB-HMI into a custom-developed pill case to realize an unprecedented crypto/smart medication dispensing robotic system (Fig. 3.10A,B). This system perceives the users' bio-indices, including medication level (here APAP, using the APAP TH-sensor), fingerprint, HR, and SpO₂ to bio-authenticate the user (for medication dispensing), verify the medication intake, and update the personal electronic health records.

Specifically, for bio-authentication, the system exploits the bio-inputs to verify the user's identity and no/low medication circulating level as prerequisites for supplying the requested medication. Upon verification, the system dispenses the requested pill with the aid of a robotic arm (mechanical feedback). Similarly, by prompting the user to provide a follow-up touch-based entry,

the same bio-inputs can be used to confirm the medication intake (by verifying the elevated circulating level of the medication in tandem with the user's identity). For both situations, the status of the bio-authentication/intake verification, as well as the acquired bio-indices are displayed on a pill case-mounted LCD screen to provide real-time visual feedback to the user. Optionally, this information can be biometrically-encrypted and logged on a cloud-connected server. In this way, the personal electronic health record of the user can be seamlessly updated, while preserving the security of the collected information—all at the point of touch.

Figure 3.10C,D demonstrate the bio-authentication function of the developed system for two representative cases: one with a subject with no recent APAP intake (> 24 h), the other with the same subject, but with a recent APAP intake (~ 1 h). In the first case, the medication request was rejected because of the detection of APAP presence at a relatively high level ($I_p > 3.7$ nA, Fig. 3.10C). In the second case, because no-/minimal circulating drug was detected ($I_p < 3.7$ nA, Fig. 3.10D), the medication request was granted, triggering the automatic delivery of a single pill by a robotic arm.

To demonstrate all the enabling functionalities of the developed system, it was applied to assist a user under a regular APAP dosing schedule (650 mg every 6 hours). In this illustrative study, three entries were provided by the user at predetermined time points ($t = 0, +5,$ and $+6$ h), where the user had a recent intake (at $t = -1$ h), which was unbeknownst to the system. Figure 3.10E shows the derived status for each entry in relation to the acquired bio-inputs (detailed in Fig. 3.11): a rejected medication request due to the detection of the presence of relatively high level of APAP (in agreement with the user's APAP intake history); a granted medication request followed by automatic pill delivery ($t = +5$ h); and a successful intake verification ($t = +6$ h). For each entry, the acquired bio-inputs were biometrically-encrypted in-situ (using our embedded CBS) and

transmitted to a Google cloud server for storage. The description of the encryption process for a representative entry ($t = +5$ h) is shown in Fig. 3.10F. At the end of the day, upon the user's request—simply through a fingertip entry—all the stored encrypted electronic medical records were successfully retrieved and decrypted to render the longitudinal profile of the acquired bio-indices.

3.7. Discussion

We devised an HMI modality—with built-in cryptographic multimodal bio-perception and interpretation capabilities—that translates the user's touch-based entries into encrypted biochemical, biophysical, and biometric indices.

As its central component, our HMI (termed CB-HMI) features a TH-coated sensing interface to non-invasively and inconspicuously measure biochemical indices. The employed TH-sensing methodology bypasses the fundamental challenge of circulating analyte accessibility (posed by the skin's barrier function), enabling the perception of body's chemistry at molecular levels. We specifically developed TH-sensors and defined signal terms to track the on-skin flux of circulating ethanol and APAP molecules.

Expanding the scope of the biological perception, the CB-HMI additionally features physical sensors (PPG and fingerprint scanner) to acquire the user's biophysical (HR, SpO₂) and biometric (fingerprint minutiae pattern) indices. Upon integrating the associated data acquisition and processing modules, we validated the CB-HMI's complete bio-perception/interpretation functionality via human subject studies. Collectively, the results demonstrated the CB-HMI's capabilities in terms of acquiring physiologically-relevant readouts of target bio-indices, as well as user-identifying and biometrically-encrypting these indices in-situ.

Furthermore, by upgrading the common surrounding objects with the CB-HMI, and subsequently, equipping them with biological perception/interpretation, we created new interactive solutions to promote the user's quality of life. The demonstrated interactive system for vehicle activation, which is capable of detecting the circulating alcohol level at well below the legal limit for driving [36], could be particularly helpful in preventing DUI—one of our modern societal challenges claiming > 10,000 lives each year in the United States alone [37]. The demonstrated crypto-smart medication dispensing robotic system could serve as an ideal drug adherence monitoring solution, owing to its built-in user bio-authentication, medication intake verification, and seamless electronic medical record keeping capabilities [38]. The demonstrated biochemical sensing capabilities can be extended to target other medications and substances and augmented with advanced algorithms to determine appropriate drug dosing and cut-off values. The acquired insight can be further enriched and contextualized by incorporating a dedicated interface for logging user reported symptoms. Moreover, the feedback functionality could also be extended to alert the subject of dose due/overdue. In this way, our technology can be positioned to address one of our societal grand healthcare challenges: non-optimized medication therapy, which is fueled by inappropriate dosing and patients' poor medication adherence, and results in 275,000 deaths and \$530B in healthcare costs, annually [39].

Toward providing a comprehensive bio-perception of the user, the devised HMI can be adapted to acquire a wider panel of psychological and physiological indices. For example, the presented TH-based sensing methodology can be applied to target endogenous molecular indicators of health, including hormones, nutrients, metabolites, and cytokines. To interpret these measurements and to inform actionable feedback, the influence of various confounding factors (e.g., skin and gland metabolism, perspiration rate variation) needs to be carefully characterized

(via large-scale clinical studies), and if necessary mitigated (via engineering solutions and machine learning algorithms). To this end, the incorporation of auxiliary sensors (e.g., temperature, humidity) could be helpful to standardize the measurements and to account for underlying sources of inter-/intra-individual variability. Furthermore, the presented PPG-based sensing modality can be extended to derive other informative biophysical indices such as respiratory rate and blood pressure.

The unique built-in data encryption feature of our devised HMI inherently provides the layer of security necessary to protect such wealth of personal information, while enabling decentralized bio-data collection and processing within Internet of Things and blockchain infrastructures. To this end, dedicated CBS optimization/validation efforts are required to improve the biometric encryption algorithm's reliability (e.g., via development of advanced key generation algorithms and validation with standard databases).

Ultimately, the maturity and proliferation of the CB-HMI, together with other classes of intelligent HMIs, will equip our surroundings with a comprehensive and deep awareness of the individuals' psychophysiological state and needs. This advancement will seed the foundation for creating interactive and adaptive environments to actively assist the users in reaching their optimal outcomes efficiently.

3.8. Reference

1. P. Bach-y-Rita, S. W. Kercel, *Trends Cogn. Sci.* 7, 541–546, 2003.
2. CC. Philip R., S. L. Oviatt, *Proc. Natl. Acad. Sci. U.S.A.* 92, 9921–9927, 1995.
3. Heikenfeld S. S. Rautaray, A. Agrawal, *Artif. Intell. Rev.* 43, 1–54, 2015.

4. Z. Zhou, K. Chen, X. Li, S. Zhang, Y. Wu, Y. Zhou, K. Meng, C. Sun, Q. He, W. Fan, E. Fan, Z. Lin, X. Tan, W. Deng, J. Yang, J. Chen, *Nat. Electron.* 3, 571–578, 2020.
5. S. DiMaio, M. Hanuschik, U. Kreaden, J. Rosen, B. Hannaford, R. M. Satava, Eds. (Springer, Boston, MA, 2011), 199–217.
6. L. Jiang, D.-Y. Liu, B. Yang, *Proceedings of 2004 International Conference on Machine Learning and Cybernetics* 2, 659–663, 2004.
7. K. Bengler, M. Rettenmaier, N. Fritz, A. Feierle, *Information.* 11, 61, 2020.
8. X. Yu, Z. Xie, Y. Yu, J. Lee, A. Vazquez-Guardado, H. Luan, J. Ruban, X. Ning, A. Akhtar, D. Li, B. Ji, Y. Liu, R. Sun, J. Cao, Q. Huo, Y. Zhong, C. Lee, S. Kim, P. Gutruf, C. Zhang, Y. Xue, Q. Guo, A. Chempakasseril, P. Tian, W. Lu, J. Jeong, Y. Yu, J. Cornman, C. Tan, B. Kim, K. Lee, X. Feng, Y. Huang, J. A. Rogers, *Nature.* 575, 473–479, 2019.
9. M. Mayer, A. J. Baeumner, *Chem. Rev.* 119, 7996–8027, 2019.
10. J. Heikenfeld, A. Jajack, B. Feldman, S. W. Granger, S. Gaitonde, G. Begtrup, B. A. Katchman, *Nat. Biotechnol.* 37, 407–419, 2019.
11. A. D. Thierer, “The internet of things and wearable technology: addressing privacy and security concerns without derailing innovation” (SSRN Scholarly Paper ID 2494382, Social Science Research Network, Rochester, NY, 2015).
12. W. Wilkowska, M. Ziefle, *Health Inform. J.* 18, 191–201, 2012.
13. P. P. Samant, M. M. Niedzwiecki, N. Raviele, V. Tran, J. Mena-Lapaix, D. I. Walker, E. I. Felner, D. P. Jones, G. W. Miller, M. R. Prausnitz, *Sci. Transl. Med.* 12, 2020.
14. H. Y. Y. Nyein, M. Bariya, B. Tran, C. H. Ahn, B. J. Brown, W. Ji, N. Davis, A. Javey, *Nat. Commun.* 12, 1823, 2021.
15. K. C. O’Neill, P. Hinnners, Y. Jin Lee, *Anal. Methods.* 12, 792–798, 2020.

16. W. Tang, L. Yin, J. R. Sempionatto, J.-M. Moon, H. Teymourian, J. Wang, *Adv. Mater.* 33, 2008465, 2021.
17. J. Brunmair, A. Bileck, T. Stimpfl, F. Raible, G. Del Favero, S. M. Meier-Menches, C. Gerner, *EPMA Journal.* 12, 141–153, 2021.
18. S. Lin, B. Wang, Y. Zhao, R. Shih, X. Cheng, W. Yu, H. Hojaiji, H. Lin, C. Hoffman, D. Ly, J. Tan, Y. Chen, D. Di Carlo, C. Milla, S. Emaminejad, *ACS Sens.* 5, 265-273, 2020.
19. S. Emaminejad, W. Gao, E. Wu, Z. A. Davies, H. Yin Yin Nyein, S. Challa, S. P. Ryan, H. M. Fahad, K. Chen, Z. Shahpar, S. Talebi, C. Milla, A. Javey, R. W. Davis, *Proc. Natl. Acad. Sci. U.S.A.* 114, 4625–4630, 2017.
20. S. Mitragotri, M. Coleman, J. Kost, R. Langer, *J. Appl. Physiol.* 89, 961–966, 2000.
21. H. Lin, J. Tan, J. Zhu, S. Lin, Y. Zhao, W. Yu, H. Hojaiji, B. Wang, S. Yang, X. Cheng, Z. Wang, E. Tang, C. Yeung, S. Emaminejad, *Nat. Commun.* 11, 4405, 2020.
22. D. Maltoni, D. Maio, A. K. Jain, S. Prabhakar, *Handbook of fingerprint recognition*, Springer, 2009.
23. T. Tamura, *Biomed. Eng. Lett.* 9, 21–36, 2019.
24. A. K. Jain, J. Feng, K. Nandakumar, *Computer.* 43, 36–44, 2010.
25. V. K. Alilou, Simple fingerprint matching (2020; <https://github.com/alilou63/fingerprint>).
26. J. Wooger, Fuzzy vault (2021; https://github.com/jwooger/fuzzy_vault).
27. S. Lin, W. Yu, B. Wang, Y. Zhao, K. En, J. Zhu, X. Cheng, C. Zhou, H. Lin, Z. Wang, H. Hojaiji, C. Yeung, C. Milla, R. W. Davis, S. Emaminejad, *Proc. Natl. Acad. Sci. U.S.A.* 117, 19017–19025, 2020.
28. J. E. Wingo, D. A. Low, D. M. Keller, R. M. Brothers, M. Shibasaki, C. G. Crandall, *J. Appl. Physiol.* 109, 1301–1306, 2010.

29. E. Mohamed, *Curr. Cardiol. Rev.* 8, 14–25, 2012.
30. W. G. Zijlstra, A. Buursma, W. P. Meeuwsen van der Roest, *Clin. Chem.* 37, 1633–1638, 1991.
31. A. K. Jain, J. Feng, K. Nandakumar, *Computer.* 43, 36–44, 2010.
32. T. Dunstone, N. Yager, Eds., *Biometric system and data analysis: design, evaluation, and data mining* (Springer, Boston, MA, 2009), 27–43.
33. U. Uludag, S. Pankanti, A. K. Jain, in *Audio- and Video-Based Biometric Person Authentication*, T. Kanade, A. Jain, N. K. Ratha, Eds. (Springer, Berlin, Heidelberg, 2005), Lecture Notes in Computer Science, 310–319.
34. E. M. Nowara, A. Sabharwal, A. Veeraraghavan, *12th IEEE International Conference on Automatic Face Gesture Recognition*, 56–62, 2017.
35. G.-S. Ryu, J. You, V. Kostianovskii, E.-B. Lee, Y. Kim, C. Park, Y.-Y. Noh, *IEEE Trans. Electron Devices.* 65, 2997–3004, 2018.
46. National Highway Traffic Safety Administration, “Digest of impaired driving and selected beverage control laws, thirtieth edition, current as of december 31, 2015” (DOT HS 812 394, U.S. Department of Transportation, Washington, DC., 2017).
37. National Highway Traffic Safety Administration, “Overview of the 2019 crash investigation sampling system” (DOT HS 813 038, U.S. Department of Transportation, Washington, DC., 2020), p. 5.
38. W. Y. Lam, P. Fresco, *Biomed Res. Int.* 2015, e217047, 2015.
39. J. H. Watanabe, T. McInnis, J. D. Hirsch, *Ann. Pharmacother.* 52, 829–837, 2018.

Chapter 4. Touch-based non-invasive lithium monitoring using an organohydrogel-based sensing interface

4.1. Introduction

Lithium salt is one of the most widely-used psychiatric medications for individuals with bipolar disorder. Despite its demonstrated efficacy for mood stabilization, translating its effectiveness into improved patient outcomes in clinical practice remains nontrivial due to multiple challenges. Firstly, lithium has a narrow therapeutic window ($\sim 0.6 - 1.2$ mM) with severe adverse effects if overdosed [1]. Secondly, due to the specific condition of the patient group and the medication itself (e.g., bipolar illness symptoms, drug's side effects), the adherence rate of lithium pharmacotherapy is low ($\sim 60\%$) [2,3]. The poor adherence can lead to poor treatment outcomes associated with increased risk of relapse, re-hospitalization, and suicide [4]. Standard practices of lithium monitoring for precise dosing are confined to centralized hospitals and involve invasive blood draw and high-cost lab-based analysis with long turnaround time. Moreover, currently there is no direct lithium adherence monitoring available, and the indirect monitoring solutions (e.g., pill counters) are incapable of verifying the actual intake event (inherently non-specific).

Wearable and mobile biochemical sensing technologies are suitable to overcome these limitations, because they can potentially be deployed at a large-scale to monitor the molecular-level information in a non-/minimally-invasive and real-time manner [5-7]. Particularly, recent studies have shown that many circulating biomarker molecules partition onto the fingertip surface (primarily via natural perspiration) with a relatively high flux, which can be leveraged for inconspicuous biomonitoring [8-10].

To adopt these opportunities for decentralized lithium therapy management, here we developed a touch-based non-invasive lithium monitoring solution, which features a gel-coated lithium sensing interface to collect and analyze (in-situ) the partitioned lithium ions on fingertips (Fig. 4.1). This interface was constructed using a thin organohydrogel-coated lithium ion-selective electrode (TOH-ISE), which features a uniquely developed TOH to address stability challenges associated with the sensor and the sensing modality. To elaborate, from the sensing interface aspect, in the previously demonstrated one-touch sensing, the hydrogel dehydration complicates the usage and storage of hydrogel-based sensors [11,12]. From the ion-selective sensing aspect, prolonged ISE conditioning process serves as a key challenge prohibiting the translation of ISEs in real-life applications [5, 13-15]. To overcome these challenges, by adopting a water-glycerol bi-solvent matrix, the devised TOH was endowed with an anti-dehydration property [16, 17]. When coupled with a lithium ISE, the TOH coating serves as a controlled micro-environment to condition the ISE in-situ. In this way, we eliminate the need for extensive ISE conditioning and thus enable “plug-and-sense” application.

The developed TOH-ISE was further augmented with a custom-developed ISE-specific signal interpretation framework—capable of extracting the lithium flux information from the touch-based inputs. The formed lithium monitoring solution was then validated in both ex-situ (using a custom-developed artificial fingertip setup) and in-situ (a patient under lithium-based therapy) settings. The demonstrated reliable lithium sensing capability illustrates the suitability of our touch-based solution for lithium adherence monitoring, and more broadly for managing the lithium-based pharmacotherapy.

4.2. Experimental Section

4.2.1. Materials and Reagents.

All the chemicals were purchased from Sigma-Aldrich (MO, USA), unless otherwise stated. Polyethylene terephthalate (PET, 100 μm thick) was purchased from MG Chemicals (CA, USA). Silver-silver chloride (Ag/AgCl) ink was purchased from Ercon Incorporated (MA, USA). Aqueous dispersion of PEDT:PSS conductive polymer (Clevios PH 1000) was purchased from Heraeus Heraeus Precious Metals North America Daychem LLC (OH, USA). The artificial sweat solution was purchased from Pickering Laboratories, Inc. (CA, USA) using a customized composition.

4.2.2. Fabrication and characterization of TOH

To fabricate TOH, 2 wt.% agarose and 3 wt.% artificial sweat solution (unless otherwise stated) were first mixed with a bi-solvent solution consisting of 80% deionized (DI) water and 20% glycerol. The mixture was incubated in the 80 $^{\circ}\text{C}$ water bath for 30 min. The resultant clear solution was then injected into vertically-assembled mold (fabricated following our previous protocol). After sufficient cooling, a rectangular organohydrogel was formed. The gel was picked up and dried overnight to allow for the evaporation of free water. The fabricated TOH was stored in the ambient environment if not used. To fabricate the lithium-spiked TOH, 1 mM lithium chloride (LiCl) was added into the gel solution before gelation. The thickness of TOH was measured to be $59 \pm 10 \mu\text{m}$ ($n = 6$). The measurement was performed under a microscope using a glass slide with a defined thickness as the reference.

4.2.3. Fabrication and characterization of lithium ISE

The lithium ISE was fabricated on a gold electrode, which was patterned on a PET substrate with the aid of a shadow mask (30 nm chromium/200 nm gold, electrode diameter: 2.4 mm). First, 2.5 μ L PEDOT:PSS solution was dropped onto the gold electrode and then dried at room temperature (~ 30 min). The acquired electrode was baked at 60 °C for 30 min to facilitate PEDOT conjugation. For ISM coating, the PEDOT:PSS electrode was dipped into a lithium ISM cocktail for 10 dip cycles (2 s each) and the sensor was dried for 5 min between dips. To prepare the cocktail (cocktail 1), 3 mg Li Ionophore VI, 2 mg potassium tetrakis (4-chlorophenyl)borate (KTCPB), 84 mg polyvinyl chloride (PVC), and 203 μ L 2-nitrophenyl octyl ether (NPOE) were dissolved into 3 mL tetrahydrofuran (THF). To compare the performance of different ISM in our context at hand, a second widely-used lithium ISM cocktail (cocktail 2) was also prepared. This cocktail contained 4.5 mg Li Ionophore VI, 1.5 mg KTCPB, 4.5 mg trioctylphosphine oxide (TOPO), 84 mg PVC, and 198 μ L NPOE in 3 mL THF. The fabricated ISEs were conditioned in a 10 mM LiCl artificial sweat solution for 2 h before use. Standalone ISE characterizations were performed using a standard electrochemical cell (versus aqueous Ag/AgCl reference electrode, CH Instruments, Inc. [TX, USA]). All the electrochemical measurements were performed using CHI660E or CHI1040C electrochemical workstation (CH Instruments, Inc.).

To fabricate the reference electrode, Ag/AgCl ink was first dropped onto the same gold electrode for ISE construction and dried at 65 °C for 30 min. Then a polyvinyl butyral/sodium chloride (PVB/NaCl) solution was dropped onto the Ag/AgCl electrode 3 times (4 μ L per time; 10 min interval between dropping) to eliminate the interference of Cl⁻ concentration variation. The solution was prepared by dissolving 79 mg PVB and 50 mg NaCl into 1 mL methanol. The

fabricated/conditioned lithium ISE and reference electrode were paired and taped on a PET substrate to form a full sensor.

4.2.4. Ex-situ TOH-ISE characterizations

The TOH was mounted onto a lithium sensor to form a TOH-ISE unit. The TOH-ISE was stored in an ambient environment if not used. The storage of the coupled unit also serves for in-situ ISE conditioning. The unit was conditioned for at least overnight before any testing if otherwise stated.

The TOH-ISE's response to a lithium flux input was characterized by coupling with a microfluidic artificial fingertip setup that was fabricated following our previous work. In the experiment, the potentiometric readout of the TOH-ISE was recorded continuously. After a stable baseline was obtained, the TOH-ISE was mounted onto the artificial fingertip, which delivered input fluid with different lithium concentration levels at a constant flow rate (320 nL/min/cm²). Potentiometric readout between 15-100 s post artificial fingertip contact was fitted into the described signal interpretation model (equation (2) below) to extract the flux-related signal s (Matlab). In the fitting process, we used the experimentally determined value of the slope m (57 mV/dec, from the standalone ISE characterization) to avoid overfitting. The starting time point (15 s) was experimentally determined to account for the analyte diffusion time and the contact-induced disturbance. A new TOH was used for each measurement. To characterize the effect of pressing force, weights were used to emulate force exertion with different strengths.

4.2.5. In-situ TOH-ISE characterization

One subject under lithium-based pharmacotherapy (900 mg lithium carbonate per day) and three healthy subjects (without lithium-based medication history) were recruited in the study. For each touch-based entry, the subjects were instructed to wash their index or middle fingertips with DI water before testing. The acquired potentiometric readouts were processed using the same method as the ex-situ experiments to extract the sensing signal. For saliva collection, the subjects were instructed to rinse their mouth with cold water before collection. The samples were collected via direct salivation using a Saliva Collection Aid (Salimetrics, CA, USA). The salivary lithium was quantified using a colorimetric lithium assay kit (Abcam ab235613, MA, USA) and Nanodrop One (Thermo Fisher, MA, USA).

4.2.6. Institutional Review Board Approval for Human Subject Testing

The conducted human subject experiments were performed in compliance with the protocols that have been approved by the Institutional Review Board at the University of California, Los Angeles (IRB No. 17-000170). All subjects gave written informed consent before participation in the study.

4.3. Development and characterization of individual components

Our designed touch-based lithium sensing interface consists of a thin gel (here, TOH)—which simultaneously serves as a bio-interface to sample the analyte flux from the skin surface and a medium for electrochemical analysis—and a lithium ISE to quantify sampled lithium ions. Here, the two components are first individually developed and characterized.

The agarose-based TOH was fabricated using a molding technique (Fig. 4.2A). Central to rendering an anti-dehydration property, the gel solution was prepared in a bi-solvent matrix containing water and glycerol, where hydrogen bonds were formed between water, glycerol, and agarose molecules to freeze water molecules within the gel matrix [18]. The as-fabricated organohydrogels were dried overnight to allow for the evaporation of unbound free water, resulting in a TOH with stabilized composition. As shown in Fig. 4.2B, the fabricated TOHs demonstrated negligible weight loss for a period over two weeks, illustrating its superior anti-dehydration capability. Moreover, the fabricated TOHs have a low thickness of $\sim 60 \mu\text{m}$, which will facilitate rapid TOH-sensor response and amplified signal [19].

The underlying lithium sensing interface was constructed using a solid-contact ISE, which consists of: 1) an ion-selective membrane (ISM) serving as the recognition element for selective lithium chemisorption; 2) a poly(3,4-ethylenedioxythiophene) polystyrene sulfonate (PEDOT:PSS)-based ion-to-electron transducer, featuring a large capacitance to render low sensor drift; and 3) a gold electrode patterned on a flexible polyethylene terephthalate (PET) substrate. Here, the composition of the ISM cocktail was specifically selected towards an optimal performance in a sweat-mimicking matrix (Fig. 4.3).

The developed sensor was first characterized in a standardized matrix. In a deionized water background, the sensor shows a Nernstian response to Li^+ within the range of 10^{-5} - $10^{-1.5}$ M (Fig. 4.4A), which is comparable to the previously reported Li^+ -ISEs [20, 21]. The intrinsic selectivity of the developed sensor was evaluated by testing the sensor in solutions containing either the interfering ions (e.g., Na^+ , K^+ , Ca^{2+} , Mg^{2+}) or Li^+ . As shown in Fig. 4.4B, the potentials recorded with all the interfering ions are much lower than that of Li^+ . Selectivity coefficients are not defined because the sensor does not give a Nernstian response to the interfering ions [22]. More

informatively, considering that natural perspiration is the primary source of touch-based sensing, the developed sensor was further characterized in custom-developed artificial sweat matrix [23], which effectively mimics the ionic environment of sweat. Figure 4.2C shows the sensors' response to Li^+ in artificial sweat, where a measurable signal to a Li^+ concentration as low as 10^{-5} M and a linear range slope (m) of 57 mV/dec are observed. Noting that the clinically relevant range of Li^+ in non-invasively retrievable biofluid (e.g., saliva) is $\sim 0.5 - 3$ mM (\sim twice compared to the corresponding serum concentrations) [24, 25], the developed sensor is theoretically capable of analyzing a touch-based input in presence of analyte dilution in TOH. Furthermore, Fig. 4.2D shows that the sensor's response to the variations of interfering ions was minimal as compared to that of Li^+ , demonstrating a good selectivity in the envisioned application.

4.4. TOH-ISE characterization

The individually-characterized TOH and lithium ISE were then coupled to form a TOH-ISE sensing interface, where the TOH serves as the sensing medium and ISE readout reflects the lithium level in the TOH.

We first characterize the TOH-ISE's readout stability. In conventional ISE sensing, to realize a low-drift readout, the sensor needs to undergo extensive conditioning in a sample-mimicking environment prior to the test, which is operational-complicated and time-consuming. In our TOH-ISE configuration, leveraging the high stability of the TOH, the TOH coating serves as a controlled micro-environment to condition the ISE in-situ. To demonstrate its utility, we compared the TOH-ISEs' readout drift in their as-fabricated state (here referring to the tests right after coupling TOHs with ISEs) and in-situ-conditioned state. As shown in Fig. 4.5A,B, the as-fabricated interface drifted significantly, while a small variation was observed in the in-situ conditioned case. The small drift can be attributed to the equilibrium of the functional layers in

ISE (e.g., hydration, ion activity in the ISM, PEDOT:PSS redox state) during the conditioning process. Through leveraging this feature, the TOH-ISE interface effectively eliminates the time-consuming ISE conditioning step before each use, rendering a plug-and-sense capability. To illustrate this capability, the developed TOH-ISE was interrogated at different days post fabrication. A lithium-spiked TOH was utilized to probe the interface's lithium response. As shown in Fig. 4.5C, the interface manifested a reproducible lithium response for two weeks and the sensor readout was stable for all the measurements.

Before deploying TOH-ISEs for touch-based sensing, we first developed an ISE-specific signal interpretation framework to extract the lithium flux information from the real-time touch-based readout. To start with, we refer to the Nicolsky-Eisenman equation, which empirically describes the ISE readout (EMF) in relation to the ion concentration levels in its surrounding environment:

$$EMF = \frac{RT}{z_i F} \log(a_i + \sum K_{IJ} a_j^{z_i/z_j}) + E_0 \quad (1)$$

Here i and z are the activity and the charge of the target ion (i ; in our case Li^+) and non-target ion (j), respectively; K_{IJ} is the selectivity coefficient for each interfering ion; E_0 is the standard potential of EMF ; and R , T , and F represent the universal gas constant, the absolute temperature, and the Faraday constant, respectively. Unlike the conventional sample-to-answer biochemical sensing scenarios, in the touch-based sensing, the epidermal influx of the analyte (here, f_I) into the gel-based interface dynamically changes its concentration in the gel. On the other hand, by optimizing the ionic composition (i.e., non-target ion concentrations) of the TOH, we verified that the contribution of non-target ion concentrations remains constant during a touch-based entry (time-independent, Fig. 4.6). Accordingly, the dynamic sensor readout as be presented as:

$$EMF(t) = \frac{RT}{z_I F} \log \left(f_I \cdot t + \sum K_{IJ} a_I^{z_I} \right) + E_0 = m \cdot \log(s \cdot t + 1) + E'_0 \quad (2)$$

To this end, the sensing signal (s , proportional to analyte flux) can be extracted by fitting the TOH-ISE readout into the equation above.

To validate the TOH-ISE interface and signal interpretation framework, we coupled the TOH-ISE with our previously developed microfluidic artificial fingerprint setup, which mimics a skin surface that continuously delivers analytes onto the sensing interface. As shown in Fig. 4.5D, upon lithium introduction, the sensor readout gradually increased, reflecting the introduced lithium flux. Then, the introduced lithium concentrations were modulated to model the variation of circulating lithium levels. Figure 4.5E,F show the real-time potentiometric readouts of the interface and the corresponding calibration curve constructed based on the aforementioned interpretation framework ($R^2 = 0.98$). Relevant to the touch-based sensing context, we also investigated the influence of the pressing force variability on the TOH-ISE readout. Figure 4.7 shows that mounting weights on the TOH-ISE did not cause sensor readout change, which is primarily due to the minimal electron motion involvement in the case of potentiometric sensing.

4.5. In-situ TOH-ISE characterization

We further validated the performance of the developed TOH-ISE in an in-situ lithium adherence monitoring study. To this end, a subject prescribed to lithium-based medication was recruited. Touch-based sensing using the TOH-ISE interface was performed multiple times before and after the scheduled drug intake (900 mg lithium carbonate): ~ 0-1 h pre-intake and ~ 1-2 h post-intake. To demonstrate the physiological significance of the touch-based readouts, saliva samples were collected at around the same time and analyzed using a standard colorimetric assay. The choice of saliva was motivated by lithium's reported saliva-blood correlation as well as the

similar analyte partitioning pathway of sweat and saliva. As a control experiment, touch-based sensing and salivary lithium analysis were also performed on three health subjects, where circulating lithium is expected to be negligible.

Figure 4.8A-C shows the representative raw and fitted TOH-ISE readouts from the three scenarios. Compared to the pre-intake case, a larger signal was obtained post the drug intake, inferring an elevated circulating lithium level. A near-zero signal was recorded from the healthy subject. As shown in Fig. 4.8D, collectively TOH-ISE readouts and saliva lithium levels follow the same trend, demonstrating the potential utility of the touch-based non-invasive sensing for direct drug adherence monitoring application.

4.6. Reference

1. Mitchell, P. B. *British journal of clinical pharmacology*, 52(S1), 45-54, 2001.
2. Lingam, R., & Scott, J. *Acta Psychiatrica Scandinavica*, 105(3), 164-172, 2002.
3. Sajatovic, M., Valenstein, M., Blow, F., Ganoczy, D., & Ignacio, R. *Psychiatric Services*, 58(6), 855-863, 2007.
4. Chakrabarti, S. *World journal of psychiatry*, 6(4), 399, 2016.
5. Gao, W., Emaminejad, S., Nyein, H. Y. Y., Challa, S., Chen, K., Peck, A., Javey, A. *Nature*, 529(7587), 509-514, 2016.
6. Kim, J., Campbell, A. S., de Ávila, B. E. F., & Wang, J. *Nature biotechnology*, 37(4), 389-406, 2019.
7. Parlak, O., Keene, S. T., Marais, A., Curto, V. F., & Salleo, A. *Science advances*, 4(7), eaar2904, 2018.
8. Nyein, H. Y. Y., Bariya, M., Tran, B., Ahn, C. H., Brown, B. J., Ji, W., & Javey, A. *Nature*

- communications*, 12(1), 1-13, 2021.
9. Tang, W., Yin, L., Sempionatto, J. R., Moon, J. M., Teymourian, H., & Wang, J. *Advanced Materials*, 33(18), 2008465, 2021.
 10. Ichimura, Y., Kuritsubo, T., Nagamine, K., Nomura, A., Shitanda, I., & Tokito, S. *Analytical and bioanalytical chemistry*, 413(7), 1883-1891, 2021.
 11. Lin, S., Wang, B., Zhao, Y., Shih, R., Cheng, X., Yu, W., & Emaminejad, S. *ACS sensors*, 5(1), 93-102, 2019.
 12. Sempionatto, J. R., Moon, J. M., & Wang, J. *ACS sensors*, 6(5), 1875-1883, 2021.
 13. Shao, Y., Ying, Y., & Ping, J. *Chemical Society Reviews*, 49(13), 4405-4465, 2020.
 14. Criscuolo, F., Cantu, F., Taurino, I., Carrara, S., & De Micheli, G. *IEEE Sensors Journal*, 21(8), 9649-9656, 2020.
 15. Criscuolo, F., Taurino, I., Stradolini, F., Carrara, S., & De Micheli, G. *Analytica Chimica Acta*, 1027, 22-32, 2018.
 16. Wu, Z., Yang, X., & Wu, J. *ACS Applied Materials & Interfaces*, 13(2), 2128-2144, 2021.
 17. Wu, J., Wu, Z., Xu, H., Wu, Q., Liu, C., Yang, B. R., & Norford, L. K. *Materials horizons*, 6(3), 595-603, 2019.
 18. Boral, S., & Bohidar, H. B. *The Journal of Physical Chemistry B*, 116(24), 7113-7121, 2012.
 19. Lin, S., Zhu, J., Yu, W., Wang, B., Sabet, K. A., Zhao, Y., & Emaminejad, S. *Proceedings of the National Academy of Sciences*, 119(15), e2201937119, 2022.
 20. Novell, M., Guinovart, T., Blondeau, P., Rius, F. X., & Andrade, F. J. *Lab on a Chip*, 14(7), 1308-1314, 2014.
 21. Sweilam, M. N., Varcoe, J. R., & Crean, C. *ACS sensors*, 3(9), 1802-1810, 2018.
 22. Bakker, E., Pretsch, E., & Bühlmann, P. *Analytical chemistry*, 72(6), 1127-1133, 2000.
 23. Wang, B., Zhao, C., Wang, Z., Yang, K. A., Cheng, X., Liu, W., & Emaminejad, S. *Science*

advances, 8(1), eabk0967, 2022.

24. Shetty, S. J., Desai, P. B., Patil, N. M., & Nayak, R. B. *Biological trace element research*, 147(1), 59-62, 2012.
25. Serdarević, N., Kozjek, F., & Malešič, I. *Bosnian journal of basic medical sciences*, 6(4), 32, 2006.

Chapter 5. Voltammetric sensing interfaces for non-invasive wearable electroactive pharmaceutical monitoring

5.1. Introduction

To realize the vision of personalized medicine, which aims to deliver the right patient, with the right drug, at the right dose, personalized pharmacotherapy solutions are necessary [1, 2]. Currently, medication dosage is generally prescribed by relying on the drug manufacturer's recommendation, which is based on statistical averages obtained from testing the medication on a relatively small patient sample size [3, 4]. Therefore, at the individual level the prescribed dosage may fall outside the optimal therapeutic concentration window, resulting in adverse events in patients and/or ineffective pharmacotherapy [5, 6]. To address such issues, personalized therapeutic drug monitoring (TDM) is essential, as it can guide dosing by capturing the dynamic pharmacokinetic profile of the patient's prescribed medication during the course of the treatment [7-10]. However, because of the invasiveness, high cost, and long turn-around time of the available TDM techniques (mostly rely on repeated blood draws and assays performed in offsite central labs), they are applied in rare occasions and at suboptimal rates [11, 12].

In that regard, wearable and mobile biochemical sensing technologies, capable of analyzing non-invasively retrievable biofluids, are suitable solutions, because they can potentially be deployed at a large-scale to monitor the individuals' drug pharmacokinetic profiles (semi)continuously and longitudinally [13-18]. Specifically, in the context of biofluids such as sweat and saliva, the free (unbound) drug molecules are speculated to diffuse into the secreted biofluids with high degrees of correlation with blood (owing to their low molecular weight, < a

few kDa) [19, 20]. Therefore, in principle, these non-invasive sensing modalities can be adopted to provide proxy measures of target drug concentration in blood (Fig. 5.1A).

Accordingly, sensor development strategies are required to render sample-to-answer drug detection capabilities within a compact footprint. In that regard, voltammetry-based approaches have been introduced to target electroactive drugs, which do not rely on recognition elements [21, 22]. These approaches transduce the target's redox chemical signature into a measurable electrical signal using millimeter-sized sensing electrodes. To adapt such approaches for the envisioned translational applications, the fundamental challenges inherent to complex biofluid analysis must be addressed.

One such challenge is the distortion/burial of the target's redox signature in the measured voltammogram, which is due to superimposing voltammetric responses of endogenous electroactive species ("interference"). Additionally, biofouling is another challenge relevant to the context at hand, which is widely investigated for the conventional biofluids (e.g., blood) [22, 23], but overlooked in the context of sweat analysis. Biofouling stems from the adsorption of surface-active agents (e.g., proteins, peptides, amino acids) onto the sensor's surface [24, 25]. This adsorption layer inhibits the analyte interaction with the electrode, which may lead to signal degradation.

Here, to resolve the selectivity challenges, I first presented a framework, which centers on the evaluation and determination of suitable sensing electrodes for voltammetric analysis and characterization of endogenous interferents. Based on the examination of the voltammetric performance of carbon-based electrode candidates (which in principle can characterize the oxidation of drug molecules), the boron-doped diamond electrode (BDDE) was determined to be a suitable sensing electrode owing to its wide electrochemical potential window and high

operational stability. With a deliberate surface treatment of the BDDE, nano- to sub/low-micromolar level quantification capability was realized for all the target drugs. Furthermore, the interference of a panel of physiologically-relevant endogenous electroactive species (including uric acid and amino acids) was characterized in relation to the quantification of the target drugs.

These studies led to the identification of “undistorted potential windows”, within which reliable electroactive target detection in sweat matrix was demonstrated. To generalize this methodology and apply it to the targets with redox peaks falling outside the original undistorted potential windows, I further devised a wearable voltammetric sensor development strategy that centers on tuning the molecule-surface interactions. We specifically tailored our strategy to target acetaminophen (APAP) as a model electroactive drug molecule with reported saliva-blood correlation [26, 27], which is a widely-used analgesic and antipyretic, and its supratherapeutic administration is the leading cause of liver failure in the United States [28]. To engineer an APAP sensing interface, the surface termination of the working electrode was adjusted to decouple the undesired interference (via tuning the electron transfer kinetics pertaining to redox reactions), and a polymeric membrane was incorporated to reject surface-active agents (also, to further reject undesired interference). These orthogonal intrinsic/extrinsic surface treatments converged to the development of a Nafion-coated and hydrogen-terminated boron-doped diamond electrode (Nafion/H-BDDE), which simultaneously mitigates biofouling and creates undistorted potential windows encompassing the APAP’s oxidation peak. Using this engineered sensing interface, accurate and reliable quantification of APAP in saliva and sweat was realized (cross-validated with lab-based assays, $R^2 \sim 0.94$).

To realize a wearable solution, the engineered sensing interface was integrated within a custom-developed smartwatch (capable of sweat sampling/routing, signal acquisition, and data

display/transmission), where the voltammetric readouts were processed by a dedicated analytical framework for target redox peak extraction (Fig. 5.1B,C). To illustrate its clinical utility, we applied this wearable solution to construct the pharmacokinetic profile of APAP in sweat (in relation to saliva), and accordingly, demonstrated the significance of sweat-based drug readings. By harnessing the demonstrated real-time and reliable drug quantification capabilities, our generalizable solution can be positioned as a viable therapeutic drug monitoring approach to enable personalized pharmacotherapy.

5.2. Experimental Section

5.2.1. Materials and Reagents.

Acetaminophen, uric acid, L-tyrosine, L-tryptophan, ascorbic acid, L-Methionine, L-Histidine, Nafion perfluorinated resin solution (5 wt%), and acetaminophen-D4 solution (100 $\mu\text{g}/\text{mL}$ in methanol) were purchased from Sigma-Aldrich (MO, USA). PBS (1 \times , Gibco PBS, pH 7.2), isopropyl alcohol, and all the reagents used in the high performance liquid chromatography (HPLC) were purchased from Fisher Scientific (MA, USA). Polyethylene terephthalate (PET, 100 μm thick) was purchased from MG Chemicals (BC, Canada). Double-sided tape (170 μm thick, 9474LE 300 LSE) and Scotch single-sided self-seal laminating sheets were purchased from 3M Science (MN, USA). BDDE sensor (reference electrode: silver, counter electrode: carbon) was purchased from Metrohm USA (FL, USA). SPCE (TE100) was purchased from CH Instruments Inc. (TX, USA).

5.2.2. Electrode preparation and electrochemical measurements.

The electrochemical measurements were performed using a CHI660E electrochemical workstation (CH Instruments, Inc.). To alter the BDDE surface from H-termination to O-termination, anodic treatment was performed in an electrochemical cell (+2 V vs. silver/silver chloride, Ag/AgCl, for 5 min) containing 0.5 M sulfuric acid (H₂SO₄). Electrochemical cleaning of BDDE was performed by cyclic voltammetry (CV) each time before use in 0.5 M H₂SO₄. Accordingly, for H-BDDE, the CV scanning was performed in the potential range of -0.5 V - 1.5 V (vs. Ag/AgCl, scan rate: 0.5 V/s, 10 cycles). For O-BDDE, a CV scanning range of -0.5 V - 2.8 V was used. Nafion coating was performed by drop casting 1.8 μ L 5wt% Nafion solution onto the working electrode, followed by drying in the ambient environment.

DPV measurements were performed with increment: 5 mV, amplitude: 50 mV, pulse width: 0.1 s, sampling width: 16.7 ms, pulse period: 0.5 s. In continuous DPV measurements, given the unidirectional nature of the applied DPV potential waveform (here, only scanning within the oxidation reaction range without a cyclic renewal), progressive analyte depletion and product built-up can occur. Accordingly, a constant potential of -0.4 V was applied across the working and reference electrodes for 0.5 s before each DPV scan. In the characterization of biofouling effect, the peak current levels from the measurements were extracted using the analytical framework.

The glassy carbon electrode was purchased from Bioanalytical Systems, Inc. (IN, USA). Each time before use, the glassy carbon electrode was pretreated by polishing with diamond suspension (1 μ m), followed by ultrasonication in ethanol (5 min) and deionized (DI) water (5 min). The screen printed carbon electrode was purchased from CH Instruments Inc. Comparison of carbon electrodes and sensor calibration were performed in an electrochemical cell (0.01 M acetate buffer, pH = 5, reference electrode: Ag/AgCl, counter electrode: platinum, Pt).

5.2.3. Sweat and saliva collection and ex-situ measurement.

For sweat stimulation and collection, a standard iontophoresis protocol was followed using the Macroduct® Sweat Collection System (ELITechGroup Inc., UT, USA). First, the volar surface of the human subject's forearm was cleaned with isopropyl alcohol and deionized water. Next, 5-min iontophoresis was performed using the pilocarpine-loaded hydrogels and a Webster sweat inducer. The secreted sweat was then collected with the Macroduct sweat collector for 30 min. To track the circulating temporal profile of APAP in sweat, iontophoresis was performed four times, at ~1 hour before, and ~10 min, ~70 min, and ~130 min after the oral administration of a medication containing 650 mg APAP (Regular Strength Pain Relief, CVS Health), respectively. Saliva samples were collected by direct salivation into plastic vials with the aid of the Saliva Collection Aid (Salimetrics, CA, USA). The subjects were instructed to rinse their mouths with cold water before saliva collection. To track the circulating temporal profile of APAP in saliva, saliva samples were collected before and 30, 60, 90, 120, 150 min after the APAP administration. Collected sweat and saliva samples were stored at -20 °C before use.

Saliva samples were centrifuged at $14,000 \times g$ for 10 min before performing measurements. To quantify APAP concentration in the samples, 40 μL of the sweat/saliva sample was drop-cast onto the sensor, followed by the DPV scanning. To calibrate the DPV readout, the respective APAP-less sweat or saliva sample (prior to the medication administration, from the same subject) was spiked with 1 mM APAP stock solution (in PBS) to construct a 50 μM -calibrator. The peak current from the calibrator (measured after the real samples) was used to calibrate the previous measurements.

5.2.4. APAP quantification with LC-MS/MS.

The APAP concentrations in the sweat and saliva samples were measured by LC-MS/MS with a multiple reaction monitoring (MRM) technique. Deuterium-labeled APAP (APAP-D₄) was used as the internal standard (IS). For calibration, various concentrations of APAP were spiked into water (Optima™ LC/MS grade) to make standard solutions of 0, 1, 10, 50, 100, 200, 200, 500 nM. The sweat and saliva samples were first centrifuged at 14,000 × g for 10 min and 1 μL supernatant was diluted into 498.5 μL water. Then 0.5 μL 1 μg/mL IS was spiked into 499.5 μL of calibrator or diluted biofluid samples (to reach a final IS concentration of 10 ng/mL). Molecular weight cutoff (MWCO) filtering was used to remove particulate matter from the sample. Accordingly, the IS-spiked samples were loaded into the 10 kDa MWCO centrifugal filters (Amicon Ultra-0.5, Sigma-Aldrich), and centrifuged at 14,000 × g for 10 min. The low molecular weight filtrate was then transferred into an autosampler vial for APAP quantification.

The HPLC setting followed our previously reported protocol (Chapter 2). The tandem mass spectrometry was operated in MRM mode recording the following m/z transitions: 152.2→110.1 for APAP and 156.2→114.1 for APAP-D₄. The declustering potential, entrance potential, collision energy, and collision cell exit potential were optimized at 56 V, 10 V, 23 V, and 6 V for APAP, and 71 V, 10 V, 21 V, and 6 V for APAP-D₄, respectively. Ionspray voltage and temperature were 5500 V and 400 °C, respectively. Collision gas, curtain gas, and ion source gas 1 and 2 were set at 4, 30, 30, and 50 psi, respectively.

5.2.5. Construction of microfluidic interface.

The microfluidic interface was created by vertically stacking multiple laser-patterned (VLS2.30, Universal Laser Systems) layers (including PET, double-sided tape, and single-sided

laminating sheets). The microfluidic interface consisted of a sweat sampling chamber and a sweat sensing chamber, fluidically connected using a vertical interconnect access (VIA). The sweat sampling chamber was created by stacking the double-sided tape layer (with the same dimension as the iontophoretically-stimulated area, diameter: 28 mm) onto a PET layer. To minimize the dead-sweat volume, a spacer was incorporated in the microfluidic interface, formed by stacking three layers of single-sided laminating sheets. The sweat sensing chamber was created by stacking PET cover and double-sided tape layers onto the sensor substrate.

5.2.6. Wireless electronic module and smartwatch design.

The wireless DPV readout was realized with a custom-developed printed circuit board (PCB). An onboard MCU (Atmega328, Microchip Technology, AR, USA) was utilized to program the applied potential waveform and acquire the readout signal. Specifically, the DPV excitation potential waveform and the cathodic electrical pulse (with the same parameters as the potentiostat measurements) were applied across the working and reference electrodes through a 16-bit DAC (DAC8552, Texas Instrument, TX, USA). The current response from the working electrode was acquired as a digital voltage output with the aid of a TIA (LT1462, Linear Technology, CA, USA) and a 12-bit ADC (ADS1015, Texas Instruments). The collected current response (through inter-integrated circuit protocol, I2C) was then used to construct the differential pulse voltammogram within the MCU. A wireless, bilateral, and real-time communication was achieved between the PCB and the user interface by an onboard Bluetooth module (AMB2621, Würth Elektronik, Germany). Moreover, the MCU communicated with a 1.44" color thin-film-transistor LCD screen (SF-TS144C-9082A-N, Shenzhen SAEF Technology, China) to display the acquired voltammogram. The sensor was connected to the PCB with the aid of a flat flexible cable (Molex,

IL, USA) and a double-sided adhesive anisotropic conductive film (9703, 3M). A single, miniaturized, rechargeable lithium-ion polymer battery with a nominal voltage of 3.7 V was used to power the PCB. A smartwatch case was 3D printed to accommodate all the functional modules (sensor, microfluidic module, and electronic module) and battery. The developed smartwatch was adhered onto the subject's wrist with the aid of the double-sided adhesive tape.

5.2.7. On-body tracking of APAP metabolic profile.

Each iontophoresis test was performed following the same protocol used in the ex-situ testing. The devised voltammetric sensing system was then mounted onto the stimulated skin surface to perform DPV measurements (during the course of the sweat secretion). Saliva samples were collected during and in between the sweat analysis. Saliva analysis was performed using circuit-interfaced sensors, similar to the ex-situ study. The APAP concentration was calculated by peak information extraction (via analytical framework) and post-calibration.

5.2.8. Analytical framework for peak height information extraction.

To extract the APAP oxidation peak information from the voltammograms, the voltammetric baseline outside the peak region was fitted using the combination of a 3rd-order polynomial and exponential equation in MATLAB (Mathworks), where proper initial values were set for all the unknown variables:

$$I_{baseline} = a_1V^3 + a_2V + a_3 + a_4 \times \exp(a_5V) \quad (1)$$

The APAP oxidation peak information was extracted by subtracting the estimated baseline from the corresponding raw readout.

5.2.9. Pharmacokinetic analysis.

A single-compartment model was used to construct the pharmacokinetic profiles of APAP in sweat and saliva. To fit the captured readouts into the model, first, the readouts in the elimination phase were plotted in the semilogarithmic scale and linearly-fitted. The pre-exponential factor A was determined as the y-intercept of the fitted curve (extrapolated) [29]. Then other parameters (t_0 , K_{el} , and K_a) are fitted using the non-linear least square regression algorithm (MATLAB).

5.2.10. Institutional Review Board (IRB) approval for human subject testing.

The conducted human subject experiments were performed in compliance with the protocols that have been approved by the IRB at the University of California, Los Angeles (IRB#17-000170). Subjects without recent APAP administration history were recruited. All subjects gave written informed consent before participation in the study.

5.3. Determination of suitable sensing electrode for electroactive drug analysis.

To adapt voltammetry for drug monitoring applications, first, a sensitive and inherently stable sensing electrode needs to be selected. To this end, carbon electrodes are particularly suitable because of their wide electrochemical potential window, which allows for the characterization of drug molecules with high oxidation potential (> 1 V) [30]. To determine a suitable electrode, the voltammetric performance of different carbon electrodes were evaluated. Two widely-used sp^2 carbon-based electrodes (glassy carbon electrode, GCE, and screen printed carbon electrode, SPCE) were selected and compared with BDDE. Because of its unique sp^3 diamond structure, BDDE manifests various superior properties for electrochemical sensing

application, including the wide electrochemical potential window, low background current, high fouling resistance and biocompatibility, relatively rapid electron transfer kinetics, and long-term stability under high-potential operation [31, 32].

The electrochemical potential windows of the selected carbon electrodes were first characterized to define the suitable potential window for electroanalysis while avoiding the electrolysis of the biofluid. Because of the potentially high oxidation potential of the target drug molecules, and broadly, to enable the analysis of a larger panel of electroactive drugs, a wide potential window is desired. Here, the potential window was defined with the aid of cyclic voltammetry (CV) and by setting the cutoff current density as $50 \mu\text{A}/\text{cm}^2$ [33]. As shown in Fig. 5.2A, BDDE exhibits the widest potential window as compared to GCE and SPCE, which arises from its high overpotential for solution decomposition. Within the electrochemical potential window, a low and stable background current is desired for high signal-to-background ratio voltammetric analysis. The background current level is related to the double layer capacitance at the electrode-electrolyte interface, which can be effectively characterized by CV measurement [34]. The double layer capacitance of the tested BDDE was $\sim 8 \mu\text{F}/\text{cm}^2$, which was less than 1/3 of that of the GCE, implying a lower background current is to be expected when performing voltammetric measurements with BDDE [32].

Next, the stability of background current under long-term operation at high potential was evaluated across the three carbon electrodes. Figure 5.2B shows that, under a constant voltage of 1.2 V, progressive baseline current drift occurred in the cases of GCE and SPCE, which can be attributed to the surface oxidation reaction of sp^2 carbon [35]. Conversely, no significant baseline current change was observed for the case of BDDE, which can be attributed to its microstructural

stability and resistance to oxidative damage [31]. These results demonstrate the superior long-term stability of BDDE even at high-voltage operation.

Given its desirable properties for voltammetry-based drug analysis (as characterized and discussed above), hereafter, BDDE is selected to three model electroactive drugs—dipyridamole (DP), acetaminophen (APAP), and caffeine (CAFF), which can be electrochemically oxidized at low (< 0.5 V), medium (0.5 - 1 V) and high (> 1 V) potentials respectively [36-38]. These drugs were selected, in particular, because of their significance in disease treatment and the demonstrated utility of monitoring them for improving patient outcomes. For example, DP is used for the cardiovascular diseases treatment due to its vasodilating and antiplatelet properties, and monitoring of antiplatelet therapies has been demonstrated to be critical for stroke patients [39, 40]. APAP is a widely-used pain reliever and fever reducer with remarkable variation in metabolism, and therapeutic monitoring can help to control the patients' exposure to its potentially toxic metabolite [41]. CAFF is used in the treatment of airway obstruction and prematurity apnea, and therapeutic monitoring has shown to be useful in individualizing dosage to reduce drug toxicity [42, 43].

The electrochemical response of BDDE can be tuned by modifying its surface termination to optimize its quantification capability toward the target drugs [44]. The surface of the as-deposited BDDE is typically hydrogen-terminated, while anodic treatment can effectively alter the surface to be oxygen-terminated [45]. As the surface termination of BDDE can affect the electrolyte organization at the electrode-electrolyte interface and the electron transfer kinetics, the suitability of the surface chemistry must be examined in relation to each drug. Here, the redox responses of the three target drug molecules in their physiological relevant concentration range were characterized by CV using anodic-treated and untreated BDDEs. As shown in Fig. 5.2C, for

anodic-treated BDDE (oxygen-terminated), three well-separated oxidation peaks were observed in the cyclic voltammogram, while for the case of untreated electrode (hydrogen-terminated), only APAP presented a clear electro-oxidation response with a small, overlapped DP oxidation peak on its left shoulder. The oxidation of CAFF on untreated BDDE is not evident in the voltammogram, because of the high current background level. These observations illustrate the utility of the anodic-treated BDDE to render simultaneous and high sensitivity quantification of the target drug molecules.

Among the common voltammetry techniques, here, DPV was adopted for the quantification of target drugs, because it allows for mitigating the contribution of non-faradaic background, and thus, achieving high signal-to-background ratio measurements. The voltammograms of DP, APAP, and CAFF (for different concentration levels, within their physiological relevant range) are shown in Fig. 5.2D-F). The calibration curves were shown in the insets respectively, where the peak current information was extracted with the aid of the background (measurement without analyte) subtraction. These results demonstrate that oxidation peaks can be recorded in nano- to sub/low-micro-molar level for all the model drugs, demonstrating the suitability of the adapted electroanalytical sensing approach for the envisioned applications, in terms of meeting the limit of detection criterion. To provide a measure of comparison, the responses of target drugs were also recorded by SPCE and GCE. As shown in Fig. 5.3, generally, BDDE rendered measurements with higher signal-to-background ratio, as compared to SPCE and GCE, validating BDDE's superior properties for the context at hand.

5.4. Interference study to determine operational window for electroactive drug analysis

To adapt the devised sensing approach for the analysis of complex and untreated biofluid samples, the interference of non-target species must be characterized. For the context at hand, specifically, the voltammetric response of endogenous electroactive species within the biofluid can lead to the burial of the target drug's voltammetric characteristic peak. Accordingly, five highly electroactive model interferents (with widely spread oxidation potential) are selected [46-49], which are present in human sweat at relatively high- and with dynamically varying concentration levels [50-54]. The interferents include amino acids (tryptophan, TRY, tyrosine, TYR, methionine, MET, and histidine, HIS) and uric acid (UA), which are listed in Fig. 5.4A, along with their previously characterized concentration ranges in sweat [50, 54].

The contribution of each electroactive interferent to the voltammetric background current was first investigated and characterized. As can be seen in Fig. 5.4A and Fig. 5.5, upon the introduction of each interferent in a test buffer (acetate buffer, pH = 5), the corresponding voltammetric background currents were significantly distorted (due to the respective interferent's oxidation reaction). To quantify the relative distortion of the background current by each of the interferents, a potential window of influence is defined, which captures the potential range where the spiked interferent causes greater than 50% change to the original background current. The observed extended potential windows of influence for the tested amino acids (spanning from the respective oxidation peak positions to relatively high potential levels, > 1.2 V), can be attributed to the complex cascade mechanisms involved in the oxidation of the amino acids as well as the reactants or products adsorption [48, 55].

To determine the potential ranges unaffected by the interferents (namely, undistorted potential windows), which present opportunities for selective drug detection, the characterized

potential windows of influence were annotated in relation to the voltammetric response of the model drug molecules. As illustrated in Fig. 5.4B, the undistorted potential window in our context is 0 - 0.5 V, which can be uniquely exploited to target DP. To verify this point, the voltammograms of solutions (acetate buffer, pH = 5) containing the model drugs alone were obtained and compared with that of the respective solutions spiked with the interferents oxidized at proximal potential (of the model drug). As shown in Fig. 5.4C, the fingerprint peak of DP was still visible after the addition of interferents. On the other hand, as shown in Fig.5.4D,E, the fingerprint peak of APAP and CAFF were buried after the introduction of the interferents. Furthermore, voltammetric drug quantification was performed in artificial sweat (pH = 5) as a test buffer, which in addition to the characterized interferents include other amino acids, metabolites and minerals (in their physiological relevant concentration), mimicking a complex biofluid matrix. Comparing the voltammograms of the blank artificial sweat (as background) and drug-spiked artificial sweat samples, yields a distinguishable peak corresponding to the DP oxidation, while the oxidation peaks of the other two target drug molecules were buried in the background (Fig. 5.4F).

While these results suggest that voltammetric quantification in the distorted potential window (here, applicable to APAP and CAFF) warrants additional efforts (e.g., sensor surface modification and/or calibration via a dedicated analytical framework), they inform the feasibility of DP quantification with the readily devised and described voltammetric sensing interface. To further validate the suitability of the approach for DP quantification in a complex biofluid matrix, a complementary selectivity study was performed, illustrating the minimal interference of non-electroactive species (Fig. 5.6). Furthermore, voltammetric DP calibration was performed in artificial sweat with the devised sensing interface. As shown in Fig. 5.4G, the results indicate that

50 nM limit of detection can be achieved in a complex matrix, which is similar to that achieved in the acetate buffer solution containing the target only.

5.5. Wireless voltammetric sensing system for wearable electroactive drug analysis

The findings from the studies performed within the presented framework (including establishing the appropriate sensing electrode and electroanalytical method as well as defining the operational window for undistorted voltammetric analysis) can be leveraged to design a voltammetric BDDE-based sensing system to render sample-to-answer drug readouts. To this end, circuit-level DPV-based signal excitation/acquisition as well as wireless transmission capabilities need to be developed and integrated in a small footprint. In this context, the excitation signal is a differential pulse potential waveform (potential pulses superimposed upon a staircase waveform), which is applied across the working and reference electrodes. The sensor current output can be acquired with the aid of a transimpedance stage, which converts the current signal into voltage.

Accordingly, a Bluetooth-enabled DPV circuit board is custom-developed (Fig. 5.7A), which implements the required system-level operations (Fig. 5.7B) seamlessly, following the circuit specifications informed by the aforementioned characterizations with the potentiostat. At its core, the circuit board utilizes an MCU to program the required excitation potential waveform (with the aid of a DAC) and to retrieve the TIA-processed readout signal (with the aid of a peripheral ADC). Figure 4c,d illustrate a representative circuit-rendered differential pulse potential waveform and a real-time continuous current readout, respectively. The difference of the averaged current before upward and before downward voltage change (annotated in Fig. 5.7D,E) was used to construct the DPV voltammogram (Fig. 5.7E) from the recorded current response.

To accurately extract the peak height information from the voltammogram, the DPV readouts must be augmented with an analytical framework for background current estimation and correction. In that regard, here a combined 3rd-order polynomial and exponential relationship was utilized to estimate the background current, similar to previous efforts [56]. The versatility of this function has been proven to be useful in providing an accurate estimation of the current background, which is particularly advantageous over linear fitting when quantifying low concentration target analytes where the analyte oxidation peak is likely to be distorted by a rising/descending background. Accordingly, the residual measured current outside the peak window was first fitted to the proposed relationship to generate the estimated background current [57]. Then, as illustrated in Fig. 5.7F, the peak height information was extracted by subtracting the derived background from the current measurements. The circuitry-based readings were subsequently validated by comparing the background-corrected measurements with that obtained by the lab instrument ($R^2 = 0.99$, Fig. 5.7G).

To demonstrate the utility of the devised approach to render sample-to-answer drug readouts in epidermally-retrievable biofluids, the DP concentration level in spiked sweat samples were quantified by the developed sensing system and analytical framework. Accordingly, standard iontophoresis protocol⁴² was followed to obtain a sweat sample from a healthy human subject without DP administration history (hence expecting zero amount of DP in the sweat sample). The obtained sweat sample was aliquoted and spiked with DP to construct four calibration samples and two test samples (4.0 and 8.0 μM). The BDDE-based voltammetric sensing system and analytical framework was then adapted to analyze the four calibration samples in order to construct the response curve (Fig. 5.7H, Fig. 5.8). It is worth noting that the difference of the sensor response in the actual vs. artificial sweat samples can be attributed to the difference in the composition of the

two matrices. The response curve constructed by the spiked sweat samples was used to infer the DP concentration levels of the subsequently introduced two test samples. As shown in Fig. 5.7H, the estimated DP concentration levels for the respective test samples were 4.3 μM and 7.5 μM (representing <10% error). These results further validate the capability of the developed BDDE-based voltammetric sensing system and analytical framework for accurate electroactive drug quantification in complex biofluids such as sweat.

5.6. Surface engineering to render undistorted and fouling-resistant voltammetric sensing

Furthermore, we geared our engineering efforts to target drug molecules whose redox peak originally fall within the “undistorted potential windows”. In the aforementioned interference study of sweat, the voltammetric response of APAP (our target here) overlaps with UA, Tyr, and Trp. Here, we first focused on systematically characterizing their voltammetric responses in relation to that of the APAP, in order to guide our sensor development efforts.

The voltammetric responses of electroactive species are controlled by the electron transfer kinetics of their corresponding redox reactions at the sensor surface, which are represented by parameters such as electron transfer rate constant and the redox species’ surface concentrations [58, 59]. By modulating these parameters—*via* tuning the sensing electrode’s surface properties (e.g., surface polarity or morphology)—the reactions of concerns can be selectively accelerated or suppressed [60, 61]. Thus, through elaborate surface engineering, we can decouple the voltammetric response of the target from that of the interferents, such that the target redox peak(s) fall within the undistorted potential window(s) [61-64].

To construct the sensing interface, we used BDDE as the working electrode, because of its wide electrochemical potential window, low background current, intrinsically high biofouling-

resistance, and high operational stability [65-57]. The surface chemistry of the BDDE can be tuned by adjusting its surface termination (effectively, altering the BDDE's surface states), an attribute that can be exploited as a degree of freedom for tuning the reaction kinetics of various analytes. Examples of BDDE termination include hydrogen- and oxygen-termination, which were previously exploited for the electroanalysis of electroactive species [68]. Accordingly, here we used as-deposited BDDE, with default hydrogen-termination, and we performed anodic treatment on BDDE to achieve oxygen-termination [65].

Our voltammetric characterization of the selected interferents (UA, Tyr, Trp, performed individually) in phosphate-buffered saline (PBS), using an oxygen terminated-BDDE (O-BDDE), informed an undistorted potential window spanning from 0 - 0.3 V. The voltammetric characterization of APAP, using the same interface, yielded an oxidation peak location at ~0.65 V, which overlaps with the oxidation peaks of all three interferents (Fig. 5.9A). The same characterization experiments were performed using a hydrogen terminated-BDDE (H-BDDE), the results of which are illustrated in Fig. 5.9B. As compared to the O-BDDE case, the H-BDDE-measured oxidation peak of APAP was shifted to a less positive potential relative to Tyr and Trp, informing the decoupling of the interference of Tyr and Trp. However, this surface termination change also leads to the shift of UA's oxidation peak to a lower potential, which overlaps with that of APAP. It is worth noting that the larger response and the lower oxidation potential of APAP indicates its higher electron transfer rate on H-BDDE [69]. This observation is aligned with previously reported characterization of APAP oxidation [70, 71] and may be attributed to the enhancement in the interaction of APAP and reduced-carbon surface [72].

To eliminate the interfering voltammetric response of UA, a surface modification step was incorporated in our surface engineering approach, as an additional measure, orthogonal to the

devised surface termination adjustment. Noting that UA is predominantly present in its negatively-charged form (urates) in physiologically relevant pH (given its $pK_a = 5.6$) and APAP is electrically-neutral, here, we selected a negatively-charged permselective membrane to repel urates from approaching the sensing surface. Specifically, we chose Nafion, because it features negatively-charged sulfonate groups in its polymer chain, and it was demonstrated to possess anti-fouling effects [73, 74]. As shown in Fig. 5.9C, the voltammetric response of UA, measured by a Nafion-coated H-BDDE (Nafion/H-BDDE), was significantly suppressed, leading to the widening of the undistorted potential window. Given that this widened window encompasses the APAP's oxidation peak, it can be concluded that the detection of APAP will be minimally influenced by all the model interferents.

To verify our surface engineering rationale, the voltammograms of 10 μM -APAP solutions (in PBS) were obtained and compared with those of 10 μM -APAP solutions spiked with model interferents (within their physiological-relevant concentration). As shown in Fig. 5.9D,E, the measured voltammograms by the bare O-BDDE and H-BDDE illustrated that the oxidation peaks of APAP were buried and distorted after the introduction of the interferents, respectively. However, the use of the devised Nafion/H-BDDE led to a well-distinguishable APAP voltammetric response (as evident from the undistorted oxidation peak, Fig. 5.9F). To further validate the suitability of Nafion/H-BDDE for the selective detection of APAP, we characterized the interference of other endogenous electroactive species (within their physiological-relevant concentration range in biofluid, e.g., sweat). As shown in Fig. 5.10, the introduction of histidine, methionine, or ascorbic acid into the APAP solutions did not distort the oxidation response of APAP. Overall, the results from this comprehensive interference study are in agreement with our surface engineering rationale and illustrate the utility of the devised strategy.

The devised Nafion/H-BDDE interface can also be leveraged to mitigate biofouling, a critical constraint, overlooked by the previously reported wearable sensors, but widely investigated in the direct electroanalysis of conventional biofluids (e.g., blood). To illustrate the severity of this issue in our context, we characterized the biofouling effect occurring in the sweat matrix. We particularly used an iontophoretically-induced sweat sample, spiked with 10 μM of APAP, as a target medium.

Accordingly, first, the biofouling of a conventional carbon electrode (screen printed carbon electrode, SPCE) was characterized *via* tracking the changes to the voltammetric response in the sweat sample (measured repeatedly over time). Because each voltammetric scan consumes a negligible amount of analyte [59], the analyte amount in the sample stays the same, and thus, the sequentially recorded redox peak levels are expected to remain unchanged. As shown in Fig. 5.9G, although the SPCE-measured APAP oxidation presented an obvious peak in the buffer matrix, its voltammetric signal in the sweat matrix was merely a weak bump, which disappeared completely within 3 scans. This signal degradation can be attributed to the immediate and progressive adsorptions of the surface-active agents present in sweat, which inhibit the electron transfer of target electroactive molecules. Therefore, the observed rapid (3 scans performed over ~ 5 min) and total sensor response degradation illustrates that the sensing interface is unsuitable for the envisioned application.

Next, we repeated the same biofouling characterization procedure using a bare BDDE (specifically, H-BDDE, Fig. 5.9H). The results indicate the presence of biofouling-induced signal degradation, although occurring at a lower rate than the case of the SPCE (as evident from the distinguishable response after 5 repeated measurements). It is worth noting that the observed relatively low signal degradation rate is inline with one of our motivations for choosing the BDDE:

leveraging the BDDE's intrinsically high biofouling-resistance (due to the weak adsorption of polar molecules of its sp^3 -carbon structure) [66, 75]. Given that the biofouling-induced signal degradation needs to be further mitigated for reliable sensing, we investigated whether the anti-fouling effect of the Nafion membrane can be harnessed. Accordingly, we performed the same characterization study with a Nafion/H-BDDE (Fig. 5.9I), where minimal signal degradation was observed over the course of 8 consecutive measurements. The biofouling characterization results, collectively, indicate that the Nafion/H-BDDE presents considerable superior performance in comparison to the SPCE and H-BDDE (Fig. 5.9J) in terms of the preservation of the sensing fidelity in biofluid matrices.

The demonstrated APAP detection capabilities (in complex matrices) of the devised Nafion/H-BDDE sensing interface can be leveraged to reliably quantify APAP in non-invasively retrievable biofluids. To illustrate this point, we first used the Nafion/H-BDDE to monitor the voltammetric response of APAP in saliva and sweat samples, which were spiked with known amounts of APAP to construct samples with concentrations spanning from $1\mu\text{M}$ to $100\mu\text{M}$ (corresponding to the physiological relevant range). Specifically, the saliva samples were collected by passive drool, and the sweat samples were collected following the standard iontophoresis protocol [76], both from healthy human subjects without recent APAP administration histories. Figure 5.11A,B show the corresponding recorded voltammograms of the saliva and sweat samples. To extract the APAP oxidation peak information from the voltammograms, baseline estimation and correction were performed with the aid of a dedicated analytical framework (following the methodology above). For the case of both biofluids, a linear relationship between the measured/extracted voltammetric peak currents and the APAP concentration levels were observed (Fig. 5.11A,B, inset, $R^2 = 0.97$ and 0.99 for saliva and sweat measurements, respectively), with a

limit of detection of 1 μM . It is also noteworthy that the voltammograms recorded in both unspiked saliva and sweat samples do not exhibit any redox peak, demonstrating the minimal voltammetric influence of endogenous electroactive interferents (inline with our conclusions from the interference study).

To demonstrate the clinical utility of the sensing interface, the Nafion/H-BDDE was applied to track the temporal profile of circulating APAP in individuals taking APAP-based medication. Accordingly, following the aforementioned biofluid collection procedure, saliva and sweat samples were obtained from two subjects before and at intermittent time-points after their readily-scheduled medication administration (containing 650 mg APAP). The obtained saliva and sweat samples were analyzed by the Nafion/H-BDDE sensors and the corresponding voltammograms were processed with the aid of the analytical framework. Figure 5.11C,D show the post-calibrated concentration profiles of APAP in the saliva and sweat samples of the first subject (the corresponding results for subject 2 are shown in Fig. 5.12). Based on the sensor readouts, no APAP was detected in the saliva and sweat prior to medication intake, and a rapid increase, followed by a gradual elimination of APAP was observed upon intake (for both subjects). The captured trends are similar to the previously reported APAP pharmacokinetic profiles. Furthermore, the measured APAP concentrations in sweat and saliva samples were cross-validated via lab instrument measurements (using liquid chromatography with tandem mass spectrometry [77], LC-MS/MS). As shown in Fig. 5.11E,F, the sensor-estimated APAP concentrations closely matched the LC-MS/MS readouts ($R^2 = 0.92$ and 0.95 for saliva and sweat, respectively). These results, collectively, indicate that the devised voltammetric sensing interface can accurately measure APAP in non-invasively retrievable biofluids, and can be positioned to track the temporal profile of circulating APAP.

5.7. Voltammetric sensing solution for non-invasive pharmacokinetic monitoring

The demonstrated sensor's high accuracy in capturing the temporal profile of circulating APAP in sweat motivated the positioning of the sensor for pharmacokinetic monitoring applications. To this end, we developed and validated an integrated wearable solution to seamlessly measure the APAP's dynamic level in real-time (Fig. 5.13A). Accordingly, the engineered voltammetric sensor was integrated within a custom-developed smartwatch, which consists of 1) a microfluidic interface (consisting of sweat sampling and sensing chambers); 2) a Nafion/H-BDDE-based voltammetric sensing interface for APAP quantification; and 3) an electronic interface (Fig. 5.13B) for DPV-based signal excitation/acquisition, and data display/transmission (*via* a liquid-crystal display and a wireless Bluetooth module, respectively). To map the smartwatch-based readouts to the corresponding APAP concentration levels, the redox feature was extracted from the measured voltammograms by the dedicated analytical framework (similar to the ex-situ saliva and sweat study above).

Specifically, to enable efficient sweat sampling and real-time analysis, a skin-adhesive thin-film microfluidic interface was developed (constructed by vertical integration of tape-based layers with laser-cut patterns), which features low-volume sweat collection and sensing chambers [78]. To characterize the microfluidic interface's sweat sampling function, an assembled microfluidic device was placed on the iontophoretically-stimulated skin surface of a human subject (in which case, the sensor was replaced by a transparent plastic film to allow for visualization). As shown in Fig. 5.14, in this trial, the sensing chamber became fully filled in less than 3 min after the initiation of the sweat secretion, demonstrating the capability of the microfluidic interface to sample fresh sweat with minute-level temporal resolution.

To evaluate the devised solution's ability to track the dynamically-varying drug concentration levels, the sensor was embedded in the microfluidic sensing chamber and connected to a continuous flow system delivering APAP solutions with varying concentration levels (Fig. 5.13C, inset). Specifically, 10-, 50-, and 30- μ M APAP (in PBS) solutions were consecutively delivered, with the aid of a programmable syringe pump, at 1 μ L/min (similar level to the sweat secretion rate, induced by the standard iontophoresis procedure). To ensure high signal reproducibility in this setting, a cathodic electrical pulse (0.5 s, -0.4 V) was applied between the DPV scans (which has been shown to mitigate the potential carry-over effects in continuous measurements [79, 80]). As shown in Fig. 5.13C, the measured APAP peak current levels tracked the increase and subsequent decrease of the APAP concentration in the introduced solutions, and in all three concentration cases, stable peak current measurements were obtained.

The integrated wearable solution was then applied to seamlessly track the APAP's pharmacokinetic profile in sweat and investigate its sweat-saliva correlation. Accordingly, a volunteer subject with pre-scheduled APAP medication intake was recruited. To access sweat throughout the expected time window of the drug's circulation, standard iontophoresis was performed at intermittent time points, and after each stimulation, the sensing system was mounted on the stimulated area to perform in-situ sweat sampling and analysis. To assess sweat-saliva correlation, saliva samples were obtained intermittently during the experiment.

During the course of the sweat secretion, DPV scans were performed consecutively. The raw DPV readouts (by the circuit) and corresponding APAP oxidation peaks (extracted by the analytical framework) at four representative time points are shown in Fig. 5.13D. The collected saliva samples were analyzed in parallel using the developed sensors. The collective readouts are shown in Fig. 5.13E, which indicates that the captured APAP trend in sweat mirrors the trend in

saliva: both feature distinct absorption and elimination phases with similar temporal characteristics. To quantitatively compare these characteristics in sweat versus saliva, the captured concentration readouts were curve-fitted following the single-compartment model [81]:

$$c = A[e^{-K_{el}(t-t_0)} - e^{-K_a(t-t_0)}] \quad (3)$$

, where t is time after the oral administration of the APAP, t_0 is the lag time (with respect to the administration time, effectively the total lag time of oral administration→blood and blood→sweat/saliva drug partitioning), A is the pre-exponential factor, and K_{el} and K_a are the elimination and absorption rate constant, respectively (Fig. 5.13F). The extracted pharmacokinetic parameters in saliva are similar to the previously reported saliva-based analysis [82]. Moreover, the resemblance of the fitted pharmacokinetic profiles of sweat and saliva (fitted curve in Fig. 5.13E) and the similarity of their extracted parameters (tabulated in Fig. 5.13F) suggest a potentially high degree of sweat-saliva correlation. Given the readily established saliva-blood correlation of APAP, the results from our study support the potential clinical utility of sweat for non-invasive therapeutic drug monitoring.

5.8. Conclusion and discussion

In conclusion, first we presented the design space and operational settings for rendering electroactive drug readouts in a sample-to-answer manner. In that regard, the evaluation of carbon-based electrode candidates informed the suitability of boron-doped diamond electrode for the envisioned application, which followed by anodic treatment, was utilized to demonstrate nano- to sub/low-micro-molar level quantification of three model drugs (using DPV-based analysis). Furthermore, the characterization of the influence of the electroactive species present in epidermally-retrievable biofluids (including amino acids and uric acid) on the sensor response

allowed for the definition/identification of undistorted potential window(s) for the selective quantification of target electroactive molecules with oxidation peaks residing within the identified window(s). These findings were particularly lever-aged to render DP concentration readouts in iontophoretically-induced sweat samples using a coupled sensing system and analytical framework.

To further target drug outside the original “undistorted potential window”, we demonstrated surface-engineered voltammetric sensing interface for reliable electroactive drug analysis in biofluid matrices. Enabled by the devised interface, we presented a fully-integrated wearable solution for seamless therapeutic drug monitoring (targeting APAP as a model drug). We first performed interference and biofouling characterization studies to identify the key analytical constraints and guide our voltammetric sensor development efforts. In order to resolve the identified constraints, we devised a surface engineering strategy to selectively tune target/interference-surface interactions via: 1) modulating the intrinsic surface properties (by adjusting the surface termination) and 2) incorporating an extrinsic permselective membrane. By employing these orthogonal intrinsic/extrinsic surface treatment approaches, we realized a Nafion/H-BDDE sensing interface, which simultaneously mitigates biofouling and creates an undistorted potential window for APAP detection. Leveraging this interface, we demonstrated accurate APAP quantification in both sweat and saliva (cross-validated with lab-based assays, $R^2 \sim 0.94$).

To render seamless APAP readouts on-body, we integrated the engineered sensing interface into a custom-developed smartwatch, which was coupled with a dedicated analytical framework for voltammetric readout processing. By applying this solution in a human subject study, we captured the APAP’s pharmacokinetic profile in sweat and saliva. Of particular interest

is the similarity of the APAP's dynamic profile in both matrices (in terms of concentration level and absorption/elimination kinetics), suggesting a similar analyte partitioning mechanism from blood. These results inform the potential clinical utility of sweat as a therapeutic drug monitoring matrix, motivating further clinical investigations toward establishing its utility.

To the best of our knowledge, this study is the first demonstration of the pharmacokinetic correlation and significance of sweat readings, which was enabled by devising a thin microfluidic-based sensing system capable of rendering accurate and minute-level drug readouts in sweat. The presented surface engineering strategy can be adapted, with minimal reconfiguration, towards the quantification of a wide panel of electroactive endogenous and exogenous molecules. Toward expanding our drug monitoring capabilities, other sensing mechanisms (e.g., affinity-based) can also be explored to target non-electroactive drugs. It is noteworthy, targeting drugs with narrow therapeutic concentration windows are of particular clinical interest, because real-time monitoring can be harnessed to enable timely intervention and prevent adverse outcomes such as drug toxicity. To this end, the inclusion of auxiliary sensing interfaces to characterize the sweat-related matrices, such as sweat rate, sweat pH (with respect to the drug's dissociation constant, pK_a), and body hydration, can be helpful to account for the inter-/intra-individual drug partitioning variations. Furthermore, large-scale clinical studies need to be performed to construct the drugs' sweat-blood correlation and establish sweat-based pharmacokinetic profiles, in which case the application of data analytics techniques can be particularly useful to improve the accuracy of the drugs' proxy readouts. In that regard, the results from saliva-based studies can serve as suitable references to guide the engineering and clinical efforts.

The convergence of these efforts will establish a non-invasive and real-time therapeutic drug monitoring modality, which allows the collection of longitudinal patient-specific datasets at

large-scale. Harnessing these unprecedented capabilities can enable new patient-centric pharmacotherapy solutions (including drug compliance/abuse monitoring, personalized drug dosing, and feedback-controlled drug delivery), and can create new dimensions to direct drug and treatment development efforts.

5.9. Reference

1. K. Pavelić, S. K. Pavelić, M. Sedić, *Personalized Medicine*, 1–19, 2016.
2. M. E. G. Bigelow, *et al.*, *IEEE journal of translational engineering in health and medicine* **4**, 1–10, 2016.
3. J. L. Lenahan, *et al.*, *Journal of health communication* **18**, 31–39, 2013.
4. J.-H. Huang, *et al.*, *Drug design, development and therapy* **9**, 305, 2015.
5. J. Jonklaas, *et al.*, *Thyroid* **24**, 1670–1751, 2014.
6. D. E. Becker, *Anesthesia progress* **59**, 28–42, 2012.
7. W. Clarke, A. Dasgupta, *Clinical Challenges in Therapeutic Drug Monitoring: Special Populations, Physiological Conditions and Pharmacogenomics*, Elsevier, 2016.
8. N. Arroyo-Currás, *et al.*, *Proceedings of the National Academy of Sciences* **114**, 645–650, 2017.
9. P. L. Mage, *et al.*, *Nat. Biomed. Eng.* **1**, 70, 2017.
10. S. H. Jang, Z. Yan, J. A. Lazor, *Clinical Pharmacology & Therapeutics* **99**, 148–150, 2016.
11. T. Buclin, *et al.*, *Frontiers in Pharmacology* **11**, 177, 2020.
12. S. Cremers, N. Guha, B. Shine, *British journal of clinical pharmacology* **82**, 900, 2016.
13. W. Gao, *et al.*, *Nature* **529**, 509, 2016.

14. Y. Zhao, *et al.*, *Science advances* **6**, eaaz0007, 2020.
15. L. Tai, *et al.*, *Advanced Materials* **30**, 1707442, 2018.
16. S. Lin, *et al.*, *ACS sensors* **5**, 93–102, 2020.
17. Y. Yang, W. Gao, *Chemical Society Reviews* **48**, 1465–1491, 2019.
18. S. Emaminejad, *et al.*, *Proceedings of the National Academy of Sciences* **114**, 4625–4630, 2017.
19. J. Heikenfeld, *et al.*, *Nature biotechnology* **37**, 407–419, 2019.
20. A. Hauke, *et al.*, *Lab on a Chip* **18**, 3750–3759, 2018.
21. V. K. Gupta, R. Jain, K. Radhapyari, N. Jadon, S. Agarwal, *Analytical biochemistry* **408**, 179–196, 2011.
22. C. Jiang, *et al.*, *Chemical Reviews* **120**, 3852–3889, 2020.
23. W. Yantasee, *et al.*, *Environmental health perspectives* **115**, 1683–1690, 2007.
24. S. Suwal, A. Doyen, L. Bazinet, *Journal of membrane science* **496**, 267–283, 2015.
25. C. Rodriguez-Emmenegger, M. Houska, A. B. Alles, E. Brynda, *Macromolecular bioscience* **12**, 1413–1422, 2012.
26. J. P. Glynn, *Journal of Pharmacy and Pharmacology* **25**, 420–421, 1973.
27. D. T. Lowenthal, S. Oie, J. C. Van Stone, W. A. Briggs, G. Levy, *Journal of Pharmacology and Experimental Therapeutics* **196**, 570–578, 1976.
28. A. M. Larson, *et al.*, *Hepatology* **42**, 1364–1372, 2005.
29. M. A. Hedaya, *Basic Pharmacokinetics* **2**, 105–126, 2012.
30. Gupta, V. K.; Jain, R.; Radhapyari, K.; Jadon, N.; Agarwal, S. *Analytical biochemistry* **408**, 179–196, 2011.

31. Yang, N.; Yu, S.; Macpherson, J. V.; Einaga, Y.; Zhao, H.; Zhao, G.; Swain, G. M.; Jiang, X. *Chemical Society Reviews* **48**, 157–204, 2019.
32. Macpherson, J. V. *Physical Chemistry Chemical Physics* **17**, 2935–2949, 2019.
33. Benck, J. D.; Pinaud, B. A.; Gorlin, Y.; Jaramillo, T. F. *PloS one*, 9(10), e107942, 2014.
34. Hutton, L. A.; Iacobini, J. G.; Bitziou, E.; Channon, R. B.; Newton, M. E.; Macpherson, J. V. *Analytical chemistry* **85**, 7230–7240, 2014.
35. Xu, J.; Swain, G. M. *Analytical Chemistry* **70**, 1502–1510, 1998.
36. Švorc, L.; Tomčík, P.; Svítková, J.; Rievaj, M.; Bustin, D. *Food chemistry* **135**, 1198–1204, 2012.
37. Lourenção, B. C.; Medeiros, R. A.; Rocha-Filho, R. C.; Mazo, L. H.; Fatibello-Filho, O. *Talanta* **78**, 748–752, 2009.
38. Sarakhman, O.; Pysarevska, S.; Dubenska, L.; Stanković, D. M.; Otrísal, P.; Planková, A.; Kianičková, K.; Švorc, L. *Journal of The Electrochemical Society* **166**, B219–B226, 2019.
39. Schaper, W. *Cardiovascular drugs and therapy* **19**, 357–363, 2005.
40. Rao, G. H. R. *Stroke* **40**, 2271–2272, 2009.
41. Flint, R. B.; Mian, P.; van der Nagel, B.; Slijkhuis, N.; Koch, B. C. P. *Therapeutic drug monitoring* **39**, 164–171, 2017.
42. de Wildt, S. N.; Kerkvliet, K. T. M.; Wezenberg, M. G. A.; Ottink, S.; Hop, W. C. J.; Vulto, A. G.; van den Anker, J. N. *Therapeutic drug monitoring* **23**, 250–254, 2001.
43. Gal, P. *The Journal of Pediatric Pharmacology and Therapeutics* **12**, 212–215, 2007.
44. Hupert, M.; Muck, A.; Wang, J.; Stotter, J.; Cvackova, Z.; Haymond, S.; Show, Y.; Swain, G. M. *Diamond and Related Materials* **12**, 1940–1949, 2003.

45. Ivandini, T. A.; Rao, T. N.; Fujishima, A.; Einaga, Y. *Analytical chemistry* **78**, 3467–3471, 2006.
46. Wang, Q.; Vasilescu, A.; Subramanian, P.; Vezeanu, A.; Andrei, V.; Coffinier, Y.; Li, M.; Boukherroub, R.; Szunerits, S. *Electrochemistry communications* **35**, 84–87, 2013.
47. Chen, L.-C.; Chang, C.-C.; Chang, H.-C. *Electrochimica Acta* **53**, 2883–2889, 2003.
48. Enache, T. A.; Oliveira-Brett, A. M. *Bioelectrochemistry* **81**, 46–52, 2011.
49. Popa, E.; Kubota, Y.; Tryk, D. A.; Fujishima, A. *Analytical chemistry* **72**, 1724–1727, 2000.
50. Delgado-Povedano, M. M.; Calderón-Santiago, M.; Priego-Capote, F.; de Castro, M. D. L. *Talanta* **146**, 310–317, 2016.
51. Liappis, N.; Hungerland, H. *The American journal of clinical nutrition* **25**, 661–663, 1972.
52. Liappis, N.; Kelderbacher, S.-D.; Kessler, K.; Bantzer, P. *European journal of applied physiology and occupational physiology* **42**, 227–234, 1979.
53. Mark, H.; Harding, C. R. *International journal of cosmetic science* **35**, 163–168, 2013.
54. Huang, C.-T.; Chen, M.-L.; Huang, L.-L.; Mao, I.-F. *Chinese Journal of Physiology* **45**, 109–116, 2002.
55. Zhao, G.; Qi, Y.; Tian, Y. *Electroanalysis: An International Journal Devoted to Fundamental and Practical Aspects of Electroanalysis* **18**, 830–834, 2006.
56. Omanović, D.; Garnier, C.; Louis, Y.; Lenoble, V.; Mounier, S.; Pižeta, I. *Analytica Chimica Acta* **664**, 136–143, 2010.
57. Jakubowska, M. *Electroanalysis* **23**, 553–572, 2011.

58. A. J. Bard, L. R. Faulkner, J. Leddy, C. G. Zoski, *Electrochemical methods: fundamentals and applications* Wiley New York, 1980.
59. S. P. Kounaves, Voltammetric techniques. *Handbook of instrumental techniques for analytical chemistry*, 709–726, 1997.
60. S. Ranganathan, T.-C. Kuo, R. L. McCreery, *Analytical chemistry* **71**, 3574–3580, 1999.
61. L. Hu, *et al.*, *ACS applied materials & interfaces* **8**, 28872–28879, 2016.
62. K. Asai, T. A. Ivandini, M. M. Falah, Y. Einaga, *Electroanalysis* **28**, 177–182, 2016.
63. K. Asai, T. A. Ivandini, Y. Einaga, *Scientific reports* **6**, 32429, 2016.
64. E. Popa, H. Notsu, T. Miwa, D. A. Tryk, A. Fujishima, *Electrochemical and Solid State Letters* **2**, 49, 1998.
65. N. Yang, *et al.*, *Chemical Society Reviews* **48**, 157–204, 2019.
66. J. V Macpherson, *Physical Chemistry Chemical Physics* **17**, 2935–2949, 2015.
67. M. Hupert, *et al.*, *Diamond and Related Materials* **12**, 1940–1949, 2003.
68. K. Muzyka, *et al.*, *Analytical methods* **11**, 397–414, 2019.
69. K. Aoki, K. Tokuda, H. Matsuda, *Journal of electroanalytical chemistry and interfacial electrochemistry* **175**, 1–13, 1984.
70. A. P. P. Eisele, D. N. Clausen, C. R. T. Tarley, L. H. Dall’Antonia, E. R. Sartori, *Electroanalysis* **25**, 1734–1741, 2013.
71. A. M. Santos, F. C. Vicentini, P. B. Deroco, R. C. Rocha-Filho, O. Fatibello-Filho, *Journal of the Brazilian Chemical Society* **26**, 2159–2168, 2015.
72. V. Bernal, A. Erto, L. Giraldo, J. C. Moreno-Piraján, *Molecules* **22**, 1032, 2017.
73. J. Wang, R. P. Deo, S. Thongngamdee, B. Ogorevc, *Electroanalysis* **13**, 1153–1156, 2001.

74. B. Hoyer, T. M. Florence, G. E. Batley, *Analytical chemistry* **59**, 1608–1614, 1987.
75. Y. Huang, A. Hara, C. Terashima, A. Fujishima, M. Takai, *Carbon* **152**, 354–362, 2019.
76. V. A. LeGrys, *Sweat testing: sample collection and quantitative analysis: approved guideline* NCCLS, 1994.
77. W. Lu, S. Zhao, M. Gong, L. Sun, L. Ding, *Journal of pharmaceutical analysis* **8**, 160–167, 2018.
78. H. Lin, *et al.*, *Lab on a Chip* **19**, 2844–2853, 2019.
79. G. Ogata, *et al.*, *Nature biomedical engineering* **1**, 654–666, 2017.
80. R. Kiran, E. Scorsone, P. Mailley, P. Bergonzo, *Analytical chemistry* **84**, 10207–10213, 2012.
81. M. A. Hedaya, *Basic Pharmacokinetics* **2**, 105–126, 2012.
82. M. T. Borin, J. W. Ayres, *International journal of pharmaceutics* **54**, 199–209, 1989.

Chapter 6. Wearable microneedle-based electrochemical aptamer biosensing for precision dosing of drugs with narrow therapeutic windows

6.1. Introduction

To realize precision personalized medicine and effective pharmacotherapy, the right drug needs to be delivered to the right patient at the right dose. In that regard, appropriate dosing for pharmaceuticals that present narrow therapeutic windows, such as antibiotics, is particularly challenging. In such cases, the high inter-/intra-subject variations—stemming from influential factors including kidney/liver function, tissue penetration, and drug-drug interactions—may often cause the drug level to fall outside the optimal therapeutic window. This can lead to adverse outcomes, such as kidney injury, and ineffective pharmacotherapy.

To circumvent such issues, patients who are prescribed these medications undergo therapeutic drug monitoring (TDM) sessions. At present, standard practices for conducting TDM involve invasive blood draws, followed by labor-intensive and high-cost lab-based analysis (e.g., chromatography, immunoassay) to capture the drug circulating level at one or two timepoint(s) (Fig. 6.1A) [1]. These limitations severely compromise the utility of TDM for optimal dosing in many aspects. Firstly, the turnaround times for results are prolonged (~24 h), and thus, inadequate to allow for timely intervention. Secondly, the poor temporal resolution of the measurements (mostly confined to a single trough level measurement) inherently limit the accuracy of the current TDM approaches in terms of predicting the drug's highly complex pharmacokinetic (PK) characteristics (e.g., area-under-the-curve [AUC]) [2]. Thirdly, because of their limited accessibility, TDM sessions are conducted at sub-optimal rates over the course of treatment, and subsequently fail to capture longitudinal variations in the drug's PK characteristics. This

shortcoming is particularly critical for antibiotics-based treatments, where the antibiotic itself or the co-administered drugs can affect the drug clearance (e.g., due to the changes they make to renal function) [3]. Also applicable to antibiotics-based treatments, these acknowledged challenges contribute to emerging antibiotic resistance: not only because of inadequate dosing, but also because of avoiding the use of the best choice of antibiotic due to the need for TDM and the fears for inducing toxicities [4].

Wearable biosensors targeting non-/minimally-invasively accessible biofluids can in principle address the limitations encountered in current TDM practices by enabling the seamless, continuous, and real-time measurement of the drug levels [5-9] (Fig. 6.1B). To this end, probing interstitial fluid (ISF) is a viable approach. A wide panel of pharmaceuticals partition into ISF with high correlation to their circulating blood levels, many of which may not diffuse into other accessible biofluids such as sweat and saliva [10]. Furthermore, probing ISF could be advantageous in the context of antibiotics-based treatments, given that the ISF compartment is often the intended site for drug activity, as it is in this space where many bacterial infections start and progress. In such cases, the ISF-based measurements may provide a more direct insight as compared to the blood-based counterpart [11].

The molecular information in the ISF can be minimally-invasively retrieved with the aid of microneedle devices. These devices possess sharp, mechanically robust, and short needle-like features that enable easy and fracture-free skin penetration with no/minimal pain. By coupling electrochemical sensing capability with the microneedle's skin piercing functionality, microneedle devices can be adapted for the sample-to-answer quantification of ISF analytes in-situ [6, 12-14]. However, the demonstrated microneedle-based electrochemical sensors rely on enzymes or

ionophores for analyte recognition, excluding a wide variety of drug molecules for which these recognition elements are not available.

In that regard, the use of aptamers, as artificially-engineered recognition elements, can greatly expand the library of detectable analytes [15]. By immobilizing redox signal reporter-coupled aptamer molecules onto the surface of an electrode, an electrochemical aptamer biosensor (EAB) can be formed—which reversibly and in real-time transduces aptamer-target bindings into an electrically measurable signal. Several EABs have been developed and adapted for the measurement of antibiotics in blood, illustrating the utility of this class of biosensors for complex biofluid analysis [16-18]. Yet EABs have not been leveraged for in-situ ISF biomonitoring, since their fabrication onto microneedle devices is non-trivial. To elaborate, for robust EAB-based sensing, a high-quality surface (e.g., gold) is needed to ensure the strong covalent binding of the aptamer molecules (typically with the aid of an intermediary thiol group) and the efficient retrieval of the transduced signal [19]. Previously reported sensor-on-microneedle fabrication and integration schemes cannot simultaneously satisfy these sensor-level electrochemical constraints and the device-level structural/mechanical constraints (imposed by skin penetration requirements) [20]. Specifically, the demonstrated microneedle-based sensing devices are limited by their substrates' impurity and high surface roughness. Furthermore, they are mostly fabricated following complex and costly fabrication schemes.

Overcoming these limitations, here, we present a simple and low-cost EAB-on-microneedle fabrication scheme to develop a microneedle-based EAB patch (“ μ NEAB-patch”) for in-situ ISF biomonitoring (Fig. 6.1C). Our fabrication scheme centers on engineering a gold nanoparticle (AuNP) coating via a single deposition step, which uniquely transforms the surface of a clinical-grade needle into a high-quality gold working electrode substrate for strong aptamer

immobilization and efficient redox signal retrieval. Following this scheme, the sensing interfaces are built on the tip of shortened acupuncture gold needles, allowing to simultaneously leverage the needles' high sharpness for skin penetration and conductivity for signal routing. Illustrating the generalizability of our approach, we developed multiple μ NEABs targeting antibiotics (tobramycin and vancomycin) as well as other drugs (doxorubicin: an anticancer drug; thrombin: a procoagulant and anticoagulant). The antibiotic choice was motivated by noting their high rate of treatment-induced kidney injuries (tobramycin: 12% [21]; vancomycin: 24% [22]), which can be effectively mitigated via advanced TDM solutions [2].

Our characterization results indicate that the developed μ NEABs present a high level of sensitivity and stability (comparable to EABs developed on standard gold electrodes), while being suitable for intradermal applications. The in-vivo animal studies—which were performed with the tobramycin μ NEAB-patch on a rat model—revealed the high correlation of blood-ISF readings and the potential of real-time continuous ISF measurements for early prediction of critical circulating PK parameters that are commonly used to guide dosing (Fig. 6.1D). By reducing the feedback time for dosage adjustment from ~24 hours to minutes and obviating cumbersome and costly sample collection/analysis, our device serves as a viable, yet accessible TDM solution to maximize safety and optimize pharmacotherapy outcomes.

6.2. Experimental Section

6.2.1. Materials and Reagents

All reagents were purchased from Sigma-Aldrich (MO, USA) unless stated. Tris(2-carboxyethyl)phosphine hydrochloride (TCEP) was purchased from TCI America, Inc. (OR, USA). The human α -thrombin was purchased from Haematologic Technologies, Inc. (VT, USA).

Tobramycin (900 $\mu\text{g}/\text{mg}$) and phosphate buffered saline (1 \times , Gibco PBS, pH 7.2) were purchased from Thermo Scientific (MA, USA). Tobramycin and vancomycin aptamers were purchased from Integrated DNA Technologies (IA, USA) and doxorubicin and thrombin aptamers were purchased from Biosearch Technologies, Inc. (CA, USA). PDMS (Sylgard 184 Silicone Elastomer) was purchased from Dow Corning (MI, USA). Gold-plated acupuncture needles were purchased from Suzhou Acupuncture & Moxibustion Appliance Co., Ltd (Suzhou, China). The lancets (30 gauge) were purchased from CVS pharmacy (RI, USA). Disc gold electrodes were purchased from Bioanalytical Systems, Inc. (IN, USA). Silver-silver chloride (Ag/AgCl) ink was purchased from Ercon Incorporated (MA, USA).

6.2.2. μNEAB -patch fabrication

The μNEAB -patch consists of three repurposed microneedle electrodes, a PDMS substrate, and a 3D-printed case (as the housing of the μNEAB -patch). The PDMS substrate was fabricated by mixing the base and the curing agent at a 10:1 ratio. The mixture was subsequently poured into a petri dish (thickness: ~ 3 mm) and cured at 70 $^{\circ}\text{C}$ for 5 h. The cured PDMS was then cut and embedded within the cylindrical 3D-printed case (diameter: 6 mm, height: 5 mm). The solid needles were inserted into the PDMS substrate with the aid of a custom-designed mold to form microneedle electrodes (exposed tip length: ~ 1 mm). The microneedle electrodes were wired from the distal ends of the needles and the whole device was sealed by epoxy.

The working and counter electrodes were constructed using gold-plated acupuncture needles. The needles were cleaned by sonication in ethanol followed by deionized (DI) water (5 min for each solvent). To form an AuNP-microneedle, the microneedle electrode was immersed in a stirring solution containing 1.2 mg/mL chloroauric acid (HAuCl_4), 0.1 M sodium chloride

(NaCl), and 1.5 wt.% hydrochloric acid (HCl). A pulsed waveform of 0 V and -0.4 V (versus Ag/AgCl) was applied for 120 cycles (one cycle: 1 s for each potential) to form an AuNP coating [24]. An uncoated Au-microneedle was directly used as a counter electrode. The reference electrode was constructed by dip-coating a lancet with Ag/AgCl ink (1:1 diluted in toluene) before inserting into the PDMS substrate.

6.2.3. Characterization of microneedle electrode surface morphologies and chemical compositions

The Au-microneedle and AuNP-microneedle morphologies were characterized by SEM (ZEISS Supra 40VP). Surface chemical compositions were characterized by EDS (Thermo Noran System 6).

6.2.4. DNA aptamer sequences.

The sequence of the aptamer probes used in the experiments are listed below:

Tobramycin:

5'-/5ThioMC6-D/GGGACTTGGTTTAGGTAATGAGTCCC/3MeBIN/-3' [23];

Vancomycin:

5'-/5ThioMC6-D/CGAGGGTACCGCAATAGTACTTATTGTTCGCCTATTGTGGGTCGG/3MeBIN/-3' [18];

Doxorubicin:

5'-/5ThioMC6-D/ACCATCTGTGTAAGGGGTAAGGGGTGGT/3MeBIN/-3' [25];

Thrombin:

5'-/5ThioMC6-D/TAAGTTCATCTCCCCGGTTGGTGTGGTTGGT/3MeBIN/-3' [26].

6.2.5. EAB fabrication

To fabricate EABs, a 5 μL aliquot of the 100 μM aptamer stock solution was thawed to room temperature and then reduced for 1 hour in the dark with 10 μL of TCEP solution. The TCEP solution was prepared in a Tris buffer solution containing 100 mM Tris hydrochloride, 140 mM NaCl, 20 mM magnesium chloride (MgCl_2), and 20 mM potassium chloride (KCl). 100 mM TCEP was used to fabricate doxorubicin EABs while other EABs were fabricated with 10 mM TCEP (to achieve a lower probe density in the fabricated EABs). The TCEP-reduced aptamer was then diluted in 500 μL PBS. To construct aptamer sensors on disc gold electrodes, the electrodes were electrochemically-cleaned following the previously reported method (24). The cleaned disc electrodes or the freshly-prepared microneedle electrodes were immersed in aptamer solution for 2 h at room temperature in the dark. Following this, the sensors were immersed overnight at room temperature in 20 mM 6-mercapto-1-hexanol (prepared in PBS) to coat the remaining gold surface and to remove non-specifically adsorbed aptamers. After this, the sensors were rinsed with DI water and stored in the artificial ISF buffer solution.

6.2.6. Ex-vivo μNEAB characterization.

All the electrochemical measurements were performed using a CHI660E or a CHI1040C electrochemical workstation (CH Instruments, Inc.). The ex-situ sensor characterizations were performed in an electrochemical cell (reference electrode: Ag/AgCl, counter electrode: platinum) containing artificial ISF buffer solution. The artificial ISF solution was prepared according to the previously reported composition [27]. Here, 6.3 g NaCl (107.7 mM), 0.26 g KCl (3.5 mM), 0.17 g calcium chloride (CaCl_2 , 1.5 mM), 0.17 g magnesium sulfate (MgSO_4 , 0.7 mM), 2.2 g sodium bicarbonate (NaHCO_3 , 26.2 mM), 0.26 g monosodium phosphate (NaH_2PO_4 , 1.7 mM), and 2.1 g

sodium gluconate (9.6 mM) were mixed in 1 L DI water and the pH was adjusted to 7.4. All sensors were interrogated using square wave voltammetry (SWV) with a frequency of 200 Hz, a pulse amplitude of 25 mV, and a voltage increment of 1 mV. The acquired voltammograms were processed using Matlab (MathWorks, MA, USA) to extract the MB redox peak current (similar to the previous-reported method [28]).

To construct phantom gels, 1.4 wt.% agarose powder [9] was mixed with artificial ISF solutions (containing tobramycin with various levels) and placed in an 80 °C water bath. After agarose was completely dissolved, the solutions were cooled to room temperature to form phantom gels. The fabricated μ NEAB-patch was inserted into the phantom gels and the sensor was interrogated continuously (with the interrogation paused during μ NEAB-patch transfer). To test the sensor drift in an ex-situ setting, The μ NEAB were inserted into an excised porcine skin (Stellen Medical, MN, USA) and the biosensor readouts were monitored continuously. The skin was placed at the bottom of a beaker containing artificial ISF solution to prevent dehydration. The skin insertion test was performed by placing the μ NEABs into an excised porcine skin followed by an immediate withdrawal (serving as one insertion). The biosensors' responses to tobramycin were tested in an electrochemical cell (containing artificial ISF buffer solution) before and after skin insertions.

6.2.7. Skin penetration efficiency test

The penetration test was performed on the rat skin immediately after the euthanasia of the animal (the carcass was donated by the Division of Laboratory Animal Medicine at University of California, Los Angeles under a tissue sharing program to reduce the number of animals used). The hair on the lower back was removed by a depilation (Nair, Church & Dwight, NJ, USA) before

the microneedle test was administered. The skin was penetrated multiple times with the developed microneedle, harvested, and fixed in 10% formalin (48 h). The fixed skin was paraffin embedded and sectioned. Sections (4 μm in thickness) were collected every 20 μm throughout the sample and stained with H&E.

6.2.8. In-vitro biocompatibility test

The cell toxicity test was performed using human dermal fibroblasts (isolated in Dr. Collier's Lab). The fabricated needle-based working, reference, and counter electrodes were separately incubated in three vials of Dulbecco's Modified Eagle Medium (DMEM, Thermo Scientific) in a CO₂ incubator (1, 4, and 8 hours). After the incubation, the electrodes were removed, the resultant DMEM was mixed with serum (up to 10% FBS) and the cells, and the mixture was plated. The plated cells were incubated at 37 °C in 5% CO₂ atmosphere (24 hours). After the incubation, all cells on the plate were collected by trypsinization. Cell viability was determined by trypan blue stain using the hemocytometer.

6.2.9. In-vivo μNEAB -patch characterization on a rat model

The animal study protocol was reviewed and approved by the Institutional Animal Care and Use Committee (IACUC) at University of California, Los Angeles. Three adult female Sprague Dawley rats were purchased from Charles River Laboratories (weight at the point of experiment: 300-400 g). Rats were housed in the facility (1 or 2 rats per cage) with controlled temperature and humidity on a 12 h light-dark cycle with food and water available ad libitum throughout the studies. A minimal seven-day acclimate time was provided before any procedure was implemented.

In the drug monitoring experiment, the rat was under isoflurane anesthesia (1.5% - 2%) with a circulating heating pad to maintain its body temperature at ~ 37 °C. A peripheral venous catheter was placed into the tail vein right after anesthesia to facilitate intravenous drug injection. A μ NEAB-patch was applied onto the rat's lower back (with hair removed) and a Tegaderm film (3M, MN, USA) was used to secure the device in place. The μ NEAB-patch was connected to a potentiostat to provide real-time readouts. The biosensor was interrogated using the same method and parameters as the ex-vivo experiments (with ~ 30 s interval between measurements). The biosensor baseline was monitored for at least 1 h before drug injection. Venous blood was collected from the tail vein or the lateral saphenous vein before and at intermittent time points after drug injection. Blood was left undisturbed at room temperature for 15 min, and then centrifuged at 10,000 rpm for 10 min. The supernatant (serum) was stored at -20 °C before analysis. To administer the drug, the tobramycin stock solution (40 mg/mL, Baxter International, IL, USA) was diluted with saline (Hospira, IL, USA) to a final volume of ~ 1 mL and slowly injected into the vein via the catheter.

6.2.10. Data analysis for in-vivo experiments

In-vivo experiment data was analyzed using Matlab. First, the MB redox peak currents were extracted from recorded voltammograms using the same method as the ex-vivo experiments. Continuous sensor readout $I_{measure}(t)$ was subsequently constructed. To correct for the sensor baseline drift, a hypothetical baseline $I_{baseline}(t)$ was constructed using an exponential equation (previously used to describe the EAB signal drift pattern in biofluid [29]). The baseline was fitted using the pre-injection sensor readouts, while ensuring all the post-injection readouts were above the fitted baseline. The ISF sensing signal $s(t)$ was defined as:

$$s(t) = \frac{I_{measure}(t) - I_{baseline}(t)}{I_{baseline}(t)} \times 100\% \quad (1)$$

6.2.11. Pharmacokinetic analysis

The pharmacokinetic analysis was performed based on the two-compartment pharmacokinetic model [30]. Accordingly, the ISF sensing signal was fitted using a bi-exponential equation derived from the model:

$$C_{ISF} = X[e^{-\beta t} - e^{-\alpha t}] \quad (2)$$

, where α and β are related to the distribution and elimination rates, respectively, and X is the pre-exponential factor. Due to the limited number of blood samples acquired per trial, the blood concentration versus time curve was fitted using a simplified exponential equation to avoid overfitting:

$$C_{blood} = Y e^{-\gamma t} \quad (3)$$

, where γ is predominantly determined by the drug elimination rate and Y is the pre-exponential factor. The AUC and R_{max} information were extracted from the fitted pharmacokinetic profiles.

6.2.12. Tobramycin quantification with LC-MS/MS

The tobramycin concentrations in the rat serum were quantified using LC-MS/MS with a multiple reaction monitoring (MRM) technique [23]. Sisomicin sulfate was used as the internal standard (IS). For calibration, tobramycin stock solution was prepared in DI water at a concentration of 1 mg/mL. The stock solution was further diluted with DI water to obtain calibration standards at 0, 100, 200, 500, 1000, and 1500 ng/mL. The IS stock solution was prepared in DI water at a concentration of 1 mg/mL and was further diluted with water to 10

µg/mL. 5 µL of the rat serum samples was first diluted into 445 µL of DI water. 50 µL of 10 µg/mL IS was then spiked into 450 µL of calibration standards or diluted serum samples (to reach a final IS concentration of 1 µg/mL). The resultant samples were mixed and vortexed with 500 µL acetonitrile, followed by centrifugation at 14,800 rpm for 10 min. 1 mL of the supernatant was mixed and vortexed with 500 µL of dichloromethane, followed by centrifugation at 14,800 rpm for 10 min. Then, 400 µL of the new supernatant was mixed and vortexed with 400 µL of DI water, followed by centrifugation at 14,800 rpm for 10 min. Finally, 100 µL of the supernatant was transferred into an autosampler vial for tobramycin quantification.

For HPLC analysis, Agilent 1200 series HPLC (Agilent Technologies, CA, USA) equipped with HTS PAL autosampler (CTC Analytics, MN, USA) was coupled to an API 4000 triple quadrupole mass spectrometer (Sciex, ON, Canada) for MRM experiments. Chromatographic separation was realized by the Zorbax 300 SB-C18 column (0.5 ID × 150 mm L, 5 µm, Agilent Technologies, CA, USA). The mobile phases A and B were water and acetonitrile respectively, both mixed with 10 mM heptafluorobutyric acid (HFBA). The flow rate was set at 400 µL/min with 3 minutes of equilibrium time. The gradient starts with increasing B from 5% to 90% in 4 minutes (0-4 min), then maintaining 90% B for 4 minutes (4-8 min), followed by decreasing B from 90% to 5% in 1 minute (8-9 min), and finally maintaining 5% B for 3 minutes (9-12 min). Sample vials were maintained at 4 °C in the autosampler tray. 20 µL of sample was loaded onto the column each time. The tandem mass spectrometry was operated in MRM mode recording the following *m/z* transitions: 468.4 → 163.2 for tobramycin and 448.3 → 160.2 for sisomicin. The declustering potential, entrance potential, collision energy, and collision cell exit potential were optimized at 86 V, 10 V, 35 V, and 10 V for tobramycin and 76 V, 10 V, 29 V, and 10 V for sisomicin.

6.3. Development of μ NEABs

To construct the μ NEAB-patch, we first fabricated microneedle electrodes by affixing clinical-grade acupuncture needles within a flexible polydimethylsiloxane (PDMS) substrate. This configuration leverages the needles' robustness and sharpness to reliably and painlessly pierce the stratum corneum layer of the skin, making it suitable for accessing dermal ISF analytes [31]. To render real-time and continuous sensing, pharmaceutical-targeting aptamers are immobilized onto the microneedle electrode surface. The distal ends of the aptamers are tagged with redox-active molecules (methylene blue, MB) as signal reporters. The aptamers undergo conformational changes upon binding to the target pharmaceutical, altering the charge transfer rate between the signal reporter and electrode surface, which can be measured via voltammetry-based approaches.

As a key fabrication step of the μ NEAB-patch, we specifically engineered a low-cost AuNP-coated gold microneedle surface (denoted as AuNP-microneedle) to serve as the biosensor substrate. This coating is critical to the EAB construction and signal transduction as it renders a high-quality surface to simultaneously enable strong aptamer binding (via a self-assembled thiol group) and reliable redox signal retrieval (given its exceptional electrochemical properties).

The surface chemistry of the AuNP-microneedle was first characterized and compared with that of the uncoated microneedle substrate (denoted as Au-microneedle). As shown in the scanning electron microscopy-energy dispersive spectroscopy (SEM-EDS, Fig. 6.2A), a high level of nickel (Ni) impurity was identified on an Au-microneedle surface, while the AuNP coating effectively suppressed the Ni-associated peaks. Eliminating the Ni exposure is important, because its poor electrochemical performance and associated surface oxide layer can impede the MB signal retrieval and the aptamer immobilization. To further verify this point, representative tobramycin μ NEABs were constructed on both substrates and the biosensors' voltammetric readouts were

recorded in a custom developed artificial ISF buffer environment. As shown in Fig. 6.2B(ii), for an AuNP-coated μ NEAB, a well-defined MB reduction peak with a flat baseline was observed, indicating the formation of a compact self-assembled monolayer [32]. However, for the uncoated case, the voltammetric peak of the signal reporter is hardly differentiated from the background (Fig. 6.2B(i)). The AuNP coating is also advantageous for rendering a large effective surface area, increasing the number of immobilized aptamers on the electrode, and subsequently enhancing the signal current and the measurement precision [33] (Fig. 6.3).

To illustrate the generalizability of our approach, we developed additional microneedle-based EABs (targeting, vancomycin, doxorubicin, and thrombin; in addition to tobramycin) by immobilizing the corresponding aptamers on the AuNP-microneedle substrates. As shown in Fig. 6.2C,D and Fig. 6.4, for all four cases, the corresponding biosensor responses and analyte concentrations present a monotonic relationship with minimal inter-device variations.

Aligned with our aforementioned motivation of tobramycin PK monitoring, in the subsequent characterization experiments, we primarily focused on tobramycin sensing. Accordingly, we first compared the performance of the tobramycin μ NEAB with the tobramycin-EAB constructed on a standard gold disc electrode and found that the two possess similar sensitivity levels (Fig. 6.2C).

Furthermore, we characterized the tobramycin μ NEAB from the standpoint of long-term stability and reproducibility. To investigate the biosensor's long-term stability, we recorded its baseline readout in an artificial ISF buffer under two extreme scenarios: repeated interrogation (1000 scans) and extended operation time (> 15 h). In both scenarios, the biosensor readouts presented insignificant drift (< 10%, Fig. 6.2E), indicating that both the electrochemically-driven and time-dependent desorption of the self-assembled monolayer were minimal. Our

characterization of different batches of the tobramycin μ NEABs yielded minimal inter-/intra-batch response variations, demonstrating the high reproducibility of the biosensor fabrication scheme (Fig. 6.2F).

6.4. Ex-vivo μ NEAB-patch characterization

Toward translation into in-vivo biomonitoring, we extended our device characterization by using ex-situ models that mimic the envisioned intradermal ISF biosensing scenario.

To evaluate the biosensor's continuous response, we utilized a phantom gel setup and the complete μ NEAB-patch (consisting of the tobramycin aptamer-immobilized working electrode, a silver/silver chloride [Ag/AgCl] reference electrode, and a gold counter electrode, all microneedle-based). We specifically used three test gels pre-spiked with different tobramycin concentrations, collectively representing the analyte concentration variations in dermal ISF. We rotated through these test gels and recorded the response of the μ NEAB-patch continuously (with the device being inserted in the gels). As shown in Fig. 6.5A, the μ NEAB produced rapid (< 1 min) as well as highly stable and reversible responses to tobramycin, demonstrating its high suitability for continuous ISF biomonitoring.

Furthermore, we characterized the μ NEAB performance in terms of its biofouling resistance. Biofouling is a major challenge for in-vivo biosensing as it can render biosensors (including EABs) unusable within a short period of time. For this characterization, we utilized two methods. The first method was based on characterizing the sensor response in a tissue environment, which was performed by inserting the device into a piece of excised porcine skin, followed by continuously recording the biosensor readouts. Figure 6.5B(i) shows that the in-skin measurements stayed within 70% of the initial measurement values for over 5 h of operation

(comparable to previously reported results in a similar context [34]). Furthermore, comparison of the biosensor's response to tobramycin (10 μM) before versus after the biofouling test revealed a minimal impact to the biosensor function (Fig. 6.5B(ii)). The second method was based on characterizing the biosensor response in a protein-spiked buffer solution (with the protein concentration being within the concentration range of common proteins in the ISF [35]). In this setting, the sensor exhibited smaller drift over an extended time window (> 13 h, Fig. 6.6). Collectively, the biofouling characterization results suggest that our biosensor would function properly within the envisioned measurement time window (corresponding to the drug's time-excursion in the circulation). To further minimize drift, follow-up investigations would be needed to identify the sources of the drift and mitigate their confounding effects.

Additionally, we evaluated the influence of insertion-induced disruptions to the biosensor performance. Previous studies performed with microneedle-based biosensors (used for ISF sampling/off-body analysis) indicated a significant loss of their immobilized sensing layer upon insertion into the epidermis [36]. To characterize this effect in our context, we measured and compared the biosensor response to tobramycin (10 μM) before and after repetitive insertions into a piece of porcine skin. As shown in Fig. 6.5C, the response remained relatively constant ($< 10\%$ variations), indicating the robustness of the coated/immobilized layers against insertion-induced disruptions.

Moreover, we investigated the μNEAB -patch's skin penetration capability and biocompatibility. Figure 6.5D show the hematoxylin and eosin (H&E) stained rat skin tissue after microneedle insertion, confirming that the developed microneedle device penetrated the epidermis and accessed the dermal layer of the skin (insertion depth ~ 200 μm). To evaluate the biocompatibility of the μNEAB -patch, the human dermal fibroblasts (HDFs) were cultured in the

presence of the μ NEAB-patch's individual electrodes. As shown in Fig. 6.5E, for all the culturing times and across all the electrodes, no obvious cell viability change was observed, suggesting that cell toxicity would be negligible for both short- and relatively long-term device operation.

6.5. In-vivo μ NEAB-patch characterization in a rat model

The developed μ NEAB-patch was then deployed in animal studies to monitor the PK profile of tobramycin in dermal ISF and investigate the drug's ISF-blood correlation. These experiments were performed on three healthy adult Sprague-Dawley rats. For these experiments, tobramycin was administered intravenously, while the rats were anesthetized, with the patch applied on their dorsal skin (Fig. 6.7A). Figure 6.8 shows no visible patch-induced bleeding as well as the rapid skin recovery upon the patch removal, reaffirming the minimally-invasive nature of the developed technology.

To investigate the drug's ISF-blood correlation, blood samples were simultaneously collected before and at intermittent time points after the drug injection, and then analyzed by the standard lab instrument (liquid chromatography with tandem mass spectrometry, LC-MS/MS). The ISF PK measurements were interpreted with the aid of a two-compartment pharmacokinetic model that accounts for the drug distribution (from blood to ISF) and elimination (Fig. 6.7B). We investigated the relationship between the drug's circulating AUC (AUC_{blood}) and the processed μ NEAB-patch readouts—specifically, the area under the curve (AUC_{ISF}) and the maximal value of the sensor responses (R_{max}). The choice of AUC_{blood} was motivated by its common use (as a standard measure of total drug exposure) to guide dosing [37].

We first assessed the μ NEAB-patch's core capability of tracking the ISF PK profile in-vivo. As shown in Fig. 6.9A, upon a bolus tobramycin injection (20 mg/kg), a rapid increase,

followed by a gradual decrease in sensor readout was observed, corresponding to the drug's distribution and redistribution/elimination phases. In a separate control experiment, the injection of a similar amount of saline did not induce noticeable changes to the sensor readout (Fig. 6.9B).

Next, we extended the study to investigate the drug's PK characteristics in relation to the administered drug dosages. For each rat, we performed the associated experiments with at least one week interval to avoid carryover effects. As shown in Fig. 6.7C,D (for rat A) and Fig. 6.10 (for rat B), both R_{\max} and AUC_{ISF} increased with the increase of drug dosages. This trend was also reflected by the AUC_{blood} .

Figure 6.7E tabulates the collective results obtained from a total of eight independent trials (performed on three rats). It should be noted that for the same animal, neither the blood-based nor the ISF-based drug measurements were linearly proportional to the correspondingly administered dosage. Furthermore, the animals' response to the same injection dosage (e.g., 20 mg/kg) varied significantly (AUC_{blood} : $176 \pm 116 \mu\text{M} \cdot \text{h}$; AUC_{ISF} : $7.7 \pm 5.2 \% \cdot \text{h}$). These observations indicate high degrees of inter-/intra-subject variations (inline with previously reported blood-based results [38]), which can be attributed to variations in the rats' underlying physiological conditions (e.g., renal function, weight, diet) [3, 39].

Encouragingly, despite these variations, the μNEAB -patch-generated ISF readouts captured the circulating pharmacokinetic characteristics reliably. Figure 6.7F shows the high level of correlation between AUC_{blood} and AUC_{ISF} ($R^2 = 0.99$) as well as AUC_{blood} and R_{\max} ($R^2 = 0.97$). These results suggest that the real-time continuous ISF readings rendered by our μNEAB -patch can be leveraged to predict the subject's total drug exposure for precision dosing. Specifically, when the maximum response value is used, the feedback time can be reduced to ~ 15 min (for the

case of a rat), providing the possibility of finetuning the dosage (within the intended therapeutic window) and/or the time interval to next dosing administration.

6.6. Discussion

The ex-vivo and in-vivo characterization results comprehensively support the suitability of the μ NEAB-patch for tracking the drug's pharmacokinetics minimally-invasively and in real time. The continuous ISF analyte readouts rendered by this patch revealed the high correlation of AUC_{ISF} and R_{max} with respect to the animal's total drug exposure. These results demonstrate the potential clinical utility of our solution for precision dosing. In particular, the use of R_{max} , as an indicator of drug exposure, could be of tremendous value. It reduces the time for extracting the drug's circulating pharmacokinetics from several hours (time-to-trough: ~ 12 h; sample analysis: ~ 6 -12 h) to minutes. In this way, the presented technology uniquely enables timely feedback for dosage adjustment and other interventions such as extending the time interval for dosing. This will effectively maximize the treatment efficacy, while minimizing toxicities and adverse effects. It is also worth highlighting the large inter-/intra-subject variations observed in the antibiotics' circulating pharmacokinetics (similar to previous findings). These observations further emphasize the pressing need for performing TDM at a higher frequency and with an improved accuracy, aligned with the possibilities offered by our technology.

Toward translating this technology into clinical settings, dedicated engineering and clinical efforts are needed. The technology could particularly benefit from surface engineering methods [34], differential/auxiliary measurement techniques [16], and corrective algorithms that minimize error caused by ISF-specific confounding factors (e.g., biofouling-induced drift within a tissue environment). Furthermore, standard microneedle sensor calibration methodologies are needed to

benchmark the biosensor performance in the ISF environment. To this end, the findings from recently introduced ISF analyte sampling/analysis techniques are insightful and have formed a solid foundation for building such methodologies [6, 10, 40]. Moreover, large-scale clinical studies are needed to assess the ISF-blood correlation across different patient populations. These studies could benefit from advanced machine learning algorithms and data analytics approaches that render personalized models for precision dosing [1, 37].

The convergence of these efforts can establish an unprecedented wearable TDM modality. This modality directly addresses the problem of inappropriate drug dosing, which is a major cause of complications in antibiotics-based treatments. For tobramycin and vancomycin alone, these complications cause >40,000 acute kidney injuries and >\$5B treatment cost per year in the US [2, 22]. Recent studies have estimated that improvements in the accuracy of employed TDM methods can reduce these adverse outcomes by 3-fold [2]. In addition, the availability of a more practical TDM platform could also facilitate the access to drug regimens with higher chances of efficacy as opposed to the selection of alternative agents. The latter approach is often used in current medical practice to avoid the demands of TDM, but at the same time brings higher chances of failure as well as possibility of inducing antibiotic resistance (in the case of antibiotics). Therefore, we anticipate that the optimization and adoption of our technology can greatly promote enhanced pharmacotherapy outcomes with consequent improvements in the quality of life for large groups of patients as well as significant savings in healthcare costs. Furthermore, the presented technology can be adapted to monitor a wide range of clinically informative analytes (e.g., markers of disease and well-being). Thus, it can be broadly applied in a variety of biomonitoring settings (e.g., ISF biomarker investigations, large-scale clinical trials, and telehealth) and for various biomedical applications in order to advance personalized and precision medicine.

6.7. Reference

1. H. C. Ates, J. A. Roberts, J. Lipman, A. E. G. Cass, G. A. Urban, C. Dincer, *Trends Biotechnol.* **38**, 1262-1277, 2020.
2. B. V. Lee, G. Fong, M. Bolaris, M. Neely, E. Minejima, A. Kang, G. Lee, C. L. Gong, *Clin. Microbiol. Infec.* **27**, 2021.
3. D. N. Gilbert, C. Plamp, P. Starr, W. M. Bennett, D. C. Houghton, G. Porter, *Antimicrob. Agents Chemother.* **13**, 34-40, 978.
4. B. C. P. Koch, A. E. Muller, N. G. M. Hunfeld, B. C. M. de Winter, T. M. J. Ewoldt, A. Abdulla, H. Endeman, *Ther. Drug Monit.* **44**, 11-18, 2022
5. S. Lin, W. Yu, B. Wang, Y. Zhao, K. En, J. Zhu, X. Cheng, C. Zhou, H. Lin, Z. Wang, H. Hojaiji, C. Yeung, C. Milla, R. W. Davis, S. Emaminejad, *Proc. Natl. Acad. Sci. U.S.A.* **117**, 19017-19025, 2020.
6. T. M. Rawson, S. A. N. Gowers, D. M. E. Freeman, R. C. Wilson, S. Sharma, M. Gilchrist, A. MacGowan, A. Lovering, M. Bayliss, M. Kyriakides, P. Georgiou, A. E. G. Cass, D. O'Hare, A. H. Holmes, *Lancet Digit Health* **1**, e335-e343, 2019.
7. H. Teymourian, M. Parrilla, J. R. Sempionatto, N. F. Montiel, A. Barfidokht, R. Van Echelpoel, K. De Wael, J. Wang, *ACS Sens.* **5**, 2679-2700, 2020.
8. L. C. Tai, T. S. Liaw, Y. J. Lin, H. Y. Y. Nyein, M. Bariya, W. B. Ji, M. Hettick, C. S. Zhao, J. Q. Zhao, L. Hou, Z. Yuan, Z. Y. Fan, A. Javey, *Nano Lett.* **19**, 6346-6351, 2019.
9. R. K. Mishra, K. Y. Goud, Z. H. Li, C. Moonla, M. A. Mohamed, F. Tehrani, H. Teymourian, J. Wang, *J. Am. Chem. Soc.* **142**, 5991-5995, 2020.
10. J. Heikenfeld, A. Jajack, B. Feldman, S. W. Granger, S. Gaitonde, G. Begtrup, B. A. Katchman, *Nat. Biotechnol.* **37**, 407-419, 2019.

11. O. Cars, *Scand. J. Infect. Dis.*, 23-33, 1991.
12. W. Lee, S. H. Jeong, Y. W. Lim, H. Lee, J. Kang, H. Lee, I. Lee, H. S. Han, S. Kobayashi, M. Tanaka, B. S. Bae, *Sci. Adv.* **7**, eabi6290, 2021.
13. M. Parrilla, M. Cuartero, S. P. Sanchez, M. Rajabi, N. Roxhed, F. Niklaus, G. A. Crespo, *Anal. Chem.* **91**, 1578-1586, 2019.
14. S. Sharma, A. El-Laboudi, M. Reddy, N. Jugnee, S. Sivasubramaniyam, M. El Sharkawy, P. Georgiou, D. Johnston, N. Oliver, A. E. G. Cass, *Anal. Methods* **10**, 2088-2095, 2018.
15. J. O. Lee, H. M. So, E. K. Jeon, H. Chang, K. Won, Y. H. Kim, *Anal. Bioanal. Chem.* **390**, 1023-1032, 2008.
16. N. Arroyo-Curras, J. Somerson, P. A. Vieira, K. L. Ploense, T. E. Kippin, K. W. Plaxco, *Proc. Natl. Acad. Sci. U.S.A.* **114**, 645-650, 2017.
17. P. L. Mage, B. S. Ferguson, D. Maliniak, K. L. Ploense, T. E. Kippin, H. T. Soh, *Nat. Biomed. Eng.* **1** (5), 1-10, 2017.
18. P. Dauphin-Ducharme, K. Yang, N. Arroyo-Curras, K. L. Ploense, Y. M. Zhang, J. Gerson, M. Kurnik, T. E. Kippin, M. N. Stojanovic, K. W. Plaxco, *ACS Sens.* **4**, 2832-2837 (2019).
19. N. Arroyo-Curras, P. Dauphin-Ducharme, K. Scida, J. L. Chavez, *Anal. Methods* **12**, 1288-1310, 2020.
20. H. Teymourian, F. Tehrani, K. Mahato, J. Wang, *Adv. Healthc. Mater.* **10** (17), 2002255, 2021.
21. F. Paquette, A. Bernier-Jean, V. Brunette, H. Ammann, V. Lavergne, V. Pichette, S. Troyanov, J. Bouchard, *Nephron* **131**, 153-160, 2015.
22. InsightRX, “2020 Vancomycin Dosing Guidelines - InsightRX White Paper” (2020, content.insight-rx.com/vancowp).

23. P. A. Vieira, C. B. Shin, N. Arroyo-Curras, G. Ortega, W. W. Li, A. A. Keller, K. W. Plaxco, T. E. Kippin, *Front. Mol. Biosci.* **6**, 69, 2019.
24. J. Liu, S. Wagan, M. D. Morris, J. Taylor, R. J. White, *Anal. Chem.* **86**, 11417-11424, 2014.
25. B. S. Ferguson, D. A. Hoggarth, D. Maliniak, K. Ploense, R. J. White, N. Woodward, K. Hsieh, A. J. Bonham, M. Eisenstein, T. E. Kippin, K. W. Plaxco, H. T. Soh, *Sci. Transl. Med.* **5** (213), 213ra165-213ra165, 2013.
26. Y. Xiao, A. A. Lubin, A. J. Heeger, K. W. Plaxco, *Angew. Chem., Int. Edit.* **44**, 5456-5459, 2005.
27. A. H. Bretag, *Life Sci.* **8**, 319-329, 1969.
28. N. Arroyo-Curras, G. Ortega, D. A. Copp, K. L. Ploense, Z. A. Plaxco, T. E. Kippin, J. P. Hespanha, K. W. Plaxco, *ACS Pharmacol. Transl. Sci.* **1**, 110-118, 2018.
29. K. K. Leung, A. M. Downs, G. Ortega, M. Kurnik, K. W. Plaxco, *ACS Sens.* **6**, 3340-3347, 2021.
30. L. Thorsteinn, *Essential pharmacokinetics: a primer for pharmaceutical scientists* (Elsevier/AP, Boston, MA, 2015).
31. M. Rajabi, N. Roxhed, R. Z. Shafagh, T. Haraldson, A. C. Fischer, W. van der Wijngaart, G. Stemme, F. Niklaus, *Plos One* **11** (12), e0166330, 2016.
32. Y. Xiao, R. Y. Lai, K. W. Plaxco, *Nat. Protoc.* **2**, 2875-2880, 2007.
33. N. Arroyo-Curras, K. Scida, K. L. Ploense, T. E. Kippin, K. W. Plaxco, *Anal. Chem.* **89**, 12185-12191, 2017.
34. J. W. Seo, K. Y. Fu, S. Correa, M. Eisenstein, E. A. Appel, H. T. Soh, *Sci. Adv.* **8**, eabk2901, 2022.

35. A. M. V. Mohan, J. R. Windmiller, R. K. Mishra, J. Wang, *Biosens. Bioelectron.* **91**, 574-579, 2017.
36. Z. Y. Wang, J. Y. Luan, A. Seth, L. Liu, M. L. You, P. Gupta, P. Rathi, Y. X. Wang, S. S. Cao, Q. S. Jiang, X. Zhang, R. Gupta, Q. J. Zhou, J. J. Morrissey, E. L. Scheller, J. S. Rudra, S. Singamaneni, Microneedle patch for the ultrasensitive quantification of protein biomarkers in interstitial fluid. *Nat. Biomed. Eng.* **5**, 64-76 (2021).
37. J. M. Brockmeyer, R. T. Wise, E. B. Burgener, C. Milla, A. Frymoyer, *Pediatr. Pulm.* **55**, 3343-3350, 2020.
38. P. A. Vieira, C. B. Shin, N. Arroyo-Curras, G. Ortega, W. W. Li, A. A. Keller, K. W. Plaxco, T. E. Kippin, *Front. Mol. Biosci.* **6**, 69, 2019.
39. L. Lin, L. Grenier, Y. Bergeron, M. Simard, M. G. Bergeron, G. Labrecque, D. Beauchamp, *Antimicrob. Agents Chemother.* **38**, 54-60, 1994.

Figures

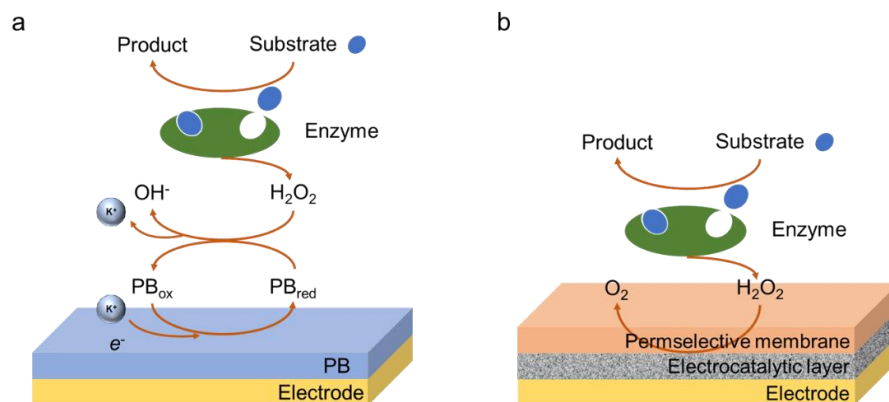


Figure 1.1. Schematic diagram of electroenzymatic sensor. (a) A Prussian Blue (PB) mediated sensor. (b) A mediator-free sensor.

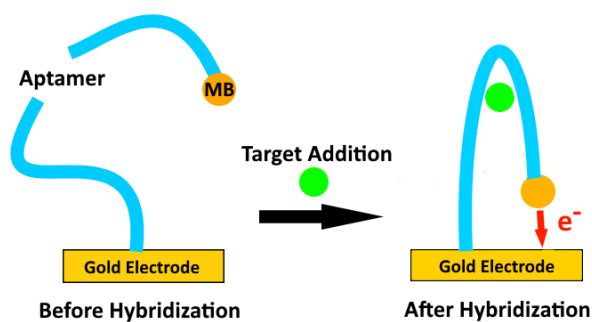


Figure 1.2. Schematic diagram of an electrochemical aptamer-based sensor.

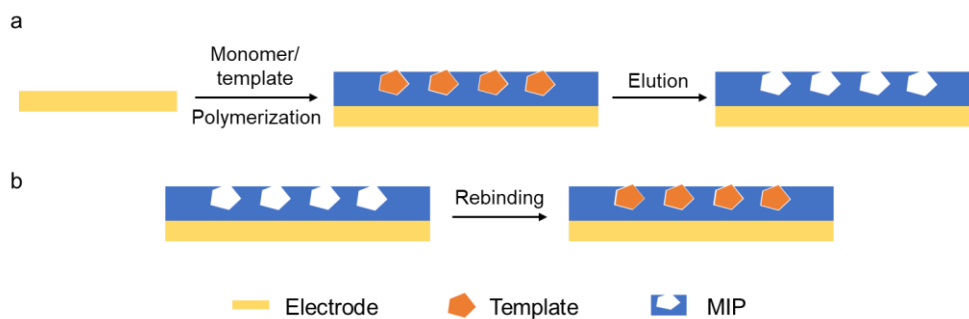


Figure 1.3. Schematic diagram of (a) fabrication and (b) application of molecularly imprinted polymers.

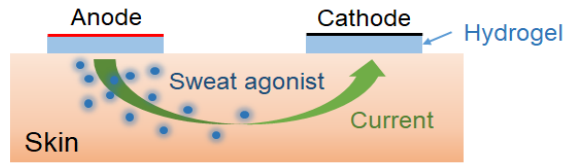


Figure 1.4. Schematic for iontophoresis-based sweat induction.

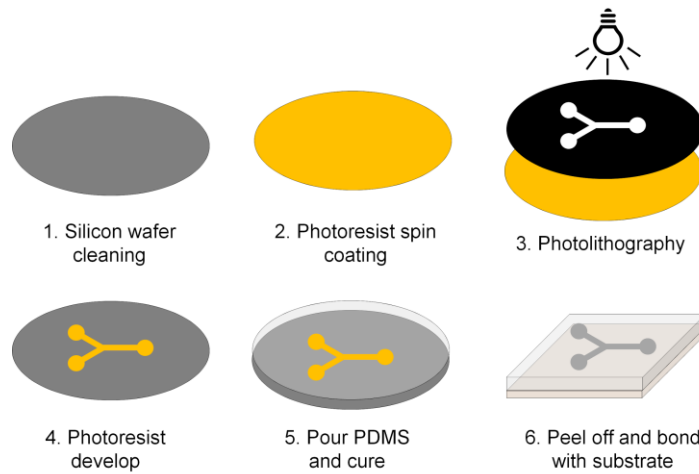


Figure 1.5. Schematic of PDMS-based microfluidic device fabrication.

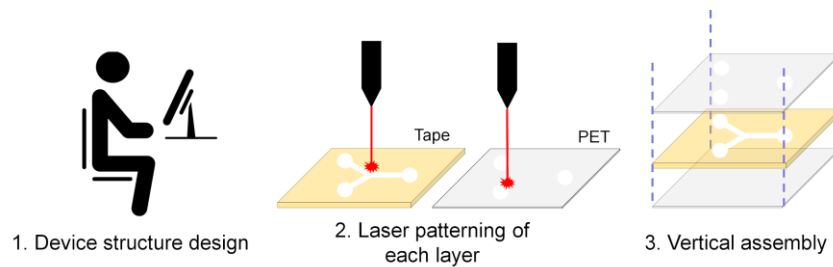


Figure 1.6. Schematic of tape-based microfluidic device fabrication.

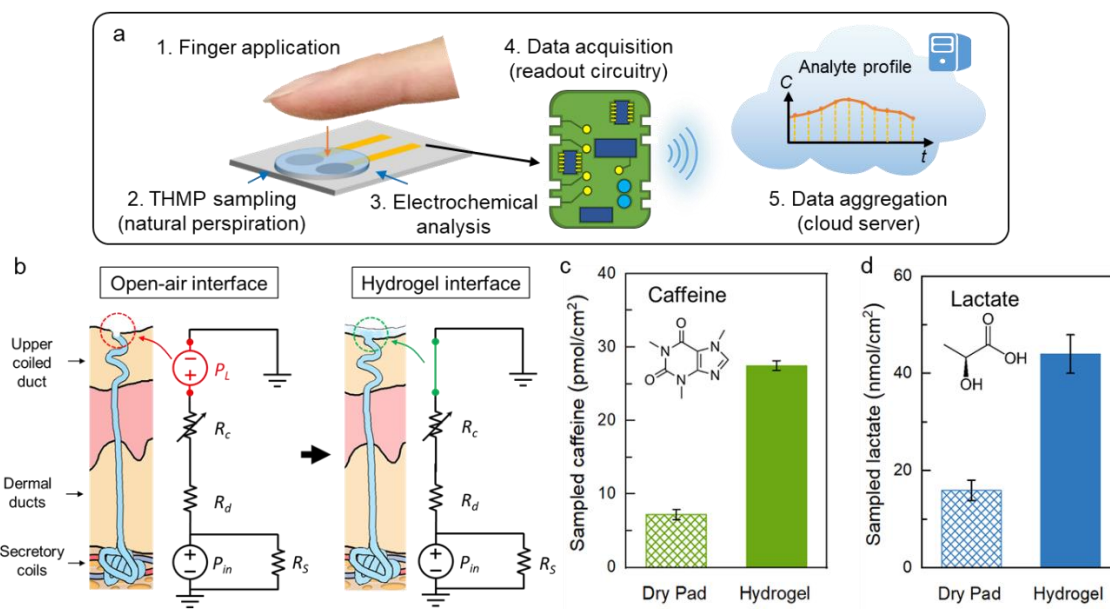


Figure 2.1. TH-based sampling and sensing interface: design rule and applications. (a) Schematic of the TH-based naturally perspired analyte sampling and wireless in-situ electrochemical analysis on a fingertip. (b) A first-order microfluidic model for natural perspiration sampling with an open-air interface and hydrogel interface. (c,d) Amount of caffeine (c) and lactate (d) sampled per unit area on fingertips with a dry absorbent pad (can be effectively considered as an open-air sampling interface) and hydrogel interface (sampled from four different fingers of the same subject, error bars indicate standard error). Sampling events targeting caffeine were conducted two hours after the consumption of beverages containing 150 mg caffeine.

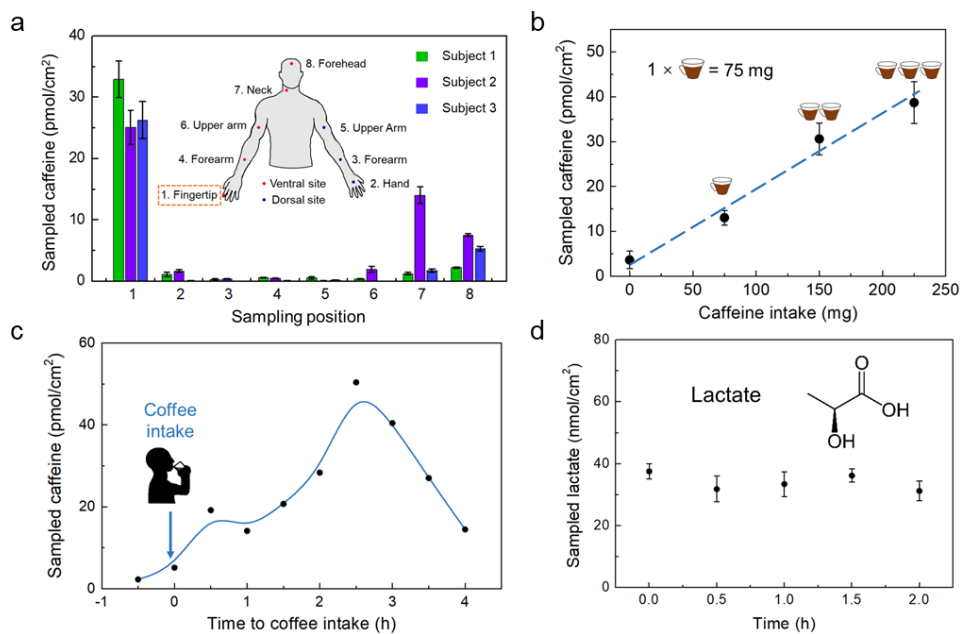


Figure 2.2. Characterization of naturally perspired analyte sampling with TH. (a) Amount of caffeine sampled per unit area on different body sites (three subjects with three trials at each position; sampled two hours after the consumption of a beverage containing 150 mg of caffeine; error bars indicate standard error). (b) Amount of caffeine sampled per unit area on fingertips of the same subject with different caffeine dosages (sampled from three different fingers, two hours after the consumption of beverages with the annotated caffeine content, error bars indicate standard error). (c) Amount of caffeine sampled per unit area on fingertips of a single subject at 30-minute intervals before and after the consumption of a beverage containing 150 mg of caffeine. (d) Amount of lactate sampled per unit area on fingertips at 30-minute intervals (from a sedentary subject, sampled from three different fingers, error bars indicate standard error).

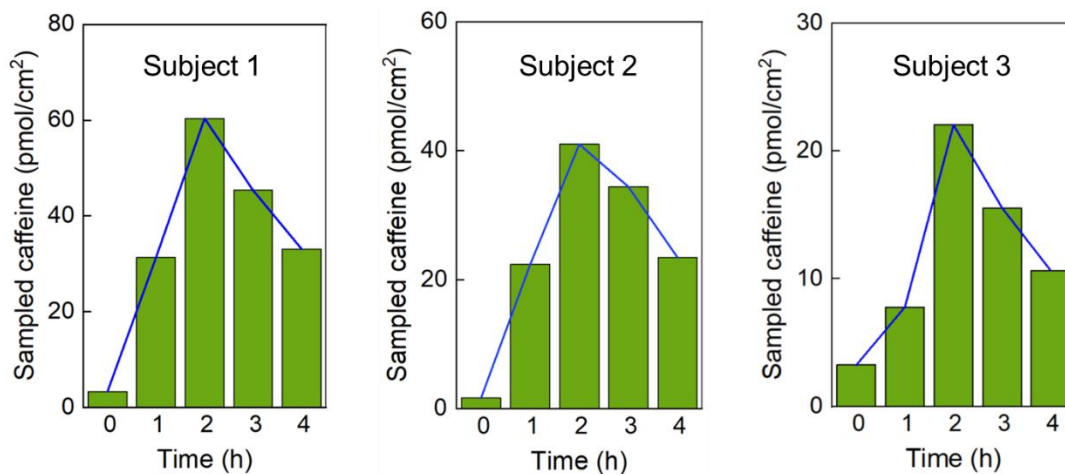


Figure 2.3. Amount of caffeine sampled per unit area from the index fingertips of three subjects at 1-hour intervals (upon the consumption of a beverage containing 150 mg of caffeine).

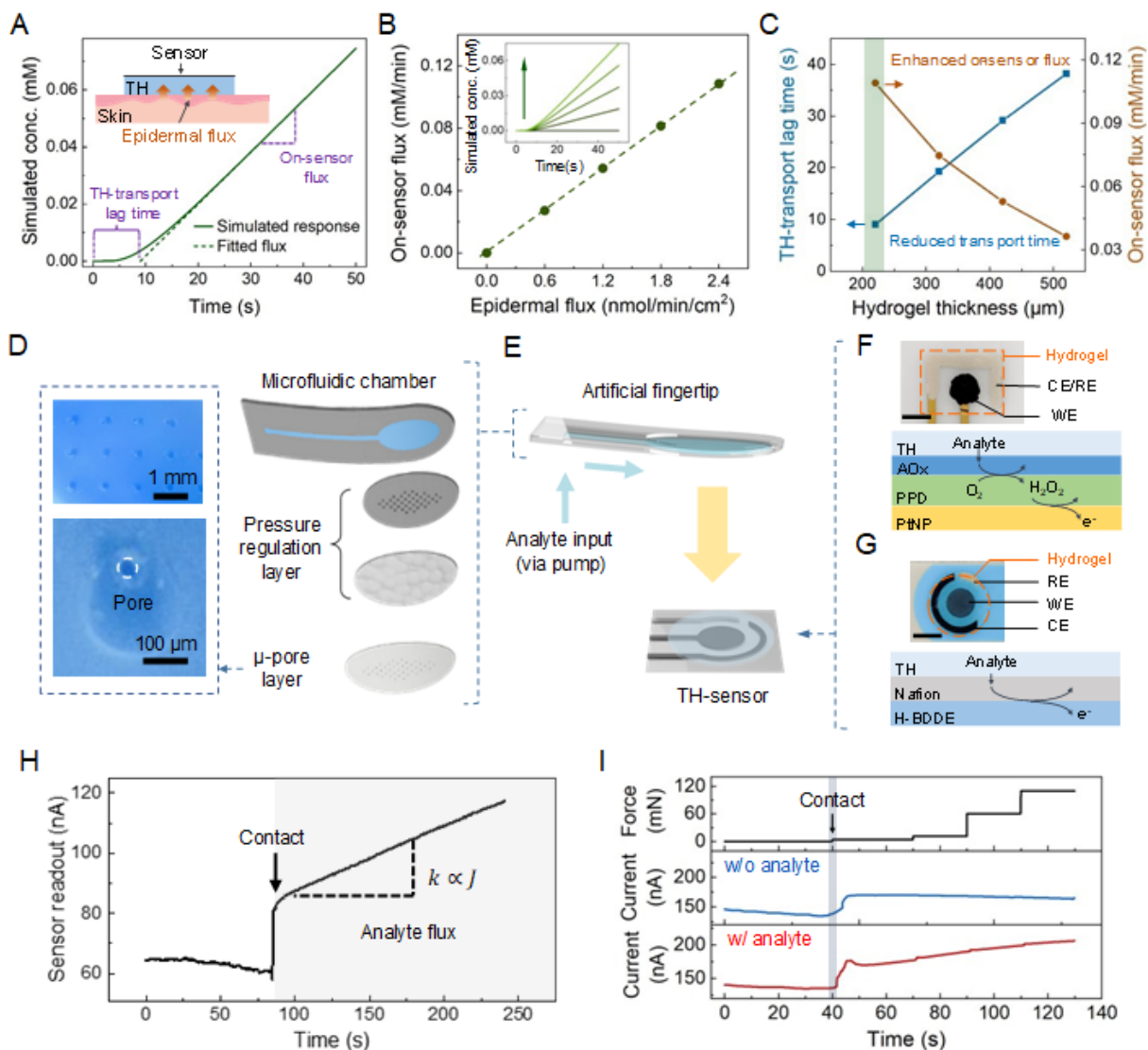


Figure 2.4. Development and validation of a TH-sensing signal interpretation framework. (A-C) Simulation of analyte concentration profile within the TH. (A) Simulated temporal profiles of analyte concentration at the vicinity of the sensor surface for a representative input flux (TH thickness: 220 μm , input flux: 2.4 $\text{nmol}/\text{min}/\text{cm}^2$). Inset shows the side view schematic of the analyte delivery to the sensor surface. (B) Simulated on-sensor analyte flux (for $t \gg t_D$) versus epidermal analyte flux, illustrating a linear relationship. Inset shows the corresponding simulated temporal profiles of analyte concentration at the vicinity of the sensor surface. (C) TH-transport lag time and on-sensor flux versus hydrogel thickness, demonstrating the superior TH-sensor performance (reduced lag time and enhanced on-sensor flux) when using a thinner hydrogel. (D) Exploded view of the artificial fingertip. Inset shows the optical images of

the laser-patterned μ -pore layer (with two different zoom-in views). (E) Ex-situ characterization of the TH-sensor via a microfluidic artificial fingertip. (F, G) Top-view photos and reaction schematics of the ethanol TH-sensor (F) and the APAP TH-sensor (G). WE, CE, and RE correspondingly denote working, counter, and reference electrodes. Scale bar: 2 mm. (H) Amperometric recording of an ethanol TH-sensor upon contact with an ethanol-contained artificial fingertip (concentration: 2 mM). (I) Amperometric recording of an ethanol TH-sensor in the presence of a varying pressing force profile. Top panel represents the exerted force profile. Middle and bottom panels correspondingly capture the measured TH-sensor's responses to the input fluid containing zero- and 2-mM ethanol.

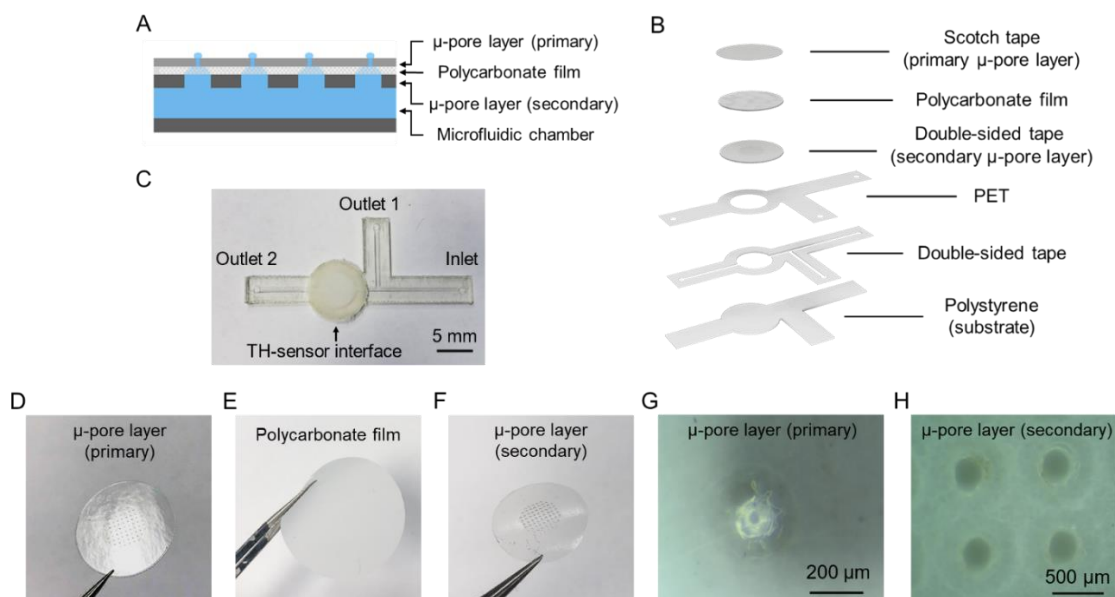


Figure 2.5. Structure of the microfluidic artificial fingertip. (A, B) Side view (A) and exploded view (B) schematics of the artificial fingertip. (C) Optical image of an assembled microfluidic fingertip. The inlet is connected to a syringe pump. The two outlets are utilized for the microfluidic chamber flushing. (D-F) Optical images of the primary μ -pore layer (D, based on a scotch tape), the polycarbonate film (E), and the secondary μ -pore layer (F, based on a double-sided tape). (G, H) Microscopic images of the primary (G) and secondary (H) μ -pore layers, showing the pore size and density of the laser-patterned pores. Primary:

pore size: $48 \pm 5 \mu\text{m}$ ($n = 10$), density: 139 cm^{-2} ; secondary: pore size: $292 \pm 17 \mu\text{m}$ ($n = 10$), pore density: 139 cm^{-2} .

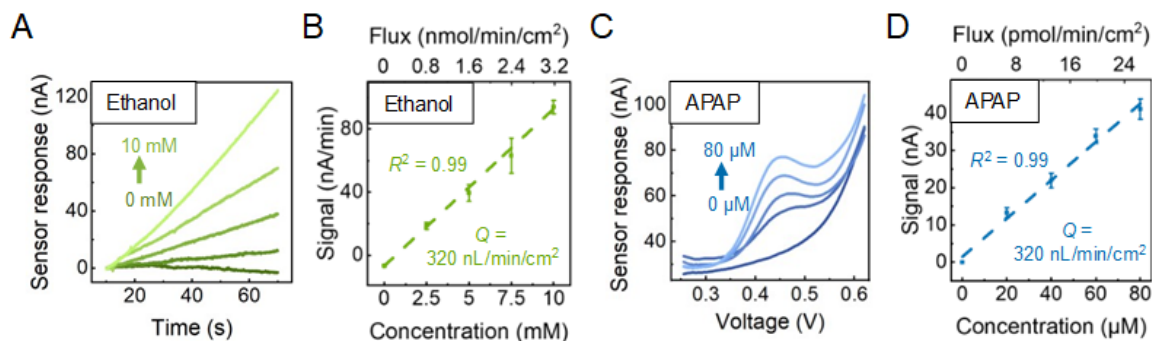


Figure 2.6. Ex-vivo characterization of TH-sensors using an artificial fingertip setup. (A) Amperometric responses of an ethanol TH-sensor to input fluid with various ethanol concentrations (0, 2, 4, 6, 8, 10 mM, all post-contact with the artificial fingertip). (B) Ethanol TH-sensor calibration curve. Error bars indicate standard error (three trials). (C) Differential pulse voltammograms of an APAP TH-sensor 3 min after the introduction of the input fluid with various APAP concentrations (0, 20, 40, 60, 80 μM). (D) APAP TH-sensor calibration curve. Error bars indicate standard error (three trials). For all the experiments the input fluid was based on a phosphate-buffered saline solution, injected at 320 nL/min/cm^2 .

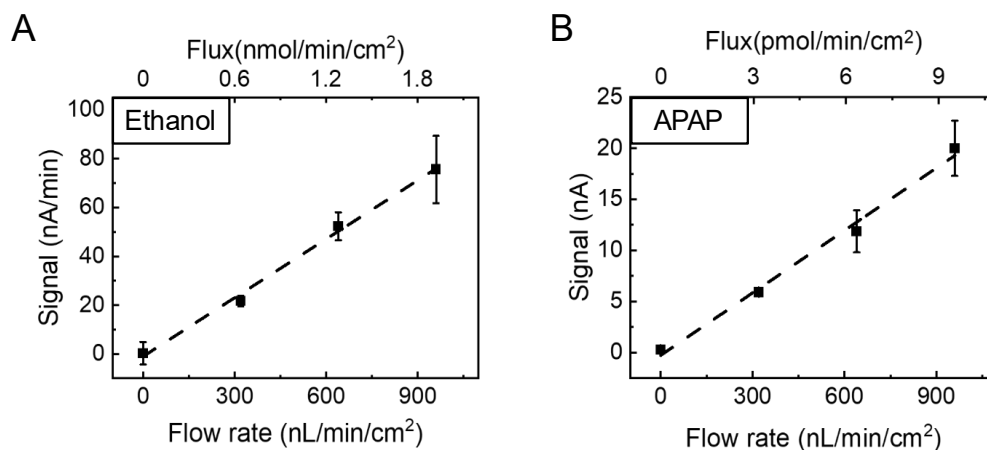


Figure 2.7. Ex-situ TH-sensor characterization under various flow rates. Calibration curves of an ethanol TH-sensor (A) and an APAP TH-sensor (B) under various input flow rates (using the artificial

fingertip). Error bars indicate standard error (three trials for each target). Ethanol concentration: 2 mM; APAP concentration: 10 μ M (both in PBS).

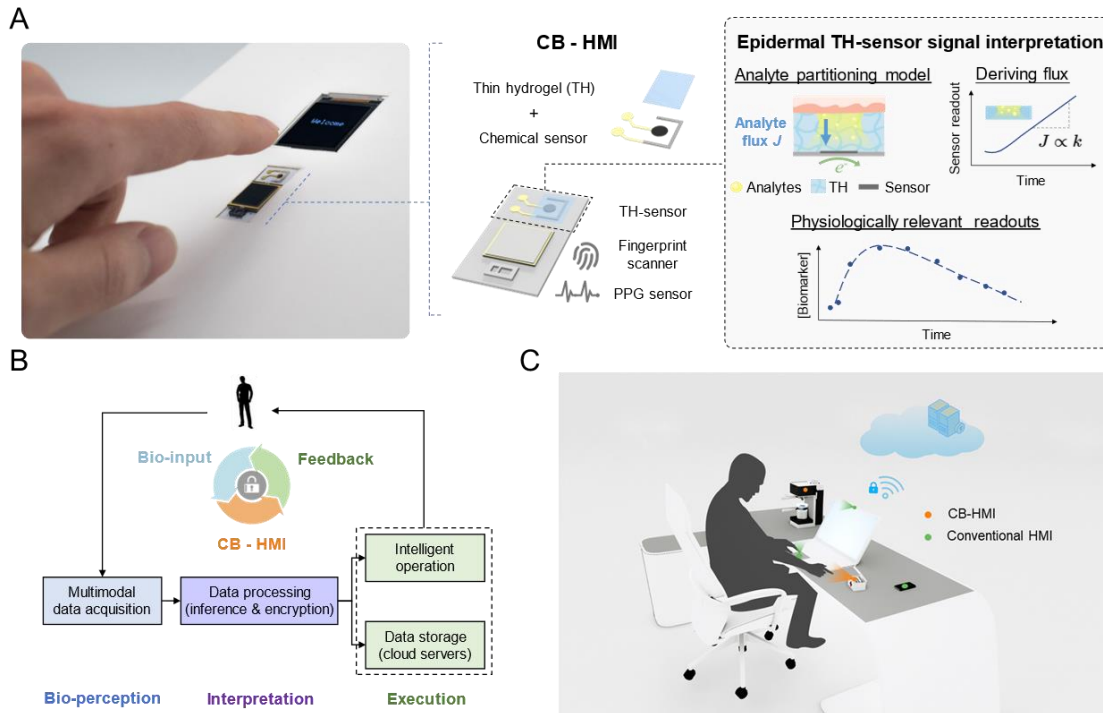


Figure 3.1. Enabling bio-perception and interpretation via CB-HMI. (A) Illustration of the translation of the user's touch-based entry into bio-inputs. Right: exploded view of the CB-HMI, including the TH-sensor component and corresponding signal interpretation framework. (B) CB-HMI's operational workflow, including its augmentation with feedback mechanisms. (C) Conceptual illustration of an ecosystem of objects, equipped with CB-HMI and conventional HMIs (e.g., touchpad and camera), forming a smart surrounding.

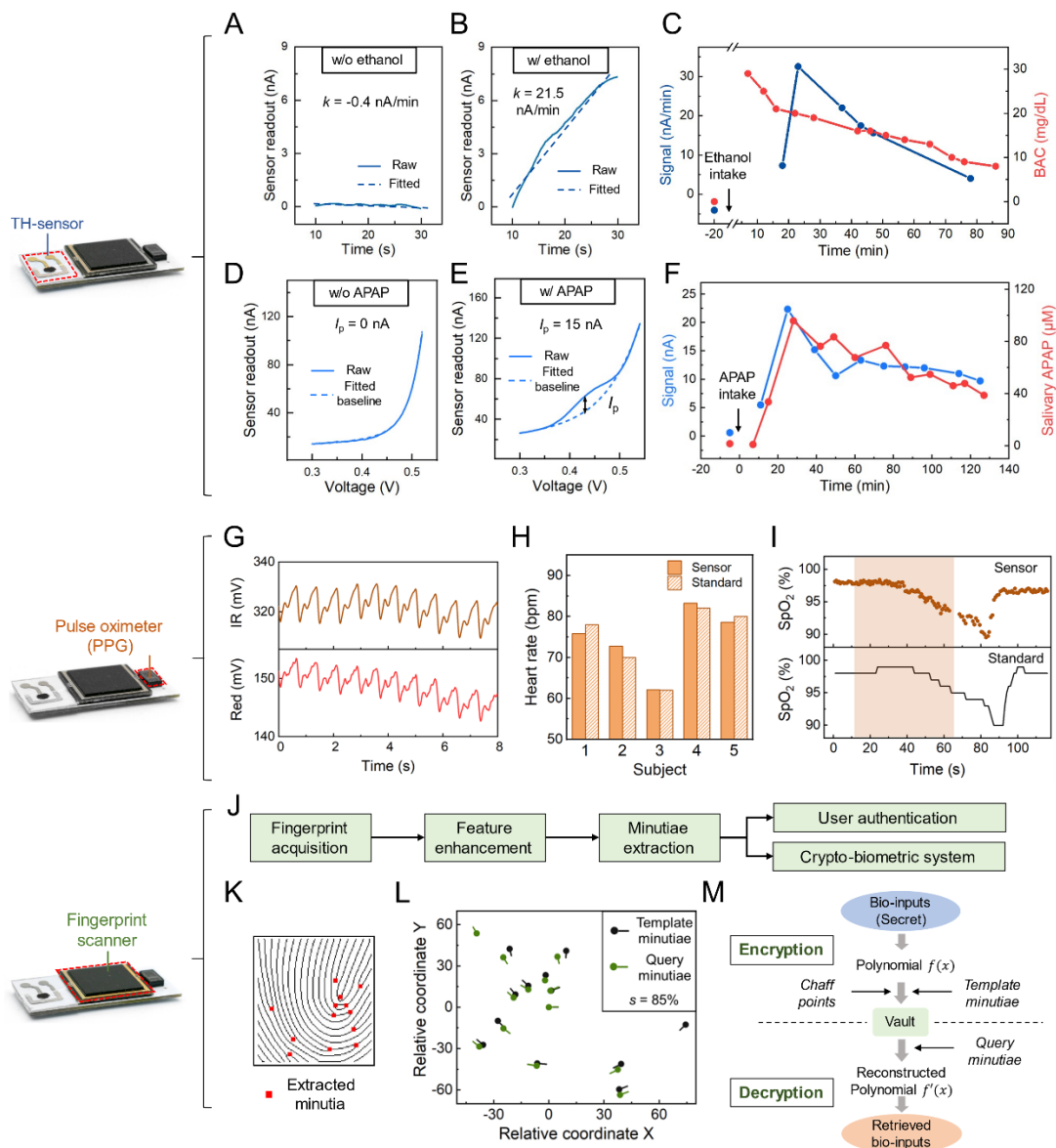


Figure 3.2. Development of the multimodal data acquisition and processing modules and validation via human subject studies. (A, B) The captured and linear-fitted ethanol TH-sensor readouts from the index fingertip of a subject (entry at $t = 0$ s) before (A) and 60 min after (B) the intake of an alcoholic beverage (~ 100 mL, 12.5% alcohol). (C) The temporal profile of the ethanol TH-sensor signal (obtained from the index fingertip of a subject) and concurrently measured BAC levels (20 min before, and after an alcoholic beverage intake: ~ 100 mL, 12.5% alcohol around $t = 0$ min). (D, E) The captured and baseline-fitted APAP TH-sensor readouts from the index fingertip of a subject before (D) and 60 min after (E) the

intake of an APAP-based medication (650 mg APAP). (F) The temporal profile of the APAP TH-sensor signal (obtained from the index fingertip of a subject) and concurrently sampled salivary APAP levels (analyzed using liquid chromatography with tandem mass spectrometry, LC-MS/MS) 5 min before, and after an APAP-based medication (650 mg APAP at $t = 0$ min). (G) PPG sensor readouts from the index fingertip of a subject (Top: IR channel, bottom: red channel). (H) HR of five subjects measured by the PPG sensor and a standard pulse oximeter. (I) The temporal profile of the SpO₂ level for a breath holding experiment, concurrently measured by the PPG sensor (top panel) and a standard pulse oximeter (bottom panel). The shaded area indicates the period of breath holding. (J) The user identification and biometric-encryption workflow. (K) A representative scanned and processed fingerprint with the extracted minutiae features annotated. (L) The corresponding plot of relative coordinates and local ridge direction of a pair of template and query fingerprints. (M) Schematic of fuzzy vault algorithm for biometric encryption of bio-inputs, leveraging the fingerprint minutiae pattern as the cryptographic key. Left-column images highlight the relevant units of the CB-HMI data acquisition module: a TH-sensor (here, ethanol), a PPG sensor, and a fingerprint scanner.

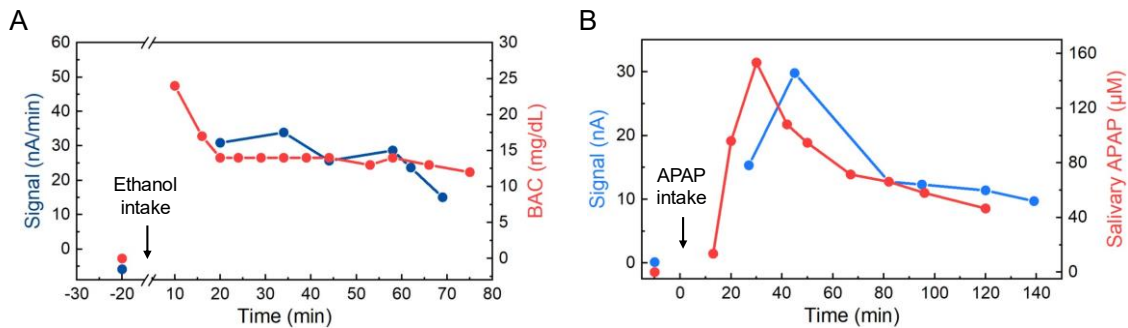


Figure 3.3. Temporal profiles of biochemical indices (second subject). (A) The temporal profile of the ethanol TH-sensor signal (obtained from the index fingertip of the second subject) and concurrently measured BAC levels (20 min before, and after an alcoholic beverage intake: ~ 100 mL, 12.5% alcohol). (B) The temporal profile of the APAP TH-sensor signal (obtained from the index fingertip of the second subject) and concurrently sampled salivary APAP levels (analyzed using LC-MS/MS) 5 min before, and after an APAP-based medication (650 mg APAP).

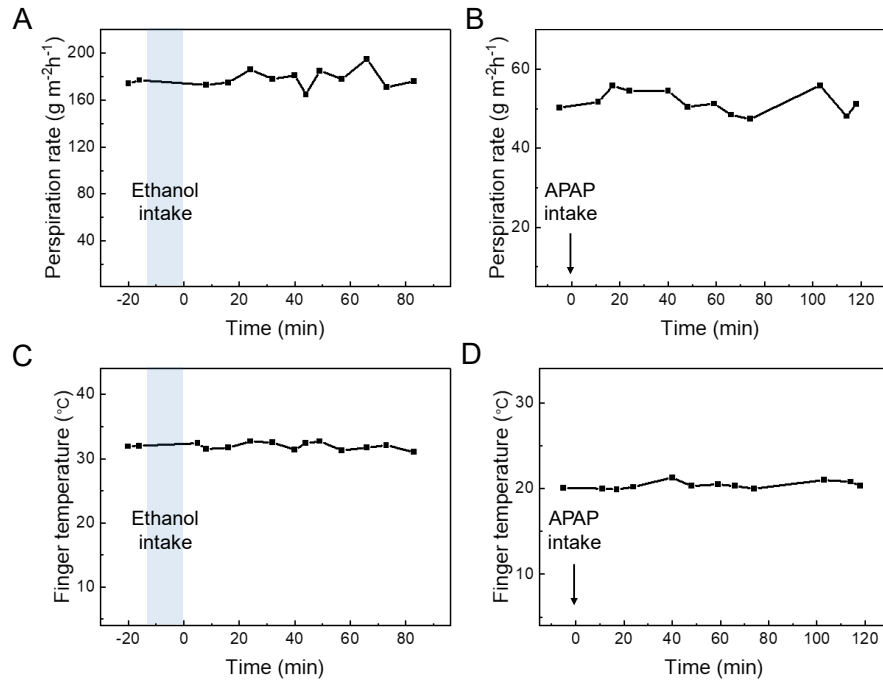


Figure 3.4. Direct and indirect measurement of the natural perspiration rate profile. (A, B) The temporal profile of the thermoregulatory natural perspiration rate (A) and the skin temperature (B) measured on the index fingertip of a subject (before and after an alcoholic beverage intake: ~ 100 mL, 12.5% alcohol). (C, D) The temporal profile of the thermoregulatory natural perspiration rate (C) and the skin temperature (D) measured on the index fingertip of a subject (before and after an APAP-based medication intake: 650 mg APAP).

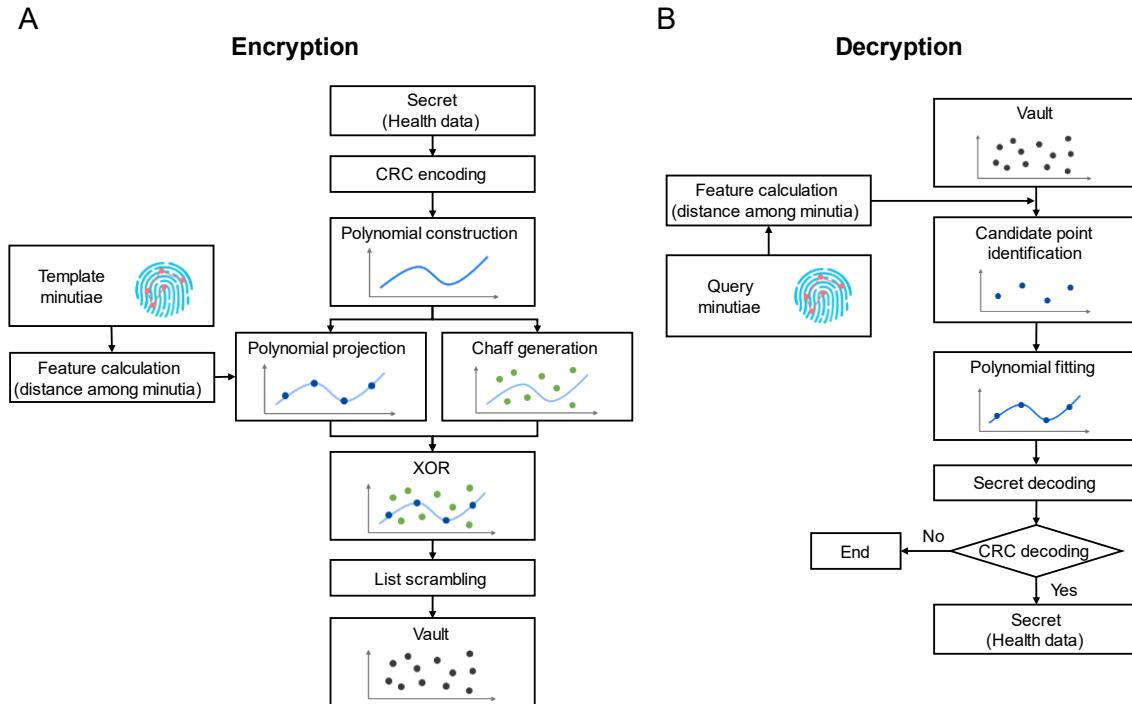

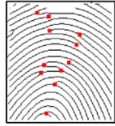


Figure 3.5. CBS encryption and decryption procedure. Flow charts of encryption (A) and decryption (B) procedure for the implemented fuzzy vault CBS algorithm. Detailed encryption and decryption procedure is described in the Materials and Method section. XOR: “exclusive or” logical operation.

Encryption

Fingerprint	Minutiae	Biometric key	Input
		[105, 292, 304, 351, 397, 468, 479, 538, 549, 854]	61234567890

Decryption








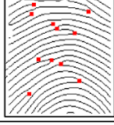
Fingerprint	Minutiae	Biometric key	Output
		[81, 304, 351, 374, 409, 456, 468, 514, 549, 702]	1234567890
		[93, 292, 304, 351, 397, 456, 468, 503, 526, 666]	1234567890
		[0, 117, 175, 187, 234, 304, 421, 561, 585, 760]	Fail
		[257, 362, 374, 549, 573, 596, 608, 690, 702, 1017]	Fail

Figure 3.6. Biometric-encryption/decryption of a hypothetical input. Tables show the encryption and four decryption attempts: the first two by the genuine subject, and the latter two (outlined in orange) by other subjects. Hypothetical input used: “1234567890”; Calculated CRC digit: 6 (in red). The first column shows the raw scanned fingerprints. The second column shows the processed fingerprints with the extracted minutiae features annotated. The third column shows the calculated biometric keys.

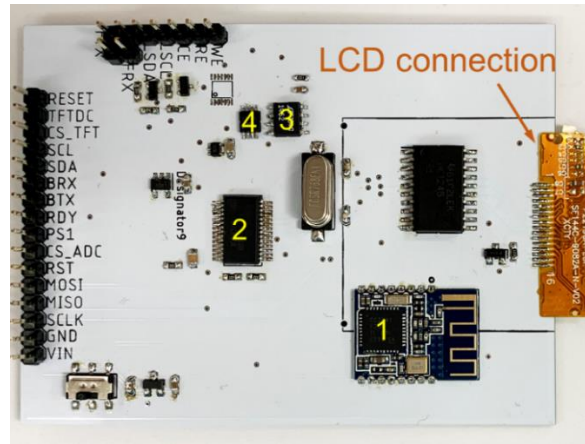


Figure 3.7. Photo of the data acquisition PCB module. The data acquisition PCB module (secondary) integrates: 1) a Bluetooth module, 2) an ADC, 3) a TIA, 4) a DAC.

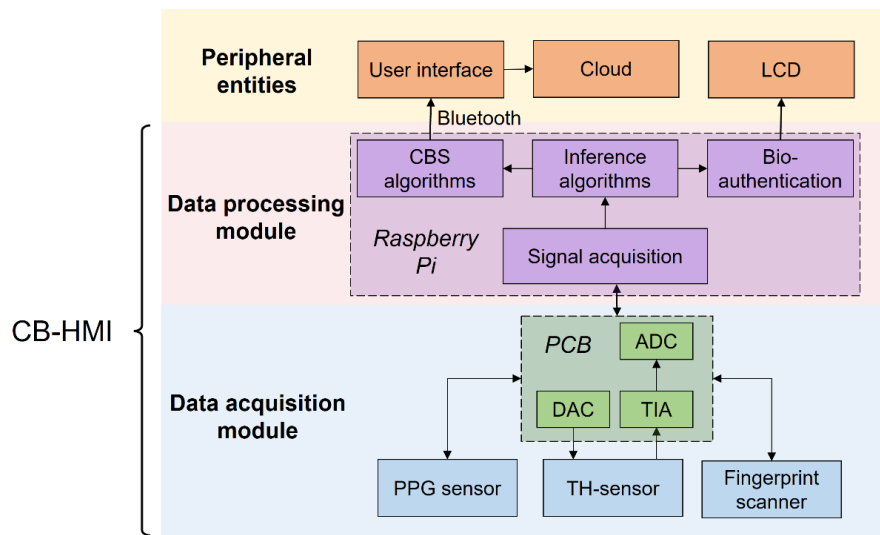


Figure 3.8. System-level block diagram of a CB-HMI-enabled system.

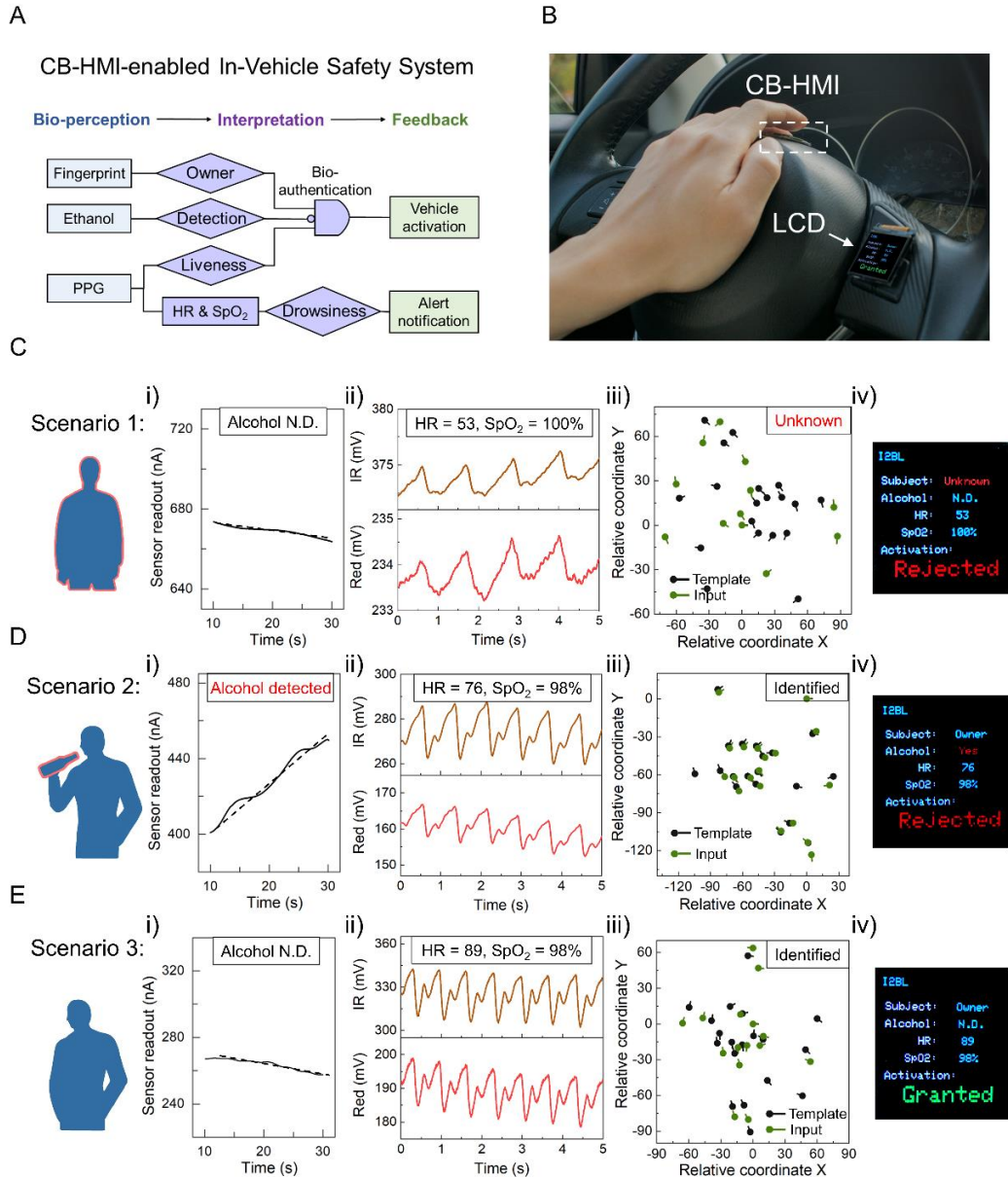


Figure 3.9. A CB-HMI-enabled in-vehicle safety system. (A) Operational workflow of the in-vehicle system. (B) Optical image of the in-vehicle system mounted on a steering wheel, illustrating the envisioned setting. (C-E) Validation of the system functionality in three hypothetical scenarios: non-owner/alcohol-free (C), owner with a recent alcohol intake (D, 1 h before fingertip-entry, ~ 100 mL beverage containing 12.5% alcohol), and owner/alcohol-free (E). For each scenario: (i) the raw and processed ethanol TH-sensor readouts (upon a fingertip-based entry at $t = 0$ s); (ii) PPG sensor readouts (IR and red channels); (iii) plot of relative coordinates and local ridge direction of the corresponding template and query fingerprints; and

(iv) visual feedback to the user via an LCD, displaying: the determined alcohol state of the subject, the derived HR and SpO₂ information, and the concluded bio-authentication status. N.D. indicates no detection of alcohol.

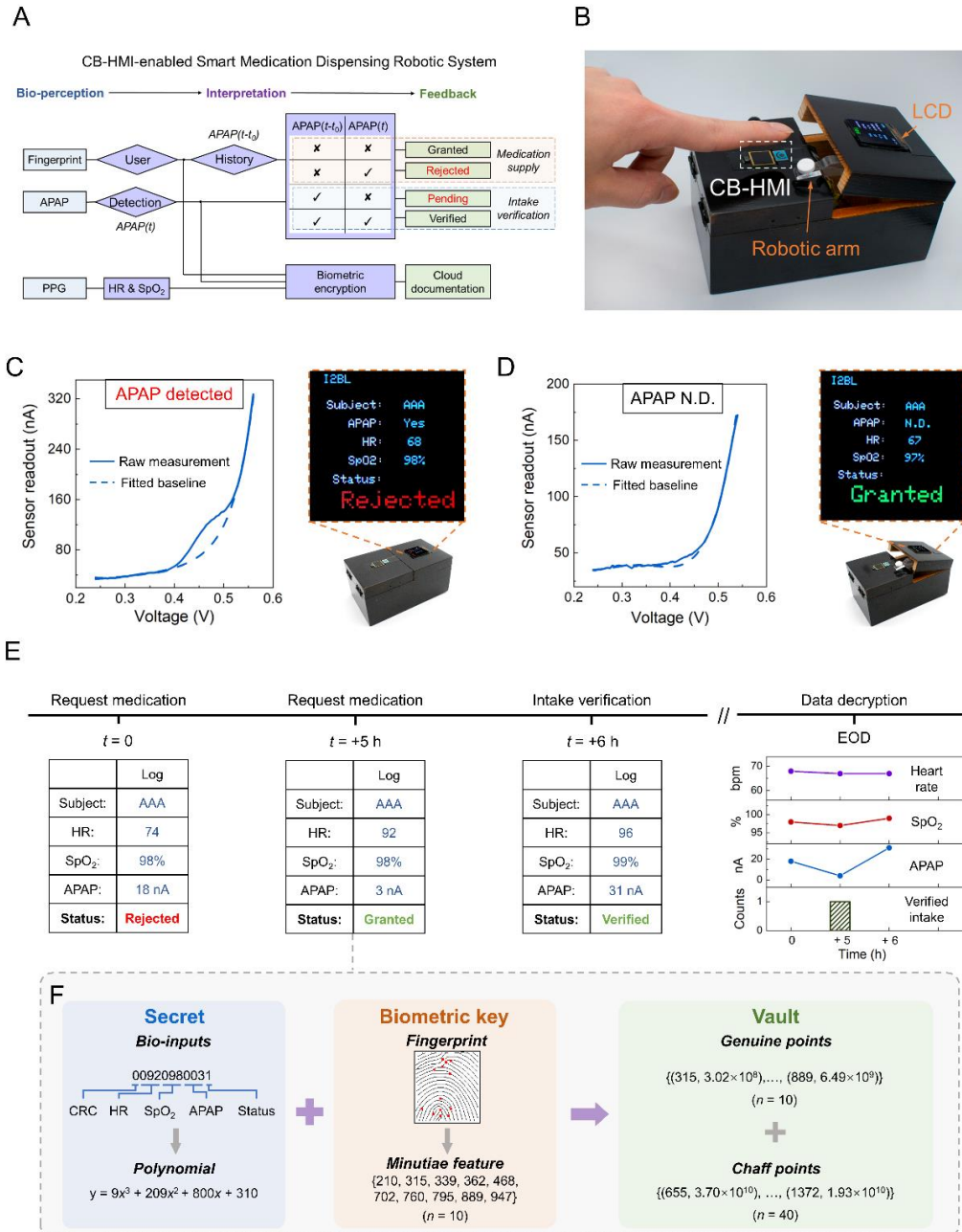


Figure 3.10. A CB-HMI-enabled medication dispensing robotic system. (A) Operational workflow of the medication dispensing robotic system. t denotes the time of entry and $t-t_0$ represents a 2-h period prior to the time of the entry. “✓” and “X” correspondingly represent the detection of relatively high and low levels of APAP (as determined by the defined signal threshold). (B) Optical image of the fully integrated medication dispensing system consisting of the CB-HMI, a medication delivery robotic arm, medication

storage compartment, and an LCD. (C, D) The raw and processed APAP TH-sensor readouts (upon an index fingertip-based entry) and corresponding system response for two cases: a subject with a recent APAP intake (C, 1 h, 650 mg APAP) and an APAP-free subject (D). N.D. indicates no detection of APAP. (E) Acquired bio-inputs and the corresponding status for three index fingertip entries at $t = 0, +5,$ and $+6$ h. Bottom right subfigure tabulates the decrypted retrieved bio-inputs and medication intake status at the end of day (EOD). (F) Encryption procedure for the second entry, illustrating the generation of: i) a secret-embedded polynomial using the acquired bio-inputs; ii) a biometric key based on the extracted minutiae features; and iii) genuine and chaff points to construct the vault.

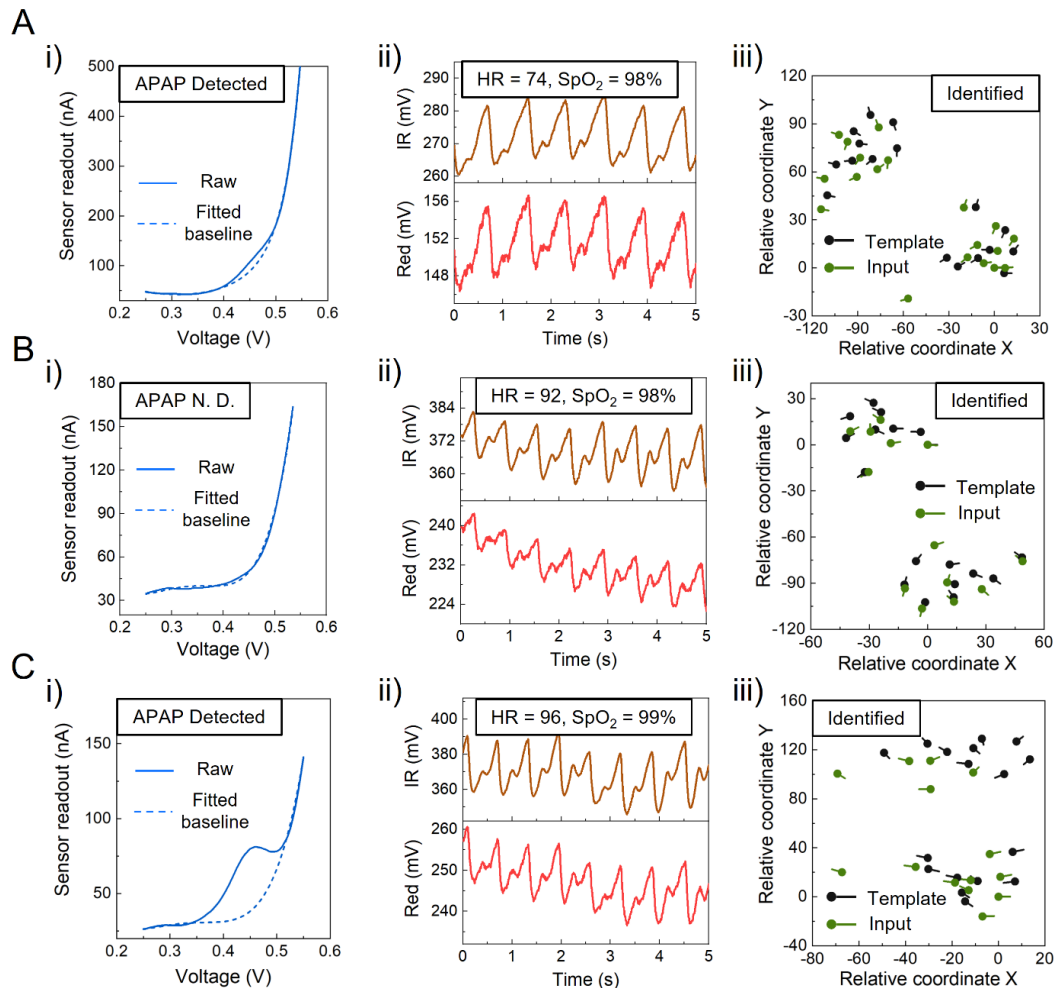


Figure 3.11. The raw and processed bio-inputs in the medication dispensing study. The raw and processed bio-inputs for three entries at different time points: (A) $t = 0$ h; (B) $t = +5$ h; (C) $t = +6$ h. For

each entry: (i) the raw and processed APAP TH-sensor readouts (30 s after the fingertip-based entry); (ii) PPG sensor readouts (IR and red channels); and (iii) plot of relative coordinates and local ridge direction of the corresponding template and query fingerprints. N.D. indicates no detection of APAP.

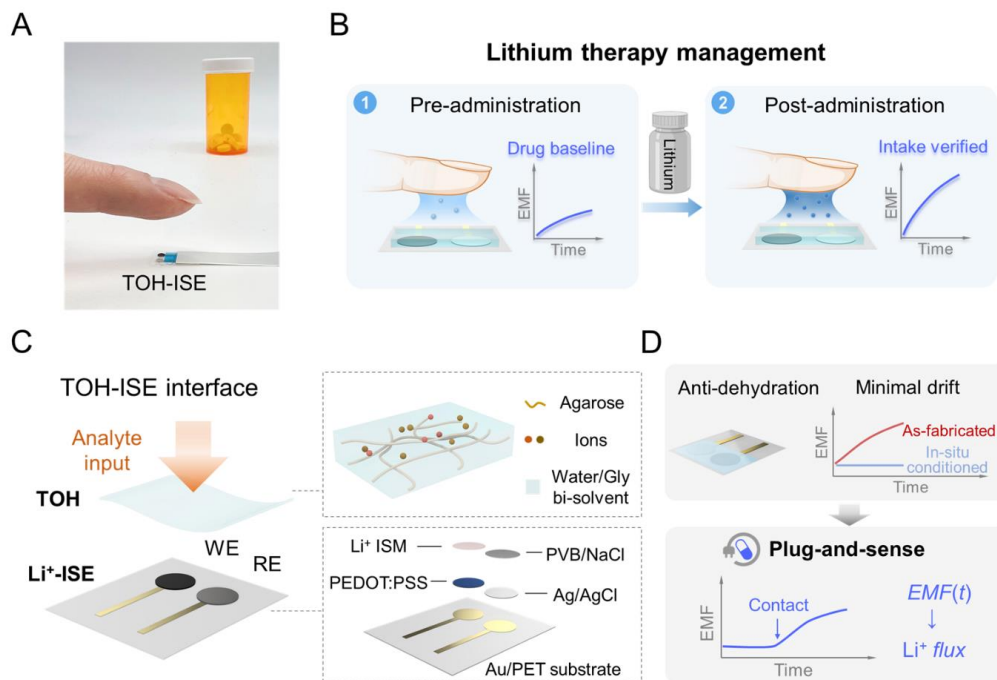


Figure 4.1. Touch-based lithium monitoring: design rationale and application. (A, B) A TOH-ISE interface that can be applied to monitor lithium adherence. (C) An illustrative view of a TOH-ISE interface (WE: working electrode; RE: reference electrode). Right: schematics showing the composition/structure of a TOH and the exploded view of a Li^+ ISE. (D) Unique features of our sensing interface, rendering lithium influx tracking in a plug-and-sense manner.

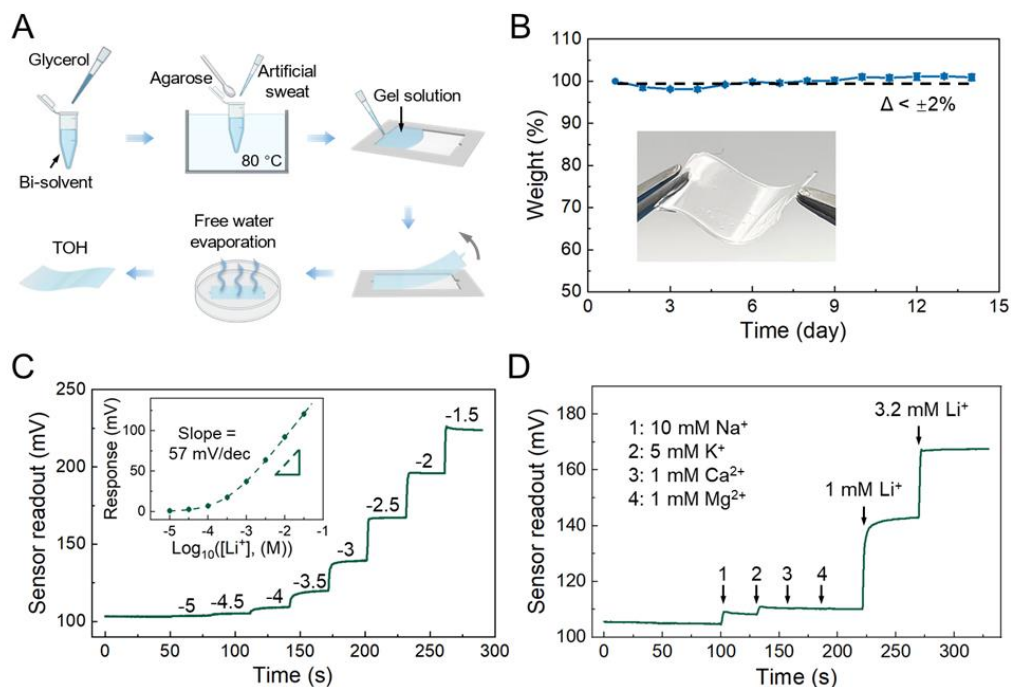


Figure 4.2. Characterization of individual components of the sensing interface. (A) Schematics of the TOH fabrication workflow. (B) Normalized TOH weight over 14 days. Error bars indicate standard deviation ($n = 10$). (C) Potentiometric readout of a Li^+ ISE with increasing Li^+ (lithium chloride, LiCl) concentration. Inset shows the calibration plot. Error bars indicate standard deviation of three sensors. (D) Selectivity study of a Li^+ ISE, where its potentiometric readout was monitored in relation to the sequential introduction of the interference ions and Li^+ . Both studies were performed in an electrochemical cell containing artificial sweat solution.

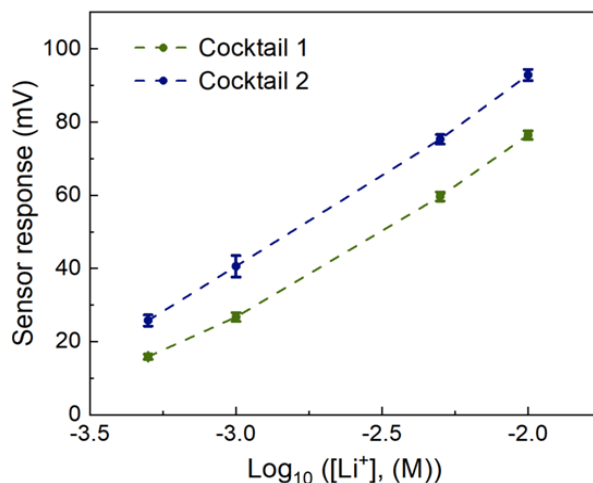


Figure 4.3. Comparison of two ISM cocktails. Responses of lithium ISEs in artificial sweat solutions. Sensors were fabricated using two previously-demonstrated ISM cocktails [ref] and tested by drop casting artificial sweat solutions with various lithium concentration levels. Error bars indicate standard deviation (three sensors for each cocktail). The inferior performance of ISEs fabricated using cocktail 2 results from their the poor selectivity towards Ca^{2+} , which can be attributed to the inclusion of trioctylphosphine oxide in the cocktail.

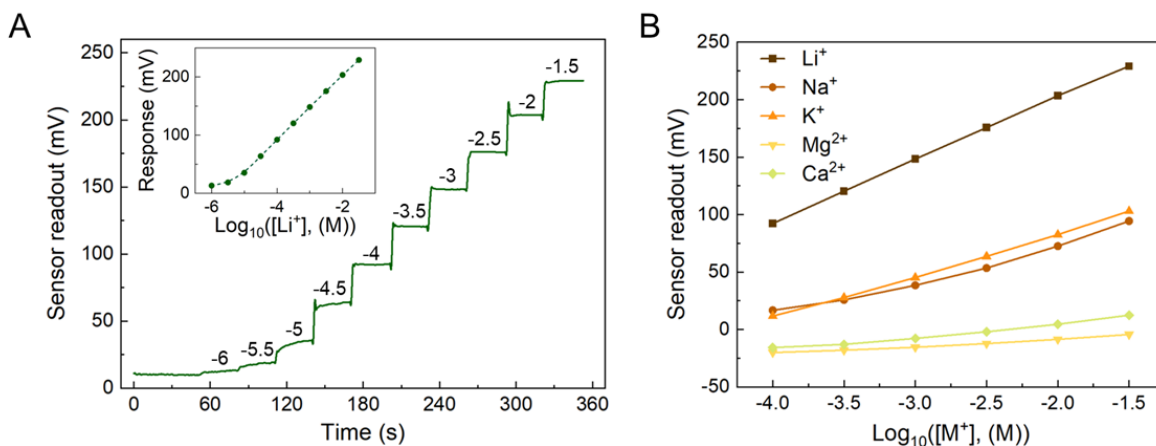


Figure 4.4. Li⁺ ISE characterization in DI water matrix. (A) Potentiometric readout of a Li⁺ ISE with increasing Li⁺ concentration. Inset shows the corresponding calibration plot. (B) Response of a Li⁺ ISE to the presence of varying concentration levels of Li⁺ and interfering ions. Both studies were performed in an electrochemical cell and using DI water as the testing solution.

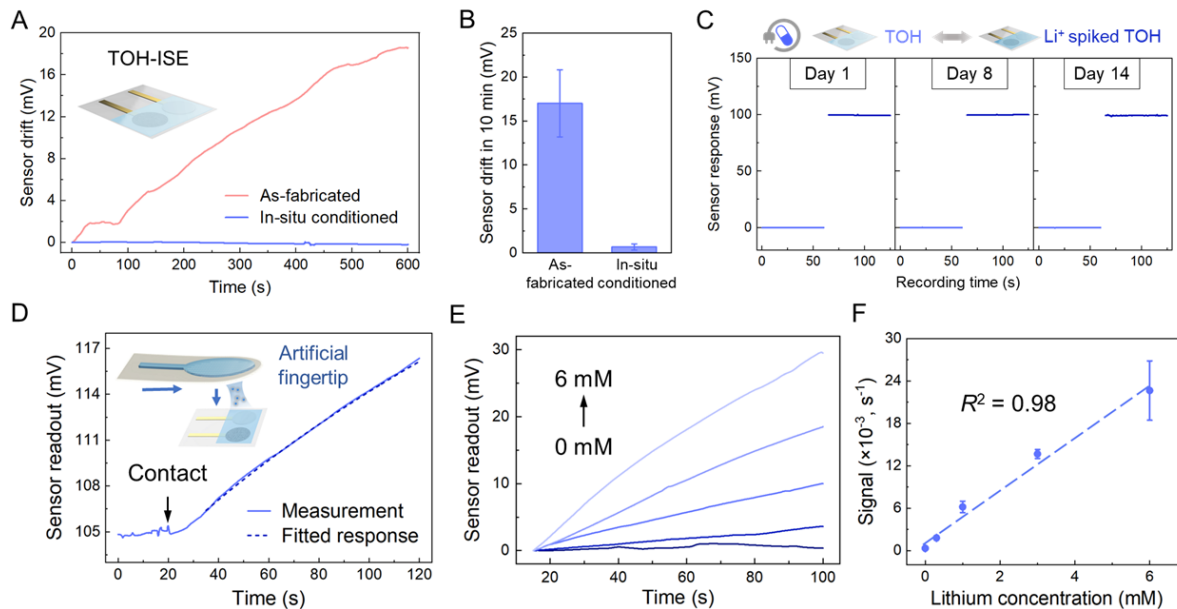


Figure 4.5. Ex-situ TOH-ISE characterization. (A) Real-time potentiometric readout drift of representative TOH-ISEs in their as-fabricated state (right after the coupling of TOH and ISE) and after overnight conditioning (in-situ conditioned state). Inset shows the schematic of a TOH-ISE. (B) Corresponding sensing signal drift magnitude in the first 10 min of the test. Error bars indicate standard deviation ($n = 5$). (C) Potentiometric response of a TOH-ISE interrogated at different days after fabrication. The sensing interface interrogation was performed by coupling swapping the TOH with a Li^+ -spiked TOH (1 mM Li^+ in the prepared gel solution). (D) Potentiometric recording of a TOH-ISE upon contact with a microfluidic artificial fingertip (delivering artificial sweat solution with 1 mM Li^+). Dotted line shows the corresponding signal interpretation framework fitted readout. Inset shows the schematic of the testing setup. (E) Potentiometric responses of a TOH-ISE to input fluid with various Li^+ concentrations (0, 0.3, 1, 6 mM, all post-contact with the artificial fingertip). (F) Corresponding calibration curve. Error bars indicate standard deviation (three trials).

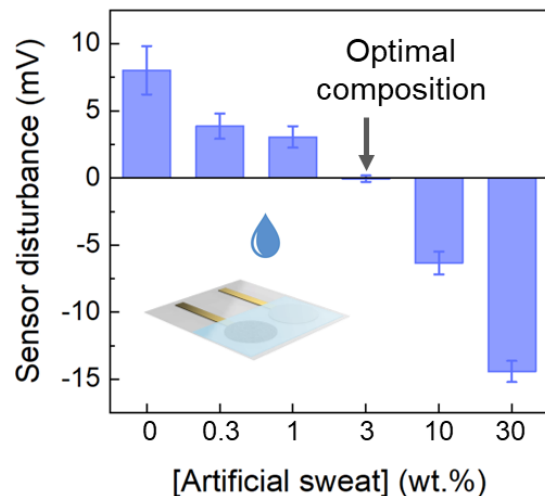


Figure 4.6. Variation of sensor readout in an emulated touch-based entry. TOH-ISE readout changes upon introduction of 1 μL blank artificial sweat solution (mimicking the touch-based entry). Inset shows the schematic of the testing setup. Here various amounts of artificial sweat solution were added into the gel solution during TOH fabrication. Error bars indicate standard deviation ($n = 3$). TOH fabricated using 3 wt.% artificial sweat leads to the smallest readout disturbance and thus was chosen as the optimal composition for the rest of TOH fabrication.

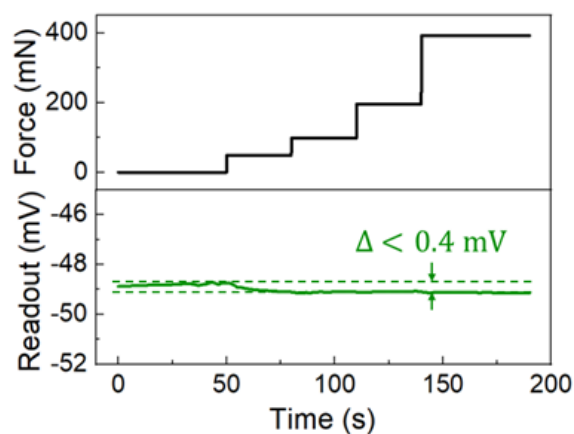


Figure 4.7. Interference of pressing force. Potentiometric recording of a TOH-ISE in the presence of a varying pressing force profile. The upper panel represents the exerted force profile, and the lower panel shows the measured sensor readout variation due to the force.

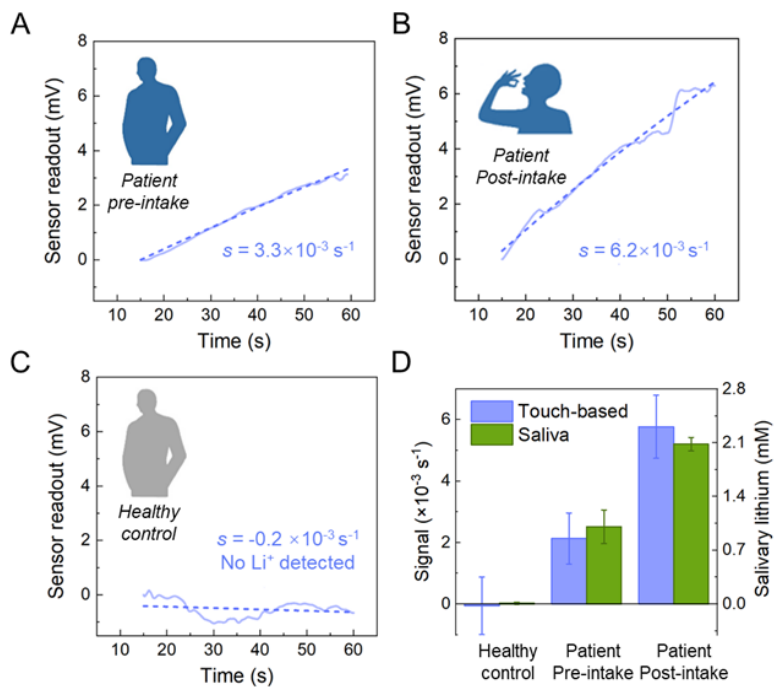


Figure 4.8. In-situ TOH-ISE validation. (A-C) Potentiometric TOH-ISE readouts and fitted responses on a patient before (A) and after (B) the scheduled daily lithium-based medication intake (900 mg lithium carbonate) as well as a healthy control subject (C). (D) Extracted touch-based sensing signal versus the corresponding salivary lithium concentration. Error bars indicate standard deviation. Healthy control: three subjects; Patient: three trials on the same subject.

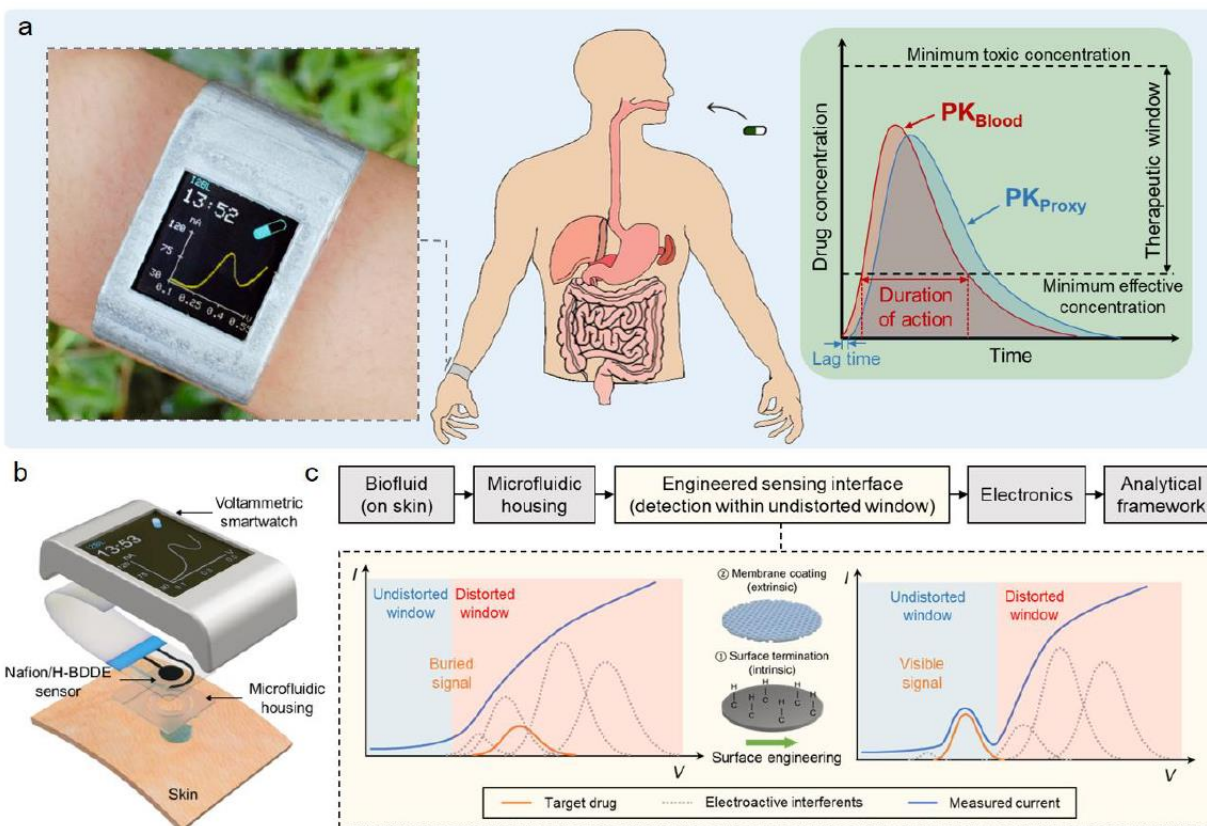


Figure 5.1. A fully-integrated wearable voltammetric drug monitoring solution: design rationale and application. (a) A voltammetric smartwatch, which can be applied to track the circulating drug's pharmacokinetics (PK) by providing proxy readouts in non-invasively retrievable biofluids. (b) An illustrative exploded view of the smartwatch components (containing microfluidic housing, Nafion/H-BDDE sensor, signal processing/transmission circuitry, LCD screen, and battery units, all embedded within a 3D-printed case). (c) Seamless operational workflow of the devised wearable voltammetric drug monitoring solution, utilizing an engineered voltammetric sensing interface to create an undistorted potential window for target drug detection (in the presence of endogenous electroactive interferents).

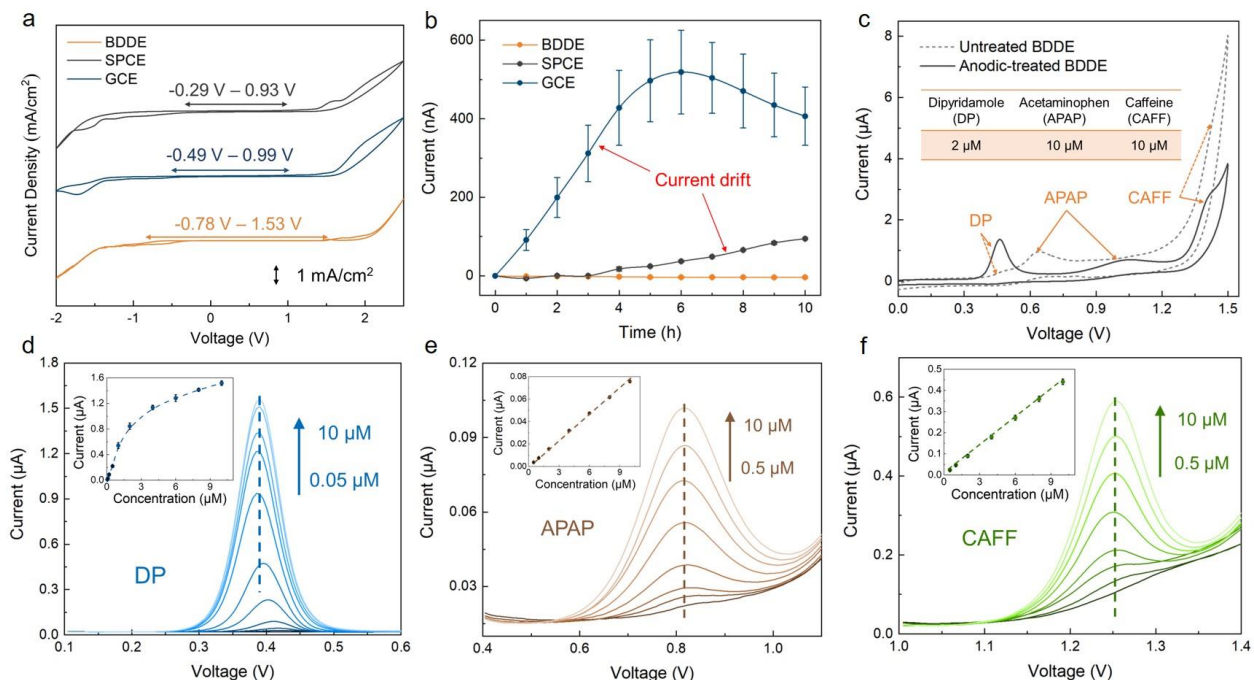


Figure 5.2. Voltammetric sensing electrode characterization. (a) Cyclic voltammograms of GCE, SPCE, and BDDE (performed in 0.01 M acetate buffer, pH = 5, scan rate: 25 mV/s) with the annotated potential window. (b) Baseline current of GCE, SPCE, and BDDE under high potential operation (1.2 V vs. Ag/AgCl, $n = 3$, error bars indicate standard error). (c) Cyclic voltammograms of untreated and anodic-treated BDDE in the presence of 2 μM DP, 10 μM APAP, and 10 μM CAFF (performed in 0.01 M acetate buffer, pH = 5, scan rate: 0.1 V/s). (d-f) Differential pulse voltammograms of anodic-treated BDDE with (d) 0, 0.05, 0.1, 0.2, 0.5, 1, 2, 4, 6, 8, 10 μM DP; (e) 0, 0.5, 1, 2, 4, 6, 8, 10 μM APAP; and (f) 0, 0.5, 1, 2, 4, 6, 8, 10 μM CAFF (performed in 0.01 M acetate buffer, pH = 5). Insets show the corresponding calibration curve ($n = 3$, error bars indicate standard error).

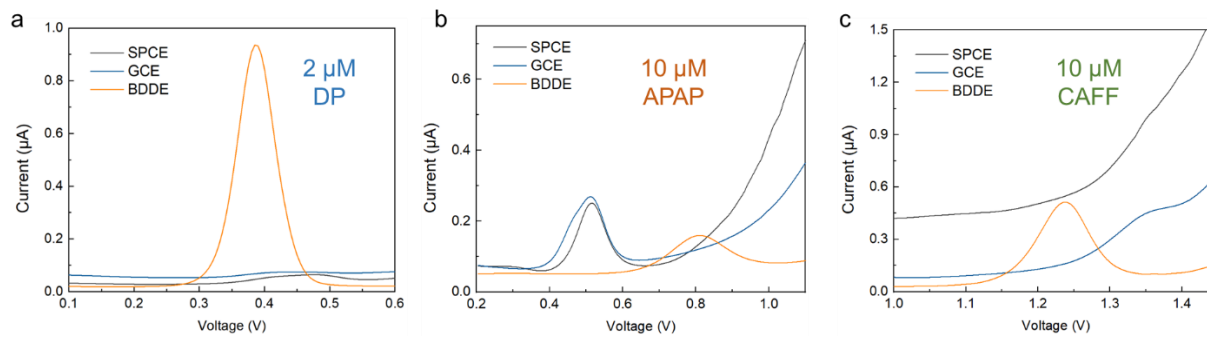


Figure 5.3. Comparison of the response of SPCE, GCE, and BDDE towards (a) 2 μM DP, (b) 10 μM APAP, and (c) 10 μM CAFF. All performed in 0.01 M acetate buffer, pH = 5.

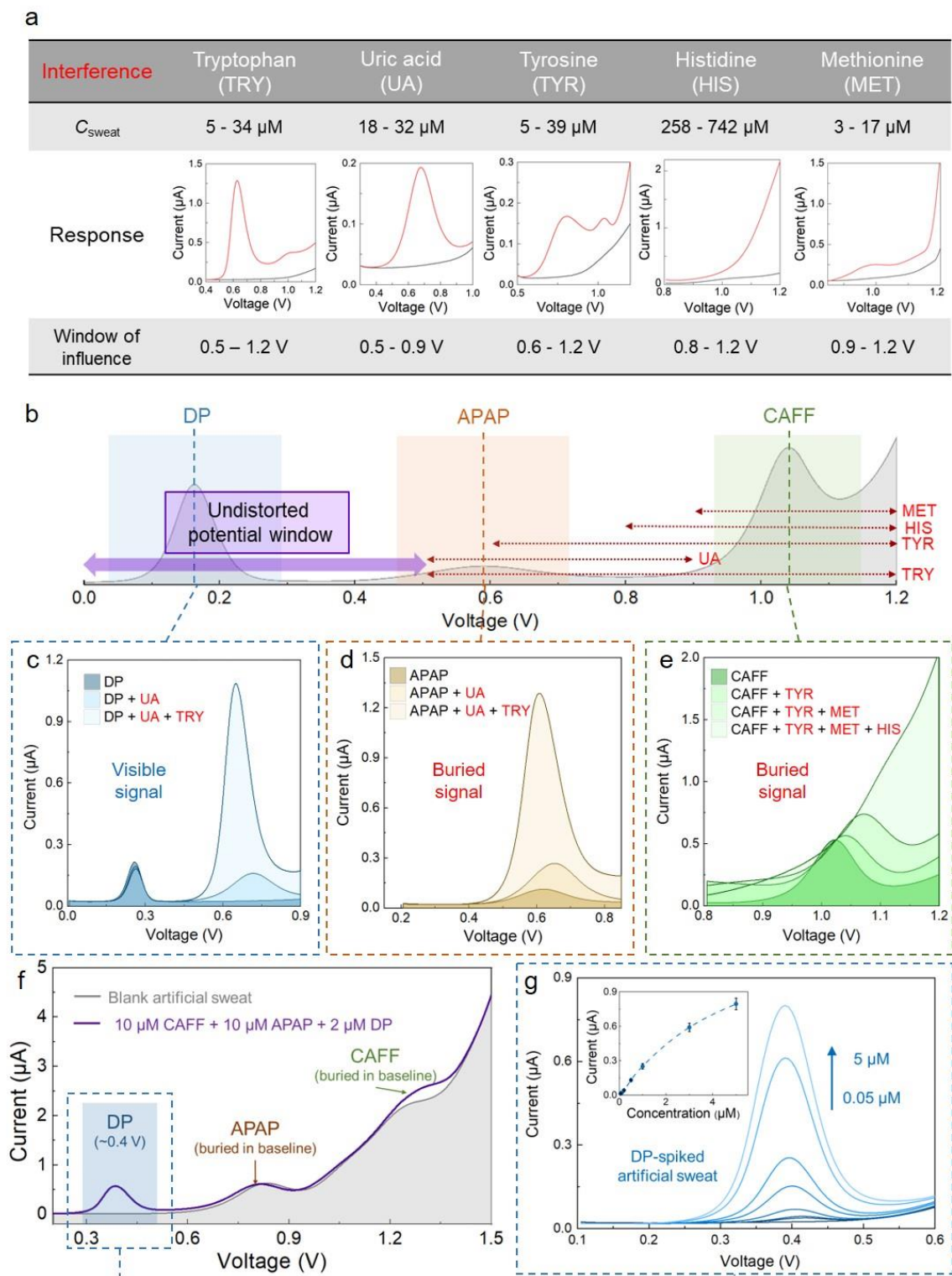


Figure 5.4. Systematic voltametric interference study. (a) Selected panel of endogenous electroactive interferents in sweat. 1st row: the interferents' concentration range in sweat; 2nd row: corresponding

differential pulse voltammograms of 20 μM TRY, 25 μM UA, 20 μM TYR, 10 μM MET, and 500 μM HIS (red) compared to the respective electrochemical background (black, no interferent spiked, all measurements were performed in 0.01 M acetate buffer, pH = 5); 3rd row: corresponding potential window of influence for each interferent. (b) Schematic differential pulse voltammogram where all the selected model drugs are present. The interferents' potential windows of influence and the undistorted potential window are annotated. (c-e) Differential pulse voltammograms of (c) 2 μM DP, (d) 10 μM APAP, and (e) 10 μM CAFF with subsequent addition of electroactive interferents oxidized at the proximal potential (20 μM TRY, 25 μM UA, 20 μM TYR, 10 μM MET, and 500 μM HIS). (f) Differential pulse voltammograms of blank artificial sweat and drug-spiked (2 μM DP, 10 μM APAP, and 10 μM CAFF) artificial sweat (pH = 5). (g) Differential pulse voltammograms of 0, 0.05, 0.1, 0.2, 0.5, 1, 3, 5 μM DP in artificial sweat (pH = 5). Inset shows the corresponding calibration curve ($n = 3$, error bars indicate standard error).

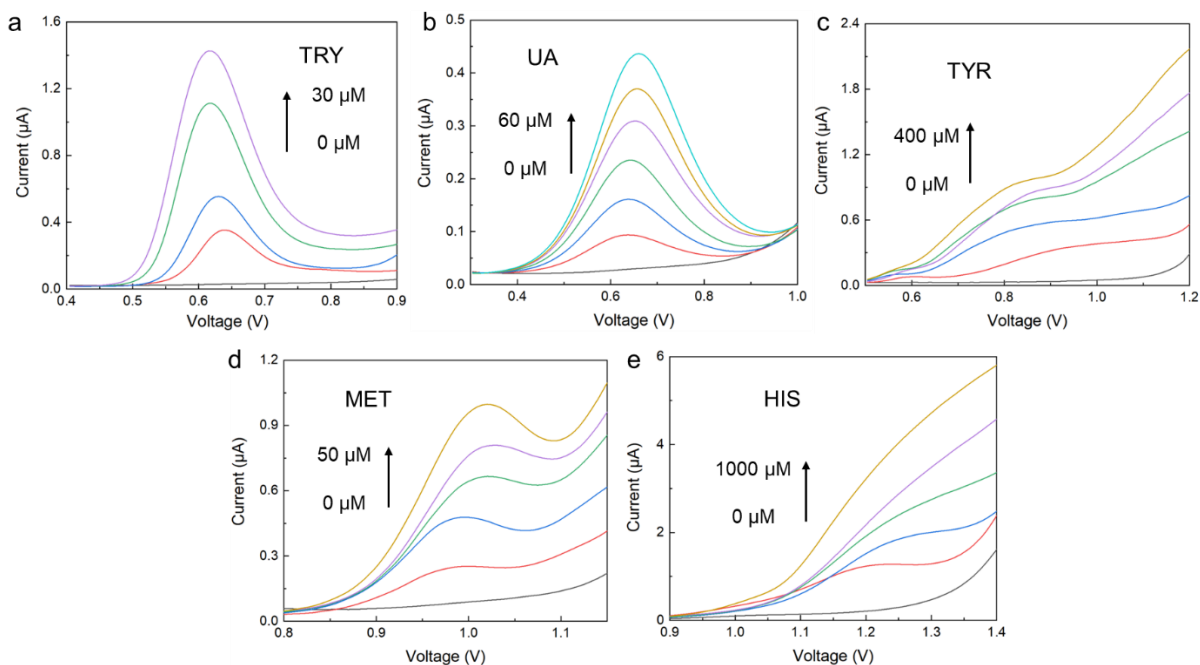


Figure 5.5. Differential pulse voltammograms of electroactive interferents. All experiments were performed within the interferents' physiological relevant concentration ranges in sweat: (a) 0, 5, 10, 20, 30

μM TRY; (b) 0, 10, 20, 30, 40, 50, 60 μM UA; (c) 0, 50, 100, 200, 300, 400 μM TYR; (d) 0, 10, 20, 30, 40, 50 μM MET; (e) 0, 50, 100, 200, 500, 1000 μM HIS (all performed in 0.01 M acetate buffer, pH = 5).

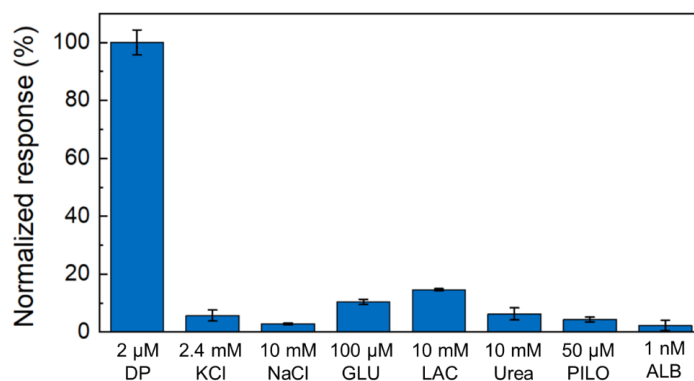


Figure 5.6. Interference study of non-electroactive species. The tests were performed separately, by drop casting 0.01 M acetate buffer (pH = 5) containing 2 μM DP and respective interferents in their physiologically relevant concentration level in sweat: 2.4 mM KCl, 10 mM NaCl, 100 μM glucose (GLU), 10 mM lactate (LAC), 10 mM urea, 50 μM pilocarpine (PILO), and 1 nM albumin (ALB). Measured DP responses were normalized to the measurement with only 2 μM DP (error bars indicate standard error, $n = 3$).

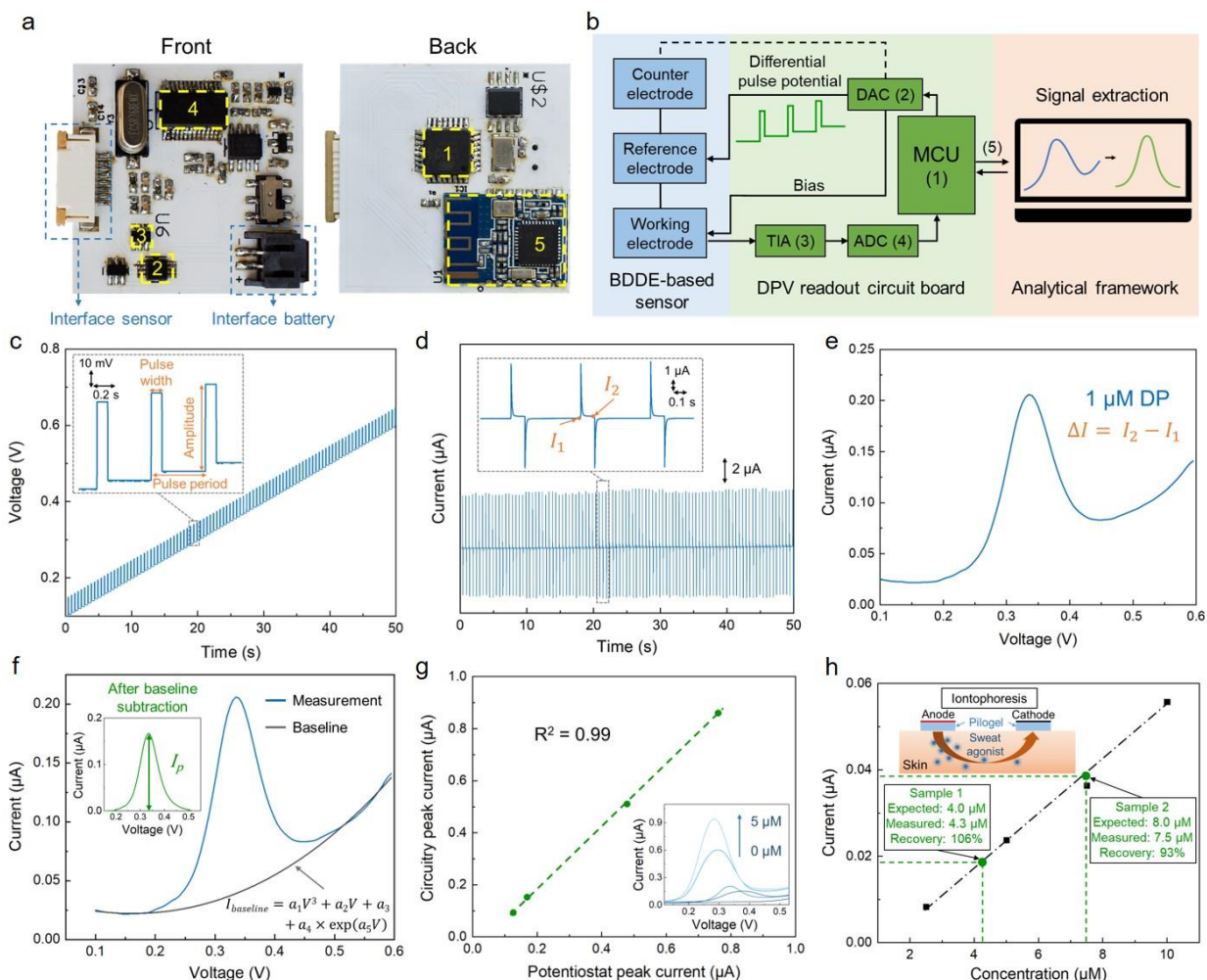


Figure 5.7. Voltammetric sensing system. (a) Front and back view of the custom-developed DPV readout circuit board, which integrates commercially-available chips, including: (1) microcontroller unit (MCU), (2) digital-to-analog converter (DAC), (3) transimpedance amplifier (TIA), (4) analog-to-digital converter (ADC), and (5) Bluetooth transceiver module. (b) System-level block diagram of the DPV readout circuit board interfacing an analytical framework. (c) A representative circuit-rendered differential pulse potential waveform (inset shows the zoomed view, pulse period: 0.5 s, pulse width: 0.1 s, amplitude: 50 mV, step: 5 mV, potential range: 0.1 - 0.6 V). (d) A circuit-rendered real-time current response toward 1 μM DP (in artificial sweat, pH = 5). Inset shows the zoomed view, with an annotated pair of sampling points for differential current response calculation. (e) Differential pulse voltammogram of an artificial sweat sample (pH = 5) spiked with 1 μM DP, rendered by the devised sensing system. (f) Background current fitting of

the 1 μM DP measurement (in artificial sweat, $\text{pH} = 5$), following a combined 3rd-order polynomial and exponential relationship. Inset shows the baseline-subtracted voltammogram. (g) The voltammetric peak current levels of 0, 0.5, 1, 3, 5 μM DP in artificial sweat ($\text{pH} = 5$) measured by the developed DPV readout circuit board *vs.* potentiostat. Inset shows the corresponding differential pulse voltammograms rendered by the board. (h) DP quantification in spiked iontophoretically-induced sweat samples. The DP concentration of the test samples were estimated with the aid of the calibration curve constructed from the DP-spiked calibration samples. Inset shows the schematic of iontophoresis for sweat induction.

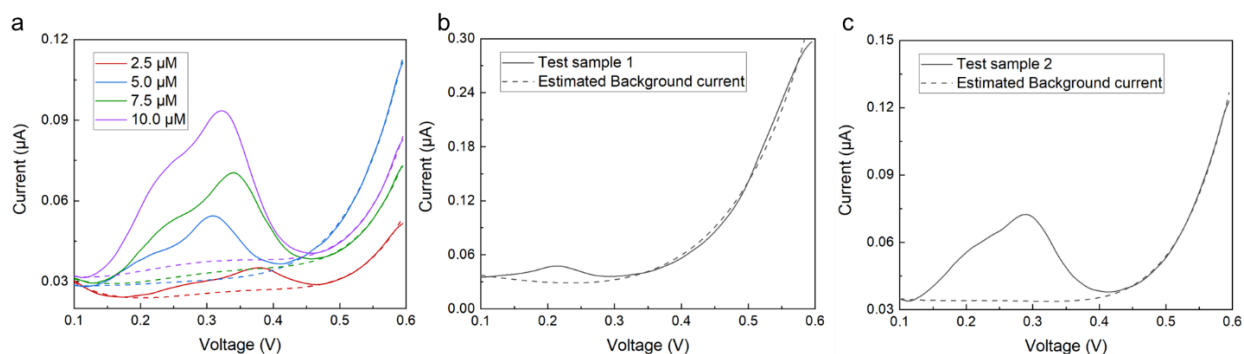


Figure 5.8. Raw DP-spiked sweat measurements. Differential pulse voltammograms (solid lines) and corresponding estimated background current (dotted lines) of iontophoretically-induced sweat samples spiked with (a) 2.5, 5.0, 7.5, 10.0 μM DP as calibration samples, as well as (b) 4.0 μM DP and (c) 8.0 μM DP as test samples.

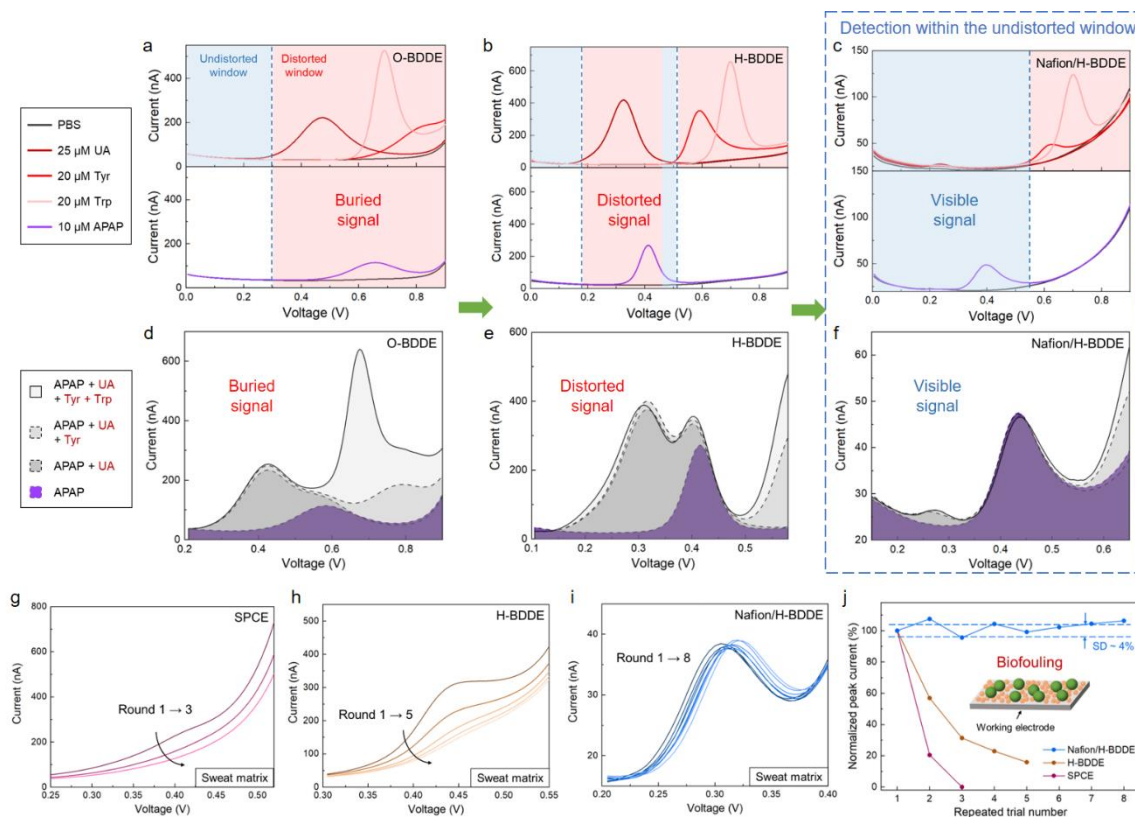


Figure 5.9. Engineering a voltammetric sensing interface for APAP detection within a created undistorted potential window with a high biofouling resistance. (a-c) Characterization of the individual DPV response of the selected endogenous electroactive interferences and the target (with respect to the electrochemical background) using O-BDDE (a), H-BDDE (b), and Nafion/H-BDDE (c) sensors. Upper panels: 25 μM UA, 20 μM Tyr, 20 μM Trp. Lower panels: 10 μM APAP. The interferences' potential windows of influence (distorted windows) and the undistorted windows are annotated. (d-f) Characterization of the DPV response of the target in presence of interferences (all at the same concentration levels as stated above) using O-BDDE (d), H-BDDE (e), and Nafion/H-BDDE (f) sensors. (g-i) Sequentially recorded differential pulse voltammograms of a sweat sample (spiked with 10 μM APAP) on SPCE (g), H-BDDE (h), and Nafion/H-BDDE (i) interfaces. (j) Corresponding voltammetric peak current of the spiked-sweat measurements (extracted with the aid of the analytical framework). The values are normalized with respect to those obtained in the corresponding first rounds. Inset shows the schematic of biofouling.

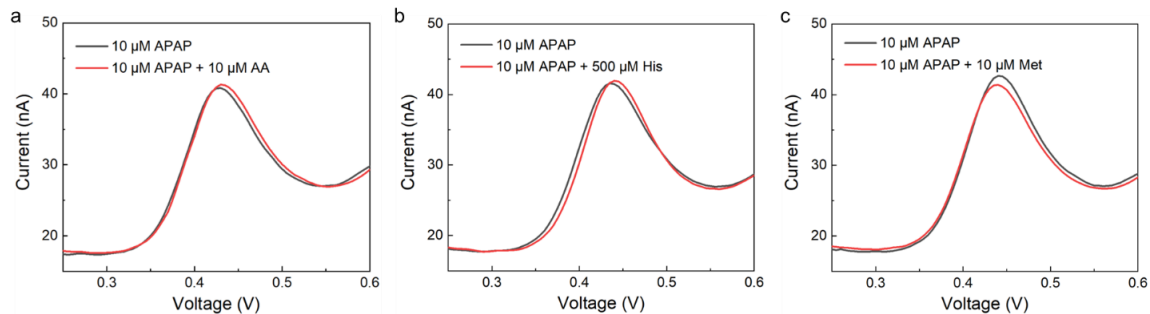


Figure 5.10. Interference of other electroactive species. Differential pulse voltammograms of 10 μM APAP (in PBS) with subsequent addition of the electroactive interferents: (a) 10 μM ascorbic acid (AA), (b) 500 μM histidine (His), and (c) 10 μM methionine (Met).

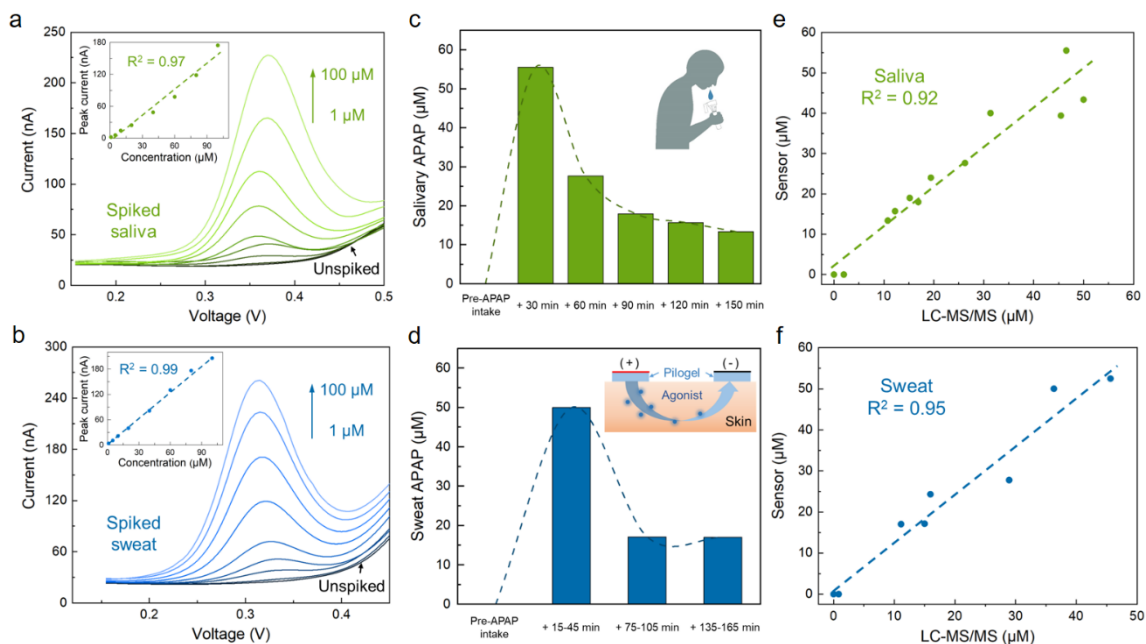


Figure 5.11. Nafion/H-BDDE-enabled ex-situ APAP quantification in non-invasively retrieved biofluid samples (a, c, e: saliva and b, d, f: sweat). (a,b) Differential pulse voltammograms of unspiked and spiked (with 1, 5, 10, 20, 40, 60, 80, 100 μM APAP) saliva (a) and sweat (b) samples. The insets show the corresponding analytical framework-extracted peak current. (c,d) Sensor-measured APAP concentration in the saliva (c) and sweat (d) samples of a human subject, collected before and at intermittent

time-points after the oral administration of a medication containing 650 mg APAP. Insets show the schematics of saliva collection and iontophoresis-based sweat stimulation. (e,f) Sensor-measured APAP concentrations in saliva (e) and sweat (f) samples *versus* the corresponding LC-MS/MS readouts.

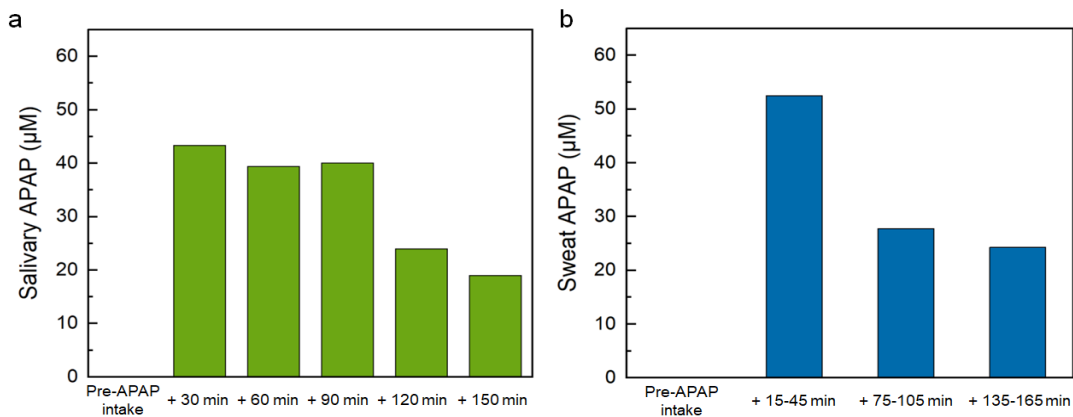


Figure 5.12. Sensor-measured APAP concentration in (a) saliva and (b) sweat samples of the second subject. Samples were collected before and at intermittent time-points after the oral administration of a medication containing 650 mg APAP.

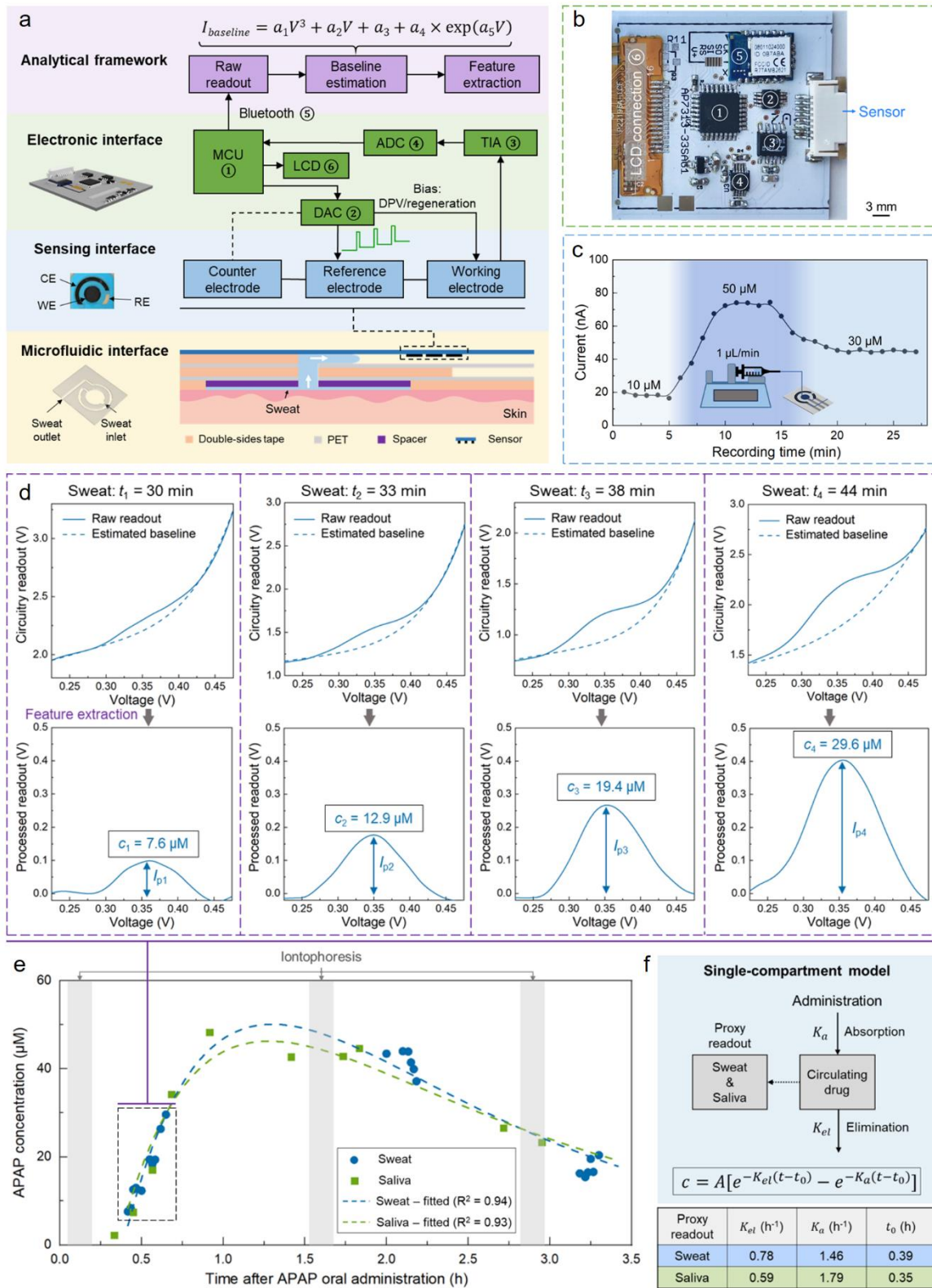


Figure 5.13. Nafion/H-BDDE-enabled wearable solution for on-body pharmacokinetic monitoring.

(a) System-level block diagram of the developed wearable solution, consisting of microfluidic, sensing, and electronic interfaces, and an analytical framework. The top-view photo of the Nafion/H-BDDE-based sensor illustrates the footprint of the working (3 mm-diameter), counter, and reference electrodes (WE, CE, and RE) used. (b) Photo of the custom-developed wireless DPV readout circuit board, which integrates commercially available electronic components, including (1) a microcontroller unit (MCU), (2) a digital-to-analog converter (DAC), (3) a transfer impedance amplifier (TIA), (4) an analog-to-digital converter (ADC), (5) a Bluetooth transceiver module, and (6) a thin-film-transistor LCD screen. (c) Sensor's response to an APAP solution with varying concentration levels, where the APAP solutions were introduced by a continuous flow setup (inset). Peak current values were extracted using the analytical framework. (d) The captured and processed differential pulse voltammograms of sweat (performed by the wearable solution), corresponding to four representative time points (top panel: raw measurements and estimated baselines, bottom panel: baseline-corrected voltammograms to derive the APAP levels). (e) The measured APAP concentration levels in sweat and saliva versus time after oral administration of APAP. Each of the measurement series were fitted into a single-compartment pharmacokinetic model. (f) Schematic of the applied single-compartment model and the tabulated pharmacokinetic parameters, which were extracted from the APAP readouts shown in Fig. 5.13E.

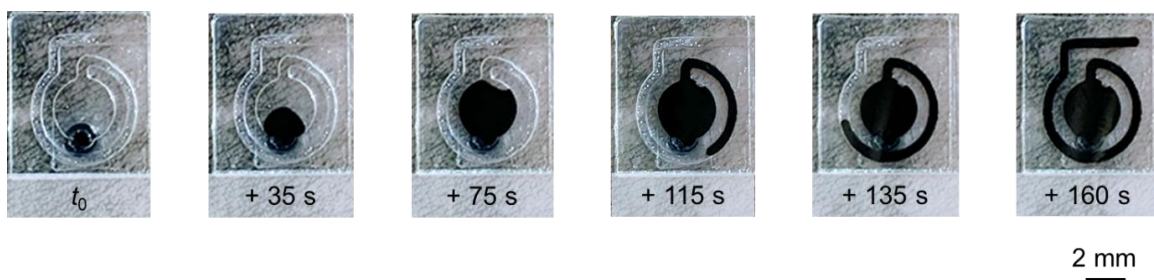


Figure 5.14. Sequential optical images of the in-situ sweat sampling/routing by the designed microfluidic interface. The sensor was replaced by a transparent plastic film to allow for visualization. t_0 : initiation of the sweat secretion post iontophoresis (~5.5 min in this trial).

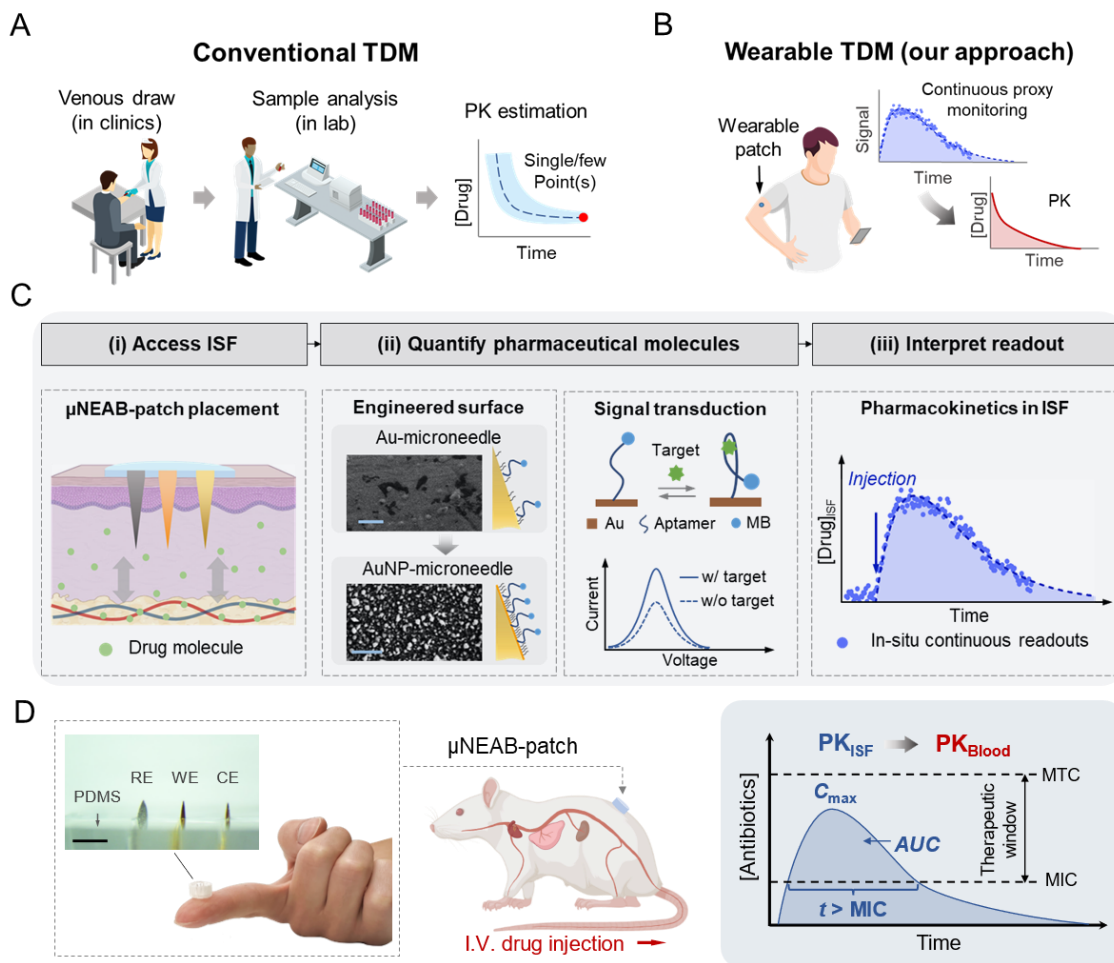


Figure 6.1. μ NEAB-patch for wearable TDM. (A) Schematic illustration of the conventional TDM approach. The approach consists of venous blood draw in clinics followed by analysis in a centralized lab to render single/few drug measurement(s), which is further used to estimate the drug's PK. (B) Schematic illustration of an envisioned wearable TDM solution. A wearable patch was utilized to render continuous in-situ proxy PK measure (e.g., ISF-based), which is subsequently leveraged to infer the circulating PK. (C) Workflow of the μ NEAB-patch-enabled wearable TDM solution. (i) Minimally-invasive access to drug molecules in dermal ISF using an μ NEAB-patch. (ii) The engineered AuNP-microneedle substrate renders reliable aptamer immobilization, where the target-aptamer binding event is transduced into the voltammetric readout variations. Insets show the SEM images of two microneedle electrode surfaces (scale bars: 5 μ m). (iii) Construction of PK in ISF using in-situ continuous μ NEAB-patch readouts. (D) Left: photos of an assembled μ NEAB-patch, consisting of microneedle electrodes inserted in a PDMS substrate.

WE, CE, and RE correspondingly denote working, counter, and reference electrodes. Scale bar: 2 mm. Middle: schematic representation of applying a μ NEAB-patch for drug monitoring in a rat model. Right: application of μ NEAB-patch to infer pharmacokinetic characteristics of antibiotics. MTC and MIC denote minimally toxic and inhibitory concentrations, respectively.

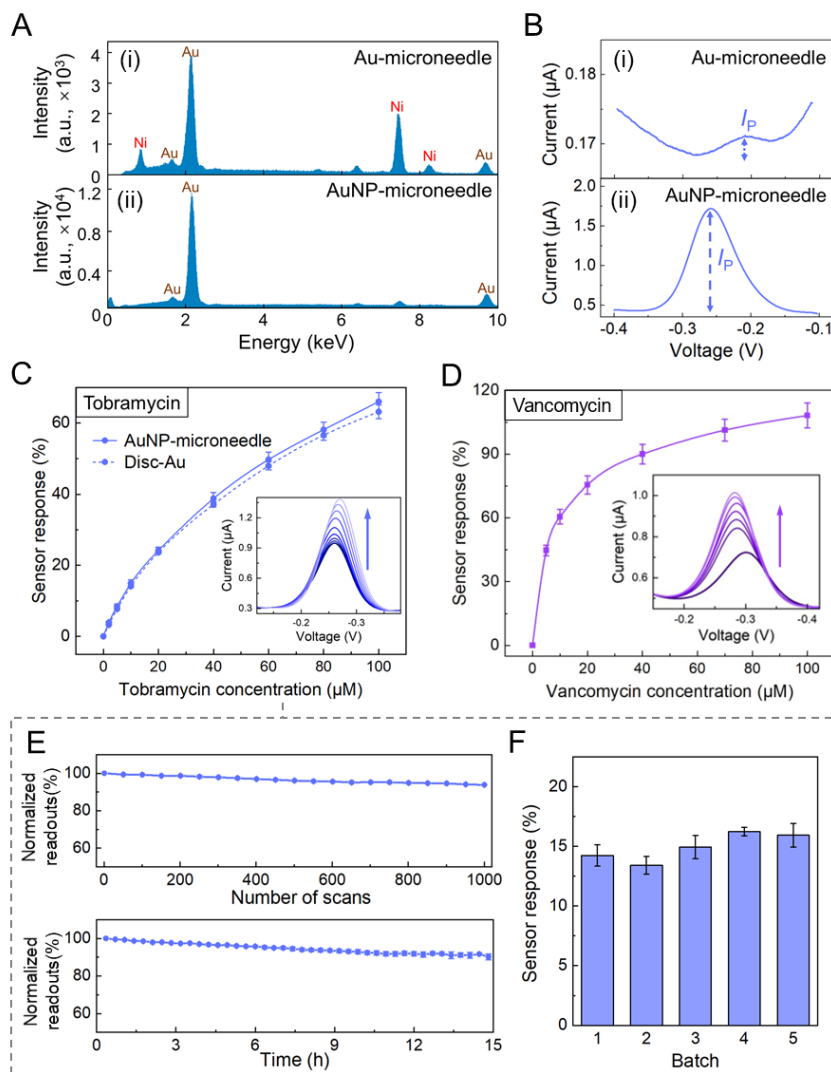


Figure 6.2. Development and characterization of μ NEABs. (A) EDS spectrum of an Au-microneedle surface (i) and an AuNP-microneedle surface (ii). (B) Square wave voltammograms of μ NEABs constructed on Au-microneedle (i) and AuNP-microneedle (ii) substrates. (C) Response of tobramycin μ NEABs, in comparison with tobramycin-EABs constructed on gold disc electrodes. Error bars indicate

standard deviations ($n = 3$). Inset shows the square wave voltammograms acquired from a μ NEAB. **(D)** Response of vancomycin μ NEABs. Error bars indicate standard deviations ($n = 3$). Inset shows the corresponding square wave voltammograms. **(E)** Normalized tobramycin μ NEAB readout variations under repetitive interrogation (upper panel) and with extended operation time (lower panel). Error bars indicate standard deviations ($n = 3$). **(F)** Tobramycin μ NEABs' response to 10 μ M tobramycin. Three sensors were characterized for each batch. Error bars indicate standard deviations. All the experiments were performed in artificial ISF buffer solutions.

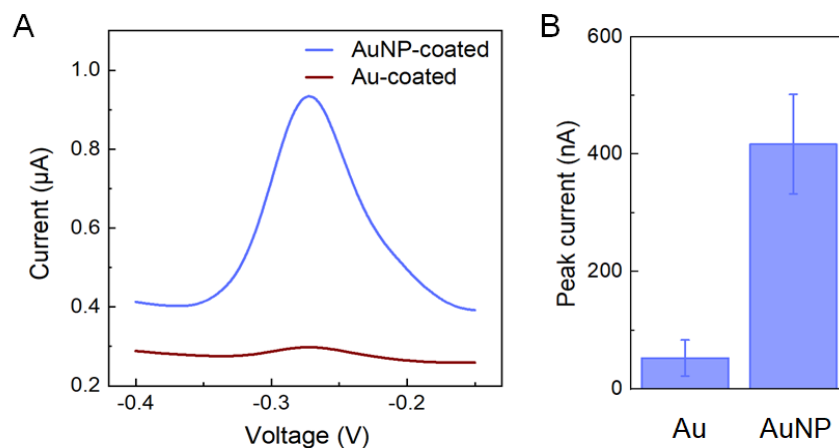


Figure 6.3. Illustration of the surface area enhancement effect using an AuNP coating. (A) Square wave voltammograms of tobramycin- μ NEABs constructed on AuNP-coated and Au-coated microneedle substrates. Here the Au coating was achieved by e-beam evaporation (30 nm chromium/200 nm Au). (B) Extracted MB peak height levels of the two cases in (A). Error bars indicate standard deviations ($n = 3$).

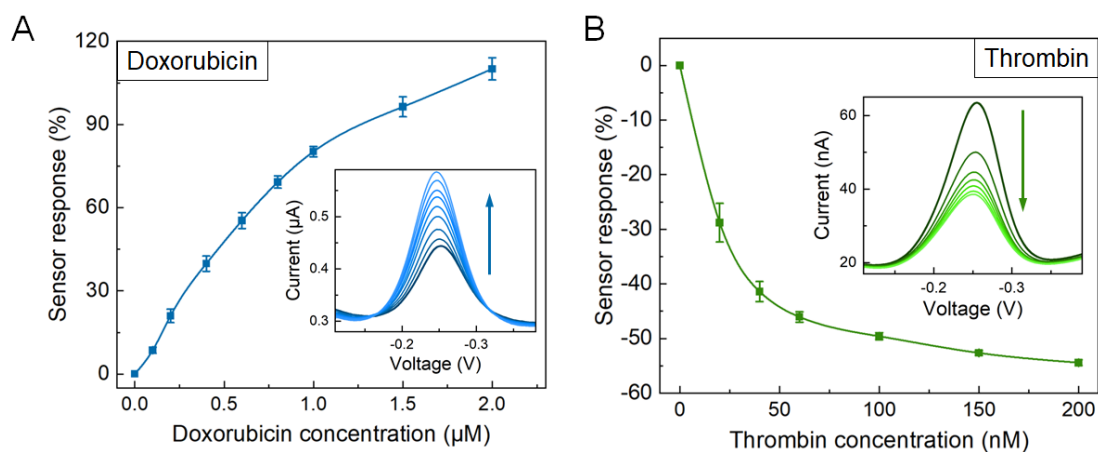


Figure 6.4. μ NEABs targeting doxorubicin and thrombin. Response of (A) doxorubicin μ NEABs and (B) thrombin μ NEABs. Error bars indicate standard deviations ($n = 3$). Insets show the corresponding square wave voltammograms acquired from a representative biosensor.

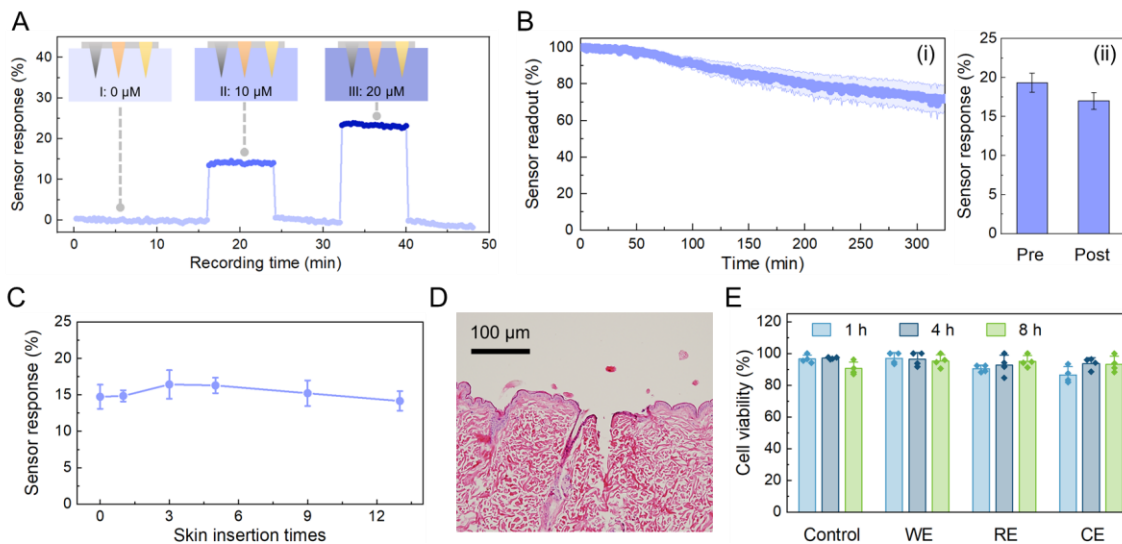


Figure 6.5. Ex-vivo μ NEAB-patch characterization. (A) Continuous measurements of μ NEAB-patch sensing response in a phantom gel setup. The μ NEAB-patch was inserted into three phantom gels in a rotational manner. Inserts show the schematics of the testing setup. Tobramycin concentration levels in the three testing gels: 0, 10, and 20 μ M. (B) (i) Continuous measurements of μ NEAB readout in well-hydrated porcine skin tissue. (ii) μ NEABs' response to 10 μ M tobramycin before and after > 300 min skin tissue exposure. The error band in (i) and error bars in (ii) indicate the standard deviation ($n = 3$). (C) μ NEAB responses to 10 μ M tobramycin before and after repetitive insertion into a porcine skin tissue. The error bars indicate the standard deviation ($n = 4$). (D) Photo of H&E-stained rat skin showing the penetration of a devised microneedle electrode. (E) Viability of HDFs cultured with medium exposed to μ NEAB electrodes for 1, 4, and 8 hours. The control result refers to the test performed using a blank matrix. The error bars indicate the standard deviation of two biological and two technical replicates.

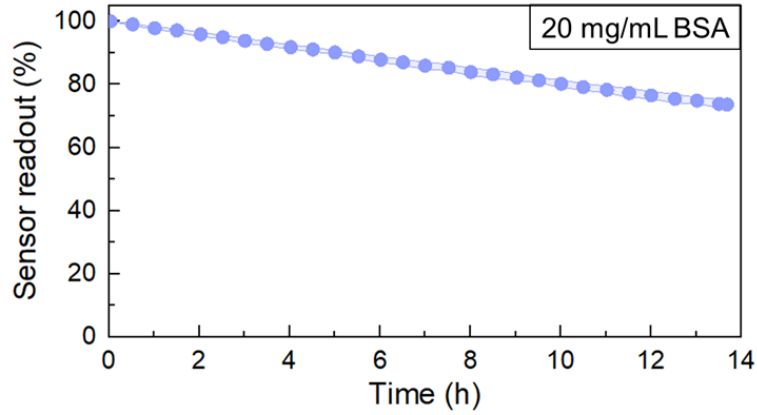


Figure 6.6. μ NEAB drift in a protein-spiked buffer solution. Continuous measurements of μ NEAB readout in an artificial ISF solution spiked with 20 mg/mL bovine serum albumin (BSA).

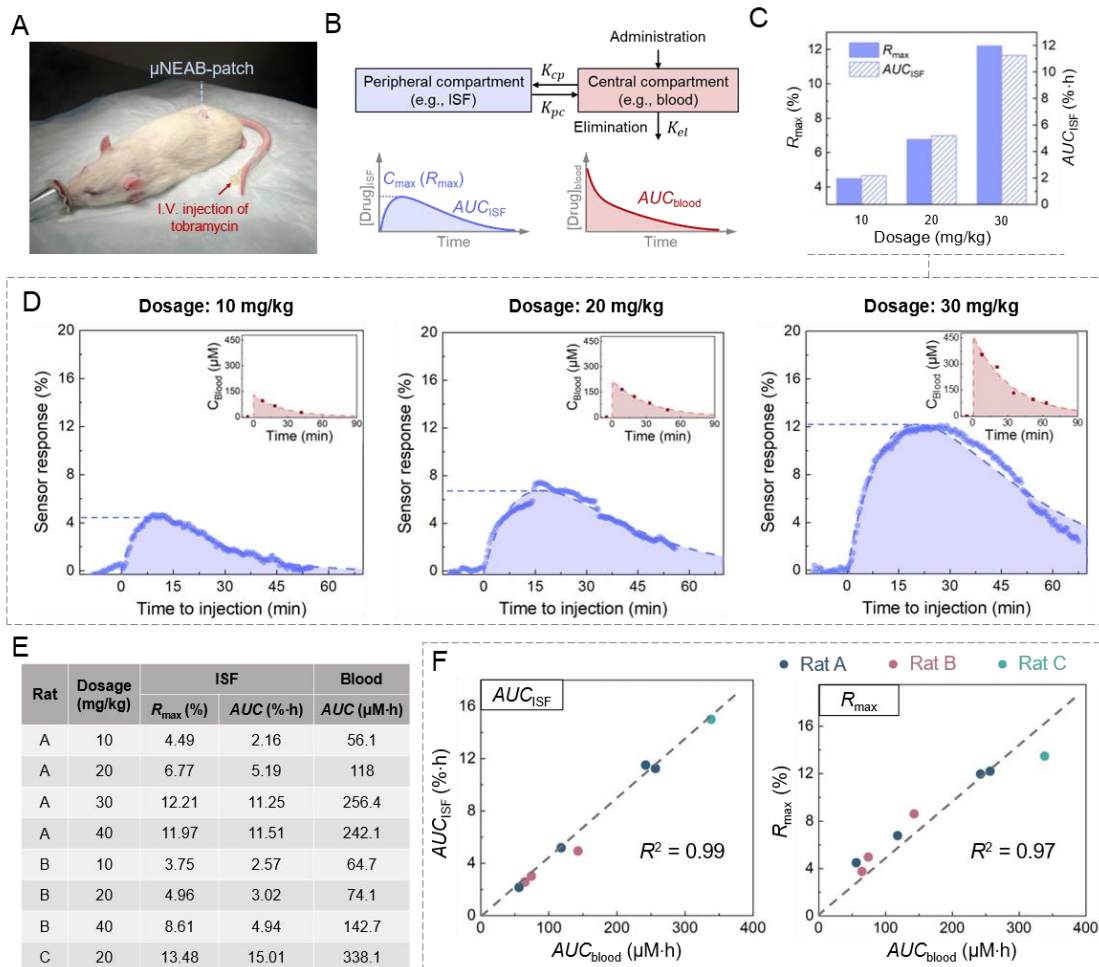


Figure 6.7. In-vivo μ NEAB-patch characterization in a rat model. (A) Photo of the animal study setup. The μ NEAB-patch was placed at the back of the rat and the drug was injected intravenously from the tail vein with the aid of a catheter. (B) Schematics of a two-compartment pharmacokinetic model and representative pharmacokinetic profiles in central and peripheral compartments. K_{pc} , K_{cp} , and K_{el} denote the first-order rate constants for distribution, redistribution, and elimination, respectively. (C) ISF PK parameters of one animal (rat A) with three different tobramycin doses. (D) The measured and baseline-corrected μ NEAB-patch readouts of Figure 4C. Insets show the corresponding blood measurements. Dash lines show the fitted pharmacokinetic curves. (E) Tabulated PK results among three animals (eight trials). (F) Correlations between PK parameters in ISF and blood. Left: AUC_{blood} versus AUC_{ISF} ; right: AUC_{blood} versus R_{max} .

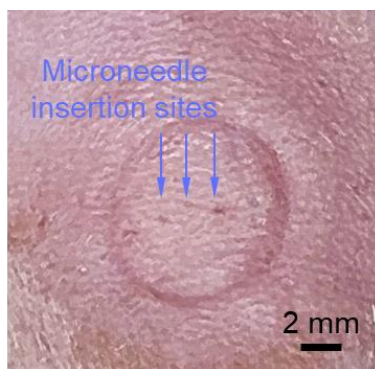


Figure 6.8. Optical image of the rat skin right after μ NEAB-patch removal. The insertion sites of the microneedle electrodes are annotated.

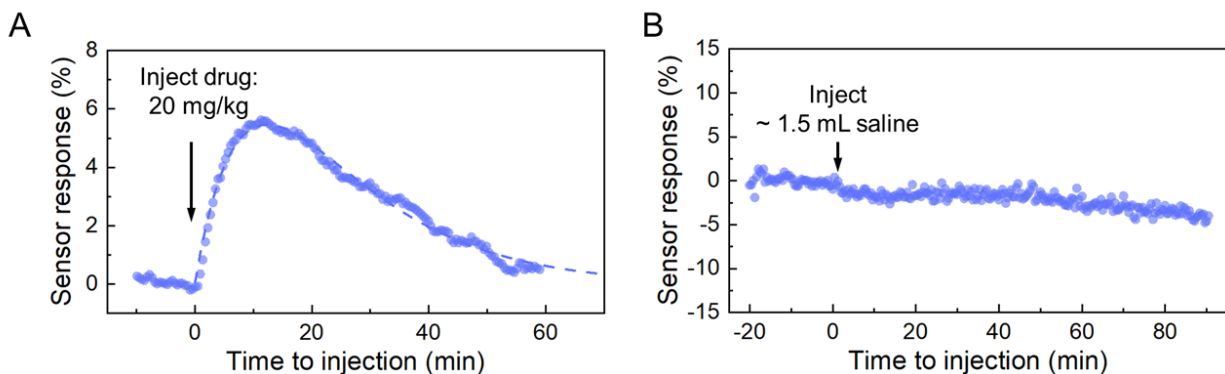


Figure 6.9. In-vivo biomonitoring using μ NEAB-patches. (A) Measured and baseline-corrected μ NEAB-patch response to the tobramycin injection (injection dosage: 20 mg/kg). (B) μ NEAB-patch response to the saline injection (serving as a control experiment).

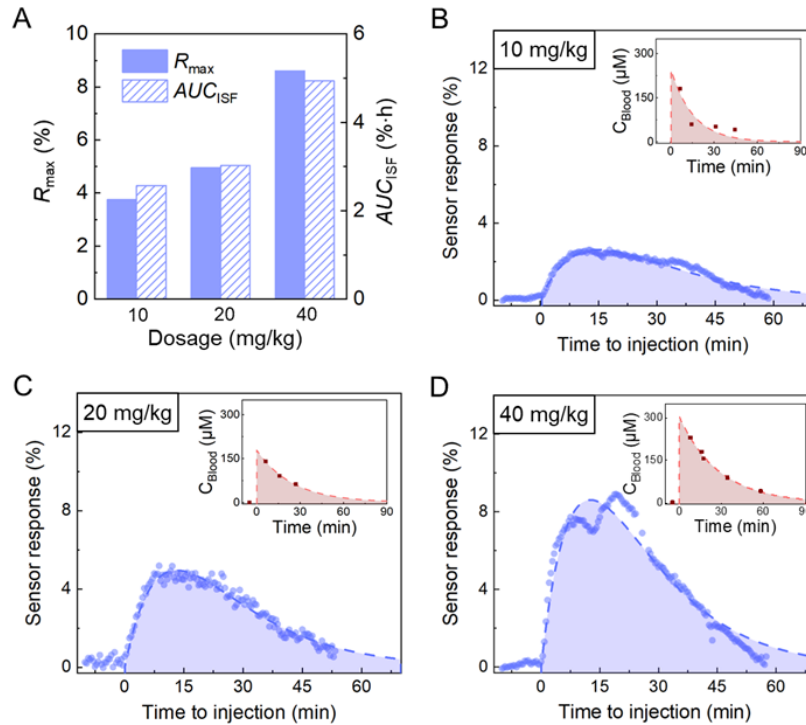


Figure 6.10. Raw PK monitoring results of rat B. (A) ISF PK parameters of rat B with three different tobramycin doses. (B-D) The measured and baseline-corrected μ NEAB-patch responses of the figure A. Insets show the corresponding blood measurements. Dash lines show the fitted PK curves. Dotted lines show the fitted pharmacokinetic curves.